

Jan-Michael Schreiber: Plausibility Tracking : A method to evaluate anatomical connectivity and microstructural properties along fiber pathways. Leipzig: Max Planck Institute for Human Cognitive and Brain Sciences, 2014 (MPI Series in Human Cognitive and Brain Sciences; 157)

---

---

Plausibility Tracking: A method to  
evaluate anatomical connectivity and  
microstructural properties along fiber  
pathways

---

## Impressum

Max Planck Institute for Human Cognitive and Brain Sciences, 2014



Diese Arbeit ist unter folgender Creative Commons-Lizenz lizenziert:  
<http://creativecommons.org/licenses/by-nc/3.0>

Published online at the Digitalen Bibliothek Thüringen

<http://www.db-thueringen.de/>

urn:nbn:de:gbv:ilm1-2014000201

Druck: Sächsisches Druck- und Verlagshaus Direct World, Dresden

Titelbild: © Jan Schreiber, 2014

ISBN 978-3-941504-41-7

# Plausibility Tracking: A method to evaluate anatomical connectivity and microstructural properties along fiber pathways

## DISSERTATION

zur Erlangung des akademischen Grades  
Doktoringenieur (Dr.-Ing.)

vorgelegt der Fakultät für Biomedizinische Technik  
Institut für Biomedizinische Technik und Informatik  
der Technischen Universität Ilmenau

von Jan-Michael Schreiber  
geboren am 20. Februar 1974 in München

Gutachter:  
Prof. Dr.-Ing. habil. Jens Haueisen  
PD Dr.-Ing. habil. Thomas R. Knösche  
Prof. Maxime Descoteaux, Ph.D.

Tag der Einreichung: 24. Oktober 2013  
Tag der wissenschaftlichen Aussprache: 14. April 2014



# Contents

<b>1</b>	<b>Abstract</b>	<b>1</b>
<b>2</b>	<b>Zusammenfassung</b>	<b>3</b>
<b>3</b>	<b>Abbreviations</b>	<b>5</b>
<b>4</b>	<b>Introduction</b>	<b>7</b>
4.1	Motivation . . . . .	7
4.2	Current state . . . . .	8
4.3	Limitations . . . . .	8
4.4	Suggested solution . . . . .	9
4.5	Graphical overview . . . . .	10
4.6	Major contributions . . . . .	12
4.7	Structure of the thesis . . . . .	12
<b>5</b>	<b>Background</b>	<b>15</b>
5.1	Overview . . . . .	15
5.2	The human brain - function, organization and structure . . . . .	16
5.3	Principles of diffusion MRI . . . . .	19
5.3.1	Brownian motion of molecules . . . . .	19
5.3.2	Quantifying the motion of water molecules using MRI . . . . .	21
5.4	Local models of diffusion MRI . . . . .	26
5.4.1	Diffusion tensor . . . . .	26
5.4.2	Multi-tensor . . . . .	29

---

5.4.3	Multi-compartment models . . . . .	29
5.4.4	Diffusion spectrum imaging . . . . .	32
5.4.5	Q-ball . . . . .	33
5.4.6	Spherical deconvolution . . . . .	35
5.5	fODF representation with spherical harmonics . . . . .	39
5.6	Reconstruction of white matter fiber tracts by tractography . . . . .	40
5.6.1	Deterministic tractography . . . . .	40
5.6.2	Probabilistic tractography . . . . .	42
5.6.3	Global tractography . . . . .	44
5.7	Comparing microstructural differences within or between groups . . . . .	45
5.7.1	Voxel-based analysis . . . . .	45
5.7.2	Region-based analysis . . . . .	45
5.7.3	Tract-based spatial statistics . . . . .	47
5.7.4	Raffelt's method . . . . .	48
5.7.5	Tract-based analysis . . . . .	49
<b>6</b>	<b>Methods</b>	<b>51</b>
6.1	Overview . . . . .	51
6.2	MRI data . . . . .	51
6.3	Preprocessing . . . . .	52
6.3.1	Removal of corrupted volumes . . . . .	52
6.3.2	Spatial normalization and interpolation . . . . .	54
6.3.3	Brain extraction . . . . .	54
6.3.4	Creation of white matter mask . . . . .	54
6.4	Local modeling . . . . .	56
6.4.1	Spherical deconvolution . . . . .	56
6.4.2	Indices derived from spherical deconvolution and the diffusion tensor . . . . .	57
6.5	Plausibility Tracking . . . . .	59
6.5.1	Introduction . . . . .	59
6.5.2	Initialization . . . . .	60
6.5.3	Optimization . . . . .	62

6.6	Applications . . . . .	67
6.6.1	Reconstruction of distinct fiber pathways . . . . .	67
6.6.2	Connections through minor pathways . . . . .	68
6.6.3	Mapping indices onto individual fiber bundles . . . . .	69
6.6.4	Comparing indices between groups . . . . .	71
<b>7</b>	<b>Results</b>	<b>73</b>
7.1	Overview . . . . .	73
7.2	Local modeling . . . . .	74
7.3	Plausibility Tracking . . . . .	76
7.3.1	Validation with data of a phantom . . . . .	76
7.3.2	Comparison with deterministic and probabilistic tractography . . . . .	82
7.4	Applications . . . . .	85
7.4.1	Reconstruction of distinct fiber bundles . . . . .	85
7.4.2	Connections through minor pathways . . . . .	87
7.4.3	Mapping indices onto individual fiber bundles . . . . .	87
7.4.4	Comparing indices between groups . . . . .	90
<b>8</b>	<b>Discussion</b>	<b>97</b>
8.1	Overview . . . . .	97
8.2	Comparison to other methods . . . . .	98
8.3	Constrained spherical deconvolution . . . . .	99
8.4	Indices based on Bingham functions . . . . .	100
8.5	Plausibility Tracking . . . . .	101
8.6	Mapping of indices and statistical evaluation . . . . .	103
<b>9</b>	<b>Summary and outlook</b>	<b>105</b>
	<b>References</b>	<b>107</b>
	<b>List of Figures</b>	<b>121</b>
	<b>List of Tables</b>	<b>125</b>
	<b>Erklärung</b>	<b>127</b>





# 1 | Abstract

Complex cognitive functions are usually processed by a number of cooperating areas in the human brain. But how are these areas connected to each other and to what extent does a connection's strength correlate with cognitive abilities?

Diffusion weighted magnetic resonance imaging makes it possible to reconstruct the courses of fiber bundles which shows how different areas of the brain might be connected. This imaging technique can also be used to characterize microstructural properties of brain tissue. If these two methods are combined in a way where the local direction of a pathway is used to select indices that describe the structure of the connecting fiber bundle without the influence of crossing fiber bundles, new insights into the function and development of the human brain can be gained.

In order to model a connecting pathway, a new method of global tractography called "Plausibility Tracking" has been developed. According to the underlying data, Plausibility Tracking provides the most plausible connecting pathway between two areas in the brain. The quality of the pathway is rated by a new measure: The plausibility of the connection. The tracks of Plausibility Tracking allow selecting the tissue characterizing indices that correspond to the analyzed connection. Plausibility Tracking is embedded in a framework that maps these indices onto the pathway. This pathway serves as a coordinate system for inter-subject comparisons. The parametrization of the pathway is guided by a purpose-built atlas in order to take into account the individual anatomical peculiarities of each subject.

Plausibility Tracking makes it possible to compare fiber bundle specific indices that characterize connecting pathways along their arc length. These biophysically meaningful indices allow a more specific characterization of the fiber bundle's microstructure

than the usually used fractional anisotropy. At the same time, the method has little more requirements on the scanning protocol than standard acquisitions. Consequently, the method presented in this thesis can even be used in clinical environments.

## 2 | Zusammenfassung

Komplexe kognitive Funktionen werden in der Regel von mehreren Arealen im Gehirn gemeinsam geleistet. Aber wie sind diese Areale miteinander verbunden und in welchem Maße korreliert die Stärke der Verbindungen mit kognitiven Fähigkeiten?

Die diffusionsgewichtete Magnetresonanztomographie ermöglicht es, die Verläufe von Faserverbindungen nachzuvollziehen und zeigt damit, wie verschiedene Areale im Gehirn miteinander verbunden sind. Dieses Bildgebungsverfahren kann außerdem dazu eingesetzt werden, um mikrostrukturelle Eigenschaften des Gehirns zu beschreiben. Wenn diese beiden Methoden so miteinander verknüpft werden, dass die lokale Richtung eines Faserverlaufs dazu verwendet wird den Wert auszuwählen, der die Struktur dieser Verbindung beschreibt, dann können neue Erkenntnisse über die Funktion und Entwicklung des menschlichen Gehirns gewonnen werden.

Um einen Verbindungspfad zu modellieren wurde eine neue globale Traktographiemethode namens “Plausibility Tracking” entwickelt. Basierend auf den zugrundeliegenden Daten liefert Plausibility Tracking den plausibelsten Verbindungspfad zwischen zwei Arealen im Gehirn. Die Qualität des Verlaufs wird mit einem neuen Maß, der Plausibilität einer Verbindung, bewertet. Die Pfade von Plausibility Tracking erlauben es, diejenigen Werte der Gewebecharakterisierung auszuwählen, die zu der zu untersuchenden Verbindung gehören. Plausibility Tracking ist in ein System eingebettet, welches diese Werte auf die Verbindungspfade projiziert. Diese Verbindungspfade dienen als Koordinatensysteme für den Vergleich der Werte zwischen Probanden. Um die anatomischen Eigenheiten der Probanden zu berücksichtigen, wird die Parametrisierung des Verbindungspfades durch einen speziell angefertigten Atlas geleitet.

Plausibility Tracking ermöglicht es, faserbündelspezifische Werte die Verbindungspfade kennzeichnen entlang deren Verlauf zu vergleichen. Diese biophysikalisch sinnvollen Werte erlauben eine spezifischere Beschreibung der Mikrostruktur eines Faserbündels, als die zumeist verwendete fraktionale Anisotropie. Gleichzeitig stellt die Methode kaum höhere Anforderungen an die Aufnahmesequenz als etablierten Standardmethoden. Folglich kann die hier vorgestellte Methode sogar im klinischen Bereich eingesetzt werden.

## 3 | Abbreviations

<b>AD</b>	axial diffusivity
<b>ADC</b>	apparent diffusion coefficient
<b>ADC(<math>\parallel</math>)</b>	parallel diffusivity
<b>ADC(<math>\perp</math>)</b>	perpendicular diffusivity
<b>AFD</b>	angular fiber density
<b>AFDmax</b>	maximal angular fiber density
<b>BA45</b>	Brodmann area 45
<b>CC</b>	corpus callosum
<b>CHARMED</b>	composite hindered and restricted model of diffusion
<b>CR</b>	corona radiate
<b>CSD</b>	constrained spherical deconvolution
<b>CSF</b>	corticospinal fluid
<b>dMRI</b>	diffusion magnetic resonance imaging
<b>dODF</b>	diffusion orientation density function
<b>DTI</b>	diffusion tensor imaging
<b>fODF</b>	fiber orientation density function
<b>FA</b>	fractional anisotropy
<b>FD</b>	fiber density
<b>FFT</b>	fast Fourier transform
<b>FS</b>	fiber spread

<b>GRAPPA</b>	generalized auto calibrating partially parallel acquisitions
<b>HARDI</b>	high angular resolution diffusion imaging
<b>IFOF</b>	inferior fronto-occipital fasciculus
<b>ILF</b>	inferior longitudinal fasciculus
<b>MAD</b>	median absolute deviation
<b>MC</b>	motor cortex
<b>MD</b>	mean diffusivity
<b>MNI</b>	Montreal Neurological Institute
<b>MRI</b>	magnetic resonance imaging
<b>NODDI</b>	neurite orientation dispersion and density imaging
<b>PFA</b>	peak fractional anisotropy
<b>PFC</b>	prefrontal cortex
<b>RBA</b>	region-based analysis
<b>RD</b>	radial diffusivity
<b>ROI</b>	region of interest
<b>SD</b>	spherical deconvolution
<b>SLF</b>	superior longitudinal fasciculus
<b>SH</b>	spherical harmonics
<b>TBA</b>	tract-based analysis
<b>TBSS</b>	tract-based spatial statistics
<b>VBM</b>	voxel-based morphology
<b>VBA</b>	voxel-based analysis
<b>voxel</b>	volume element

## 4 | Introduction

### 4.1 Motivation

For centuries men and women have tried to better understand how the human brain works. Lesions for example that could be correlated with functional deficits gave hints to which areas of the brain are involved into which functions. Fortunately, with today's methods it does not require injuries anymore to study the human brain and its functions. Non-invasive imaging methods give insights into the brain's anatomy and function like never before. Studies can be performed on healthy volunteers and even children. Comparing data from children with data from adults allows to correlate cognitive skills with anatomical changes at different ages and provides valuable insights into how the human brain works.

It is known that complex cognitive functions are processed in cooperation of multiple areas of the brain. But how are these areas connected to each other and to what extend does a connection's strength correlate with cognitive abilities?

In order to help answering these questions, the work presented in this thesis aims to improve the quantification of anatomical connectivity within the human brain. A new method is introduced that determines the most plausible pathway of connections between distinct locations in the brain. Then, microstructural properties that are relevant for the connection strength are mapped onto the pathway to make them comparable across subjects. Comparing these measurements between children and adults helps to understand the development and function of the human brain.



## 4.2 Current state

Many methods to investigate the human brain are based on the analysis of data from *Magnetic resonance imaging* (MRI). MRI is a method to capture volumetric pictures of biological bodies in general and the human brain in particular. One of its outstanding features is that different molecular properties like spin relaxation, concentration and diffusion can be recorded by different sequences at high spatial resolution. All these measurements are non-invasive, which means that there is no known persistent side effect for the scanned persons (Formica and Silvestri, 2004). Accordingly, MRI can be applied for various studies on healthy human subjects. The different scanning protocols allow to investigate various aspects of anatomy, physiology and chemistry to obtain a wide range of information. The scanning protocol of interest here is *diffusion weighted MRI* (dMRI) (Le Bihan, 1991). It allows to estimate the diffusion of water molecules within the tissue and, based on that, permits conclusions about the tissue's microstructure.

There are two major applications of dMRI: quantification of microstructural properties, and reconstruction of fiber pathways called tractography. The quantification of tissue properties is based on local models that provide indices describing certain characteristics of the tissue. From these indices, maps of the brain can be generated that visualize certain characteristics (that are parametrized by the indices) of the tissue. These methods are mostly used to locate and quantify differences between groups of subjects or changes in longitudinal studies (a more detailed explanation is given in chapter 5.7). Tractography, on the other hand, integrates the directional information from local models within a defined neighborhood or from the whole brain to model possible axonal pathways. It allows to draw conclusions about the connectivity of cortical regions and pathways through which two or more regions are linked (more details are provided in chapter 5.6).

## 4.3 Limitations

In most studies only one of these two methods is applied although it seems a logical consequence to map microstructural properties onto connecting pathways to get an in-

tegrated assessment of the connection. A few approaches have been published showing different levels of integration and complexity (see chapter 5.7.5 for a short review).

Still, most of the combining approaches use rotationally invariant indices that characterize the tissue's microstructure in a specific location, but not for a specific fiber bundle. As with current scanner resolutions, one third to two thirds of all white matter voxels include a mixture of multiple fiber bundles (Behrens et al., 2007; Jeurissen et al., 2010). It is not ensured, that the observed peculiarity originates from the bundle of interest itself or from a crossing connection.

The accumulation of index values perpendicular to a pathway's main direction is challenging for strongly curved pathways. Two intersecting planes at the two ends of a pathway, as proposed by previously (Corouge et al., 2006), are only sufficient for relatively straight or very thin pathways.

## 4.4 Suggested solution

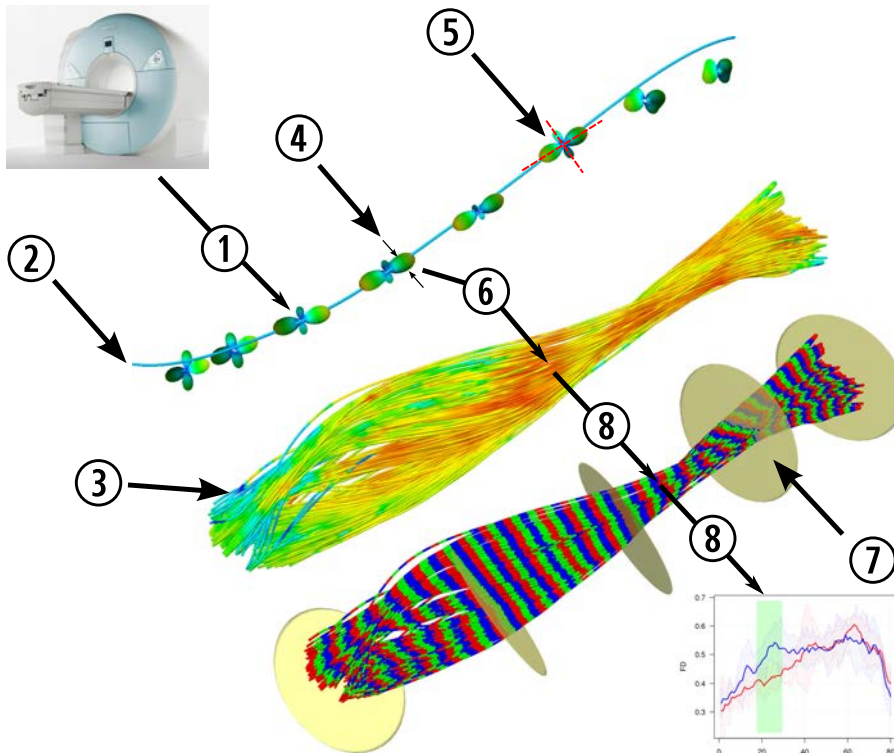
In this thesis a framework is introduced that quantifies bundle specific microstructural properties along fiber pathways. It is composed of multiple methods that are consecutively applied. The goal is to quantify microstructural properties of certain connections in the brain with biophysically meaningful parameters. Such indices have been introduced recently by Riffert and colleagues 2014. They are based on *constrained spherical deconvolution* (CSD) (Tournier et al., 2007) that can be computed from standard single shell *high angular resolution diffusion imaging* (HARDI) (Tuch et al., 2002). The required data can be acquired in reasonable time from most clinical scanners. The indices provide multiple biophysically meaningful measures like fiber density, fiber fraction and fiber spread. In regions of crossing fiber bundles, the indices are available for every fiber bundle separately. They promise to increase the specificity in characterizing the tissue microstructure compared to the most often used rotationally invariant indices derived from the diffusion tensor.

The directionality of these indices poses the problem to reliably select the correct index value that corresponds to the pathway of interest. This challenge is solved by a new method of tractography called *Plausibility Tracking*, which is the core method of this thesis. According to the underlying dMRI data it models the most plausible connecting path between two locations in the brain and provides reliable information

about the the pathway's direction along the pathway. For initialization, it uses probabilistic tractography (see chapter 5.6.2) to obtain close to optimal starting parameters that keep the time for optimization at a minimum. Additionally, Plausibility Tracking offers a new measure of connectivity that describes the anatomical plausibility of a connection.

The parametrization of the connecting pathway is supported by a purpose-built atlas. Multiple intersecting planes are defined between the atlas labels and serve as anchors for the parametrization along the pathway's arc length.

## 4.5 Graphical overview



- ① The local model shows the fiber configuration as computed from diffusion weighted MRI data in every voxel.
- ② Most plausible tracks through the field of local models are computed with a new method of global tractography.
- ③ A bundle of these tracks is obtained when all connecting tracks between two regions in the brain are computed.
- ④ Biophysically meaningful indices are computed for every direction provided by the local model.
- ⑤ The index values corresponding to the connection of interest are determined by their accordance with the direction of a tract.
- ⑥ The corresponding index values are mapped onto the fiber bundle.
- ⑦ Intersecting planes, which are defined by an atlas, support the parametrization of the fiber bundle into narrow sections.
- ⑧ Index values which have been mapped onto the tracks are accumulated according to the bundle's parametrization and are available for statistical evaluation across subjects.

## 4.6 Major contributions

The major contributions of this thesis are:

- **A framework to compare bundle specific parameters derived from dMRI across subjects**

This framework is implemented in a fully automatic processing pipeline that performs data preprocessing, local modeling, computation of indices, Plausibility Tracking, mapping of indices onto the fiber bundles and statistical evaluation.

- **Introduction of a new global tractography method called *Plausibility Tracking***

Plausibility Tracking models, according to the underlying data, the most plausible pathway between two locations in the brain. It uses a new measure that rates the plausibility of a local direction independently from the strength of the fiber bundles. The smooth path provides a reliable local direction all along the pathway. Additionally, a new measure of connectivity is introduced: the *plausibility* of a connection.

The proposed initialization provides close to optimal starting parameters for the optimization of Plausibility Tracking, so that the computation time is reduced to a minimum, and local minima are avoided.

- **Atlas-based parametrization of fiber bundles**

The parametrization of fiber bundles with bundle specific atlases provides highest correspondences across subjects, taking individual peculiarities of shape into account.

## 4.7 Structure of the thesis

The thesis is organized as follows. Chapter Background gives an overview on state-of-the-art methods that are relevant for or related to this work. It is rather comprehensive as several methods are combined in the presented framework. Chapter Methods describes in detail the novelties and implementations of the framework. In large parts it follows the publication *Plausibility Tracking: A method to evaluate anatomical connectivity*

---

*and microstructural properties along fiber pathways*, which has been submitted to the journal of NeuroImage (Elsevier). The chapter Results is subdivided into validation of the proposed tractography method and applications, featuring the comparison of direction dependent indices along the *inferior longitudinal fasciculus* (ILF) between children and adults. Finally, methods and results are discussed in the last chapter.



## 5 | Background

### 5.1 Overview

This chapter reviews state-of-the-art methods that are applied in or related to the presented framework. Section 5.2 provides an overview of the structure, organization and function of the human brain. It briefly describes the organization of nerve fibers, which is the structure that is analyzed with the presented methods.

The analysis is based on measurements performed with *diffusion weighted MRI* (dMRI). The theoretical concepts and practical applications of this technique are described in section 5.3. It explains how the diffusion of water molecules are measured using dMRI. The structure of this section roughly follows the concept of the book written by Stieltjes (2013).

Local models and their indices are introduced in section 5.4. They describe the characteristics of diffusion and provide the possibility to parametrize microstructural configurations.

As the model used in this thesis uses spherical harmonics for its computation and representation, a short introduction to the mathematics of spherical harmonics is given in section 5.5.

Two applications of diffusion MRI that are based on the local models, namely mapping and comparison of indices as well as tractography, are described in sections 5.6 and 5.7 respectively.



## 5.2 The human brain - function, organization and structure

The human brain is the major part of the central nervous system. It receives and differentiates sensory inputs, stores information and integrates all data to organize complex behavior.

Not every region in the brain is equally involved in all processes of the brain. The anatomically most pronounced peculiarity is the separation into the left and right hemisphere (Fig. 5.1a). Sensory and motor areas for the left side of the body are located in the right hemisphere and vice versa. Within the hemispheres, functional areas can be roughly divided into different areas following anatomical landmarks, as shown in Fig. 5.1b. The frontal lobe is the largest structure in the human brain and associated with e.g. executive processes like voluntary behavior and movement, comprehension, planning, problem solving, cognition, language processing, and many more. In the parietal lobe, somatosensory information are perceived and integrated. It is also the area of spatial attention and mapping as well as number representation. The occipital lobe at the back of the brain is the primary visual area. The temporal lobe is associated with a number of functions like learning and memory, perception for hearing, vision and smell, as well as understanding languages. More archaic functions like startle response, alertness and the control of breathing and heart rate are maintained in the brain stem. The cerebellum is mainly associated with the coordination of voluntary movements, and in particular with the regulation of automatic movements (Purves et al., 2004).

A further subdivision is possible and has been done e.g. based on examinations of microstructure (Brodmann, 1909), observations after injuries, measurements with EEG, MEG and MRI (Bear et al., 2007) and many other methods.

These functions are maintained and executed by highly specialized cells. The most prominent (although not the most numerous) cells within the brain are nervous cells, also called neurons. A schematic drawing of a neuron can be seen in Fig. 5.2. The interior of neurons is composed as most other cells of the body, and includes cell organelles and the nucleus (for more details refer to e.g. Purves et al., 2004). Unique features of neurons are dendrites and axons. Dendrites connect to other neurons to

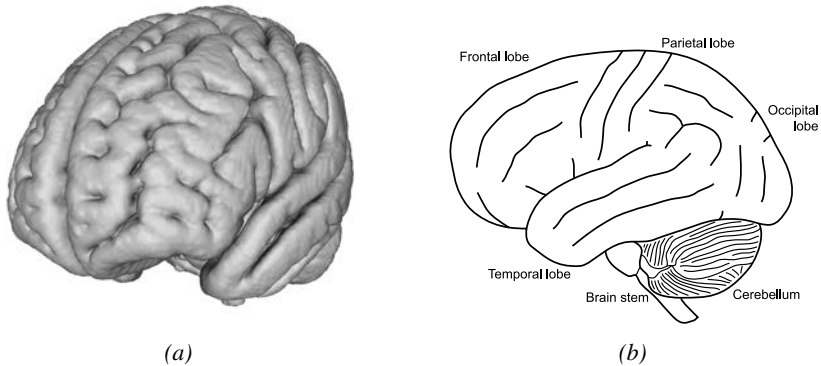


Figure 5.1: The human brain. (a) Reconstructed from MRI data and (b) schematic drawing showing telencephalic lobes, cerebellum and brain stem in different colors. (from [http://commons.wikimedia.org/wiki/File:Gehirn,\\_lateral\\_-\\_Lobi\\_+\\_Stammhirn\\_+\\_Cerebellum\\_eng.svg](http://commons.wikimedia.org/wiki/File:Gehirn,_lateral_-_Lobi_+_Stammhirn_+_Cerebellum_eng.svg))

receive input signals from them. These signals are electrical potentials induced by neurotransmitters and are integrated in the axon hillock and passed on through the axon. The axon is a tail like prolongation. It may be quite short and connect with neighboring neurons or close by areas of the brain, but it can also be very long, projecting to distant brain regions or through the spinal cord into other parts of the body.

The long connections are a major challenge regarding signal transmission, because long distances lead to long transmission times. One possibility to improve the performance of transmission is to increase the axon's diameter, which is not practical for many connections because it requires a lot of space to be effective. Another solution is to improve the insulation of axons by supporting cells. These oligodendrocytes in the brain or Schwann cells in the peripheral nervous system are wrapped around the axons multiple times in several layers. They serve as insulation, the so called *myelin sheath*, which is also sketched in Fig. 5.2. Gaps within the myelin sheath, referred to as nodes of Ranvier, permit the signal in form of potentials to “jump” from node to node. Depending on the degree of myelination, this concept provides a significant increase in transmission time. The conduction velocity in unmyelinated axons ranges from about 0.5 m/s to 1 m/s, whereas the velocity of conduction reach up to 150 m/s in myelinated axons (Purves et al., 2004).

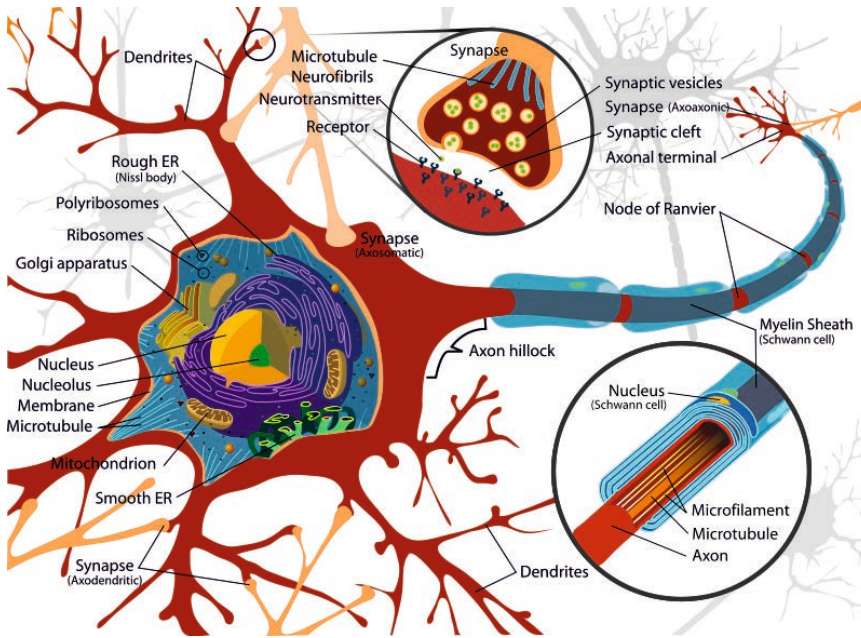


Figure 5.2: Picture of a neuron showing the internal structure of its cell body, the axon with myelin sheath, its dendrites and synapses from other neurons (from [http://commons.wikimedia.org/wiki/File:Complete\\_neuron\\_cell\\_diagram\\_en.svg](http://commons.wikimedia.org/wiki/File:Complete_neuron_cell_diagram_en.svg)).

The brain can be structured in according to the location of the neuron's bodies and their axons. In general, neuronal cell bodies are located in the so called *gray matter*, which forms the outer 2 mm to 4 mm thick cortical layer of the brain. (see Fig. 5.3a).

Many axons are projecting from the gray matter through the so called *white matter* to close-by or distant regions of the brain. In cases where the axons are connecting neighboring regions, they are referred to as *u-fibers*. Long distance axonal connections are organized in bundles (see Fig. 5.3b). This fact is crucial for the analysis with magnetic resonance imaging, which has a spatial resolution of 1.0 mm to 3.0 mm (using up-to-date clinical scanners). Single axons have a diameter of 1  $\mu\text{m}$  up to 20  $\mu\text{m}$ , and hence are much too small to be distinguished individually with today's imaging methods. But when organized in fiber bundles, axons form a more or less homogenous thread wide enough to be captured with magnetic resonance imaging.

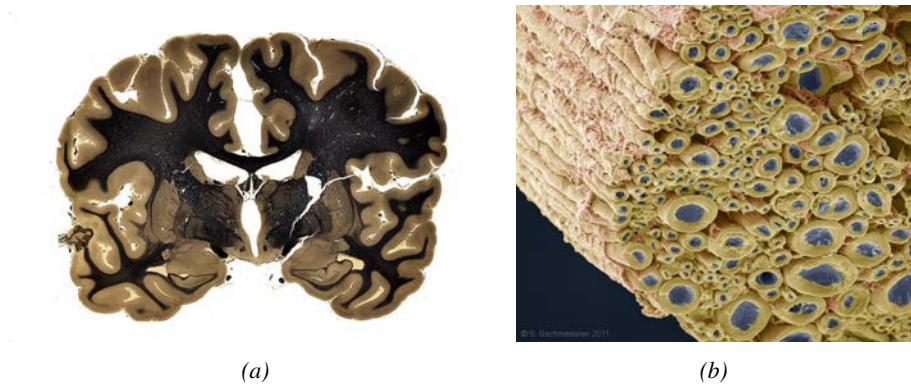


Figure 5.3: The human brain at different scales. (a) Coronal section through a human brain. With the fiber staining, gray matter is shown in brown while the axonal fibers in the white matter are stained black<sup>1</sup>. (b) Microscopic image of a peripheral fiber bundle. (from <http://www.theworldcloseup.com> ©Stephen Gschmeissner)

## 5.3 Principles of diffusion MRI

### 5.3.1 Brownian motion of molecules

The structure of white matter cannot be measured directly, but has to be estimated indirectly through inference with the characteristics of diffusing water molecules.

Molecules in fluids, including water molecules in brain tissue, are constantly in motion (Einstein, 1905). This so called *Brownian motion* is isotropic if there are no barriers or other influencing forces like flow or gradients in concentration. As it is not possible to measure the motion of every molecule separately, a statistical description is used. Here, the expectation value  $\langle x \rangle$  describes the euclidean distance  $x$ , a particle is expected to travel within time  $t$ . As the molecules move in all directions with the same probability, positive and negative directions would cancel out and the expectation value would always be zero. To circumvent this problem, the expectation value of the

<sup>1</sup>Image courtesy of University of Wisconsin, Michigan State Comparative Mammalian Brain Collections and the National Museum of Health and Medicine, preparation of the image and specimen has been funded by the National Science Foundation, as well as by the National Institutes of Health. <http://www.brainmuseum.org/>

squared displacement  $\langle x^2 \rangle$  is used. Einstein (1905) showed that for free diffusion the typical euclidean distance  $\lambda_x$  a molecule is expected to travel within time  $t$  is

$$\lambda_x = \sqrt{\langle x^2 \rangle} = \sqrt{2D_0 t}. \quad (5.1)$$

where  $D_0$  is the *free diffusion coefficient*. Hence, the typical displacement of a particle is proportional to the square root of the diffusion time.

The distribution of distances  $x$ , that are expected to being traveled by the molecules, can be described by the *diffusion propagator*  $P$  (Cory, 1990) which, in the case of free diffusion, is defined as

$$P(x, t) = \frac{1}{2\sqrt{\pi D_0 t}} \exp\left(\frac{-x^2}{4D_0 t}\right). \quad (5.2)$$

This diffusion propagator is a Gaussian function (see Fig. 5.5a) depending on the diffusion coefficient  $D_0$  and the diffusion time  $t$ .

But what happens if the diffusion is not free but restricted by barriers? Axons contain microtubules and neurofilaments that are surrounded by the axonal membrane, which is often covered by a myelin sheath. All these structures influence the anisotropy of the diffusion of water molecules in white matter. Beaulieu and colleagues (2002; 2006) showed that axonal membranes by far exert the strongest influence on the diffusion of water molecules, and are only modulated by the amount of myelin. Hence, the molecules are not able to move freely but are hindered (when located outside the axons) or restricted (when located inside the axons) by the axonal membranes that can be considered as barriers (see fig. 5.4). Note that this is a strongly simplified model. To a small degree, the axonal membranes are permeable to water molecules. Also, although these membranes show the strongest effect on the diffusion process, intracellular structures and supporting cells other than neurons also have an influence on the diffusion of water molecules.

As a logical consequence the expected traveling distance of molecules in tissue is reduced compared to free diffusion. The longer the diffusion time, the more the barriers influence the molecular motion, and the shape of the diffusion propagator loses its Gaussian shape (see Fig. 5.5b).

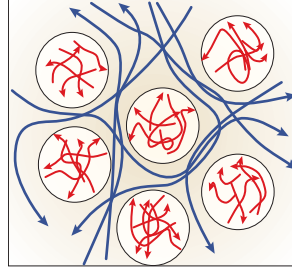


Figure 5.4: Hindered and restricted diffusion caused by axonal membranes. Water molecules in the interaxonal space are hindered in their diffusion (blue) while the molecules inside the axons are restricted (red) in the direction perpendicular to the fiber. (Modified reprint from (Le Bihan, 2003))

In practice, the shape of the diffusion propagator depends on multiple factors, like the distance of the barriers to the starting location, their shape and reflective properties. Still, one can use Eq. 5.2 to define a time dependent diffusion coefficient  $D(t)$  that intuitively describes how far the particles displace within time  $t$  (Stieltjes et al., 2013).

$$\sqrt{\langle x^2 \rangle_{tissue}} = \sqrt{2D(t)t} \quad (5.3)$$

$D(t)$  is not equal to the free diffusion coefficient because it is altered by the structures of the tissue. It is the from the outside visible diffusion coefficient, that is accordingly called the *apparent diffusion coefficient* (ADC) (Le Bihan et al., 1986).

### 5.3.2 Quantifying the motion of water molecules using MRI

As it is not possible to measure the the diffusion of water molecules directly and non-invasively in a closed system like the human body or brain, as special sequence of MRI, named *diffusion weighted MRI* (dMRI), has been developed. With this method, water molecules are labeled with a location specific phase of the nuclear spin. After a defined time of diffusion, the amount of signal attenuation that is quantified due to phase shifts caused by molecules that changed their position. This technique allows to estimate the ADC at arbitrary locations and in any direction, which provides a three dimensional ADC profile in every measured *volume element* (voxel).

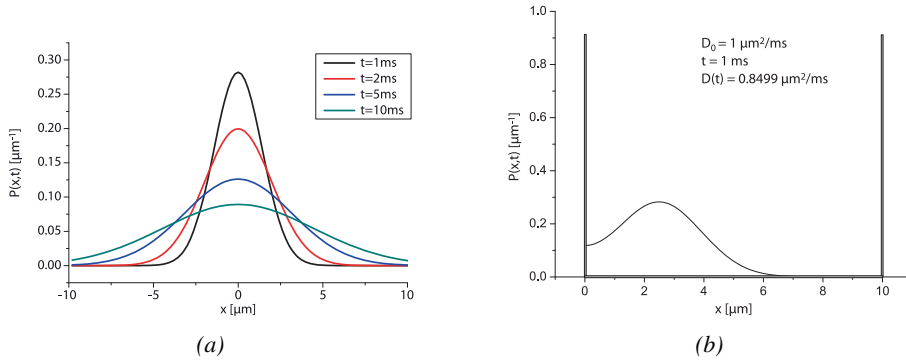


Figure 5.5: Gaussian shape of the diffusion propagator, a) in the case of free diffusion with different diffusion times and b) in the case of restricted diffusion. (reprint from (Stieltjes et al., 2013))

Going into detail, a fundamental property of atoms obviously is their magnetic moment. This moment precesses around an external magnetic field. Its angular frequency depends on the *magnetic field strength*  $B$ , as well as on the *gyromagnetic ratio*  $\gamma$ , which is a nucleus specific constant. The angular frequency at which the spin precesses is called the *Larmor frequency*  $\omega$  which is defined as

$$\omega = -\gamma B. \quad (5.4)$$

In MRI, usually the gyromagnetic ratio of protons ( $^1\text{H}$ ) is used, and as  $\gamma$  is a constant, the Larmor frequency solely depends on the external magnetic field strength  $B$ . Also, the main magnetic field strength is initially kept constant and homogeneous inside the MR scanner. When adding an additional gradient field to the static magnetic field  $B_0$ , protons obtain a Larmor frequency that depends on their position in the scanner and accordingly in the brain. This is used to change the phase of the proton's moments in order to label the water molecules according to their position.

Generally, the diffusion of water molecules can be measured using the following protocol shown in Fig. 5.6:

- $t_1$  Initially, all spins rotate at the same angular frequency and in phase. The signal intensity obtained from this state is recorded and serves as reference signal  $S_0$ .

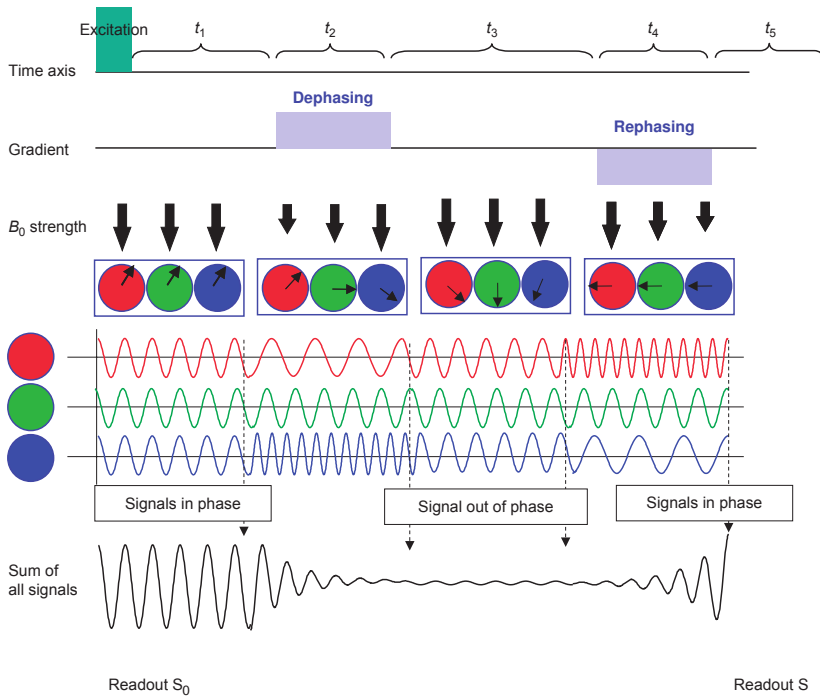


Figure 5.6: Scheme of the dephase-rephase sequence to measure the diffusion of water molecules. Water molecules located at different locations in a sample are represented by the colored circles. Their arrows indicate the current phase arrangement. The length of the thick arrows indicates the strengths of the magnetic field strength ( $B_0$ ) as modified by the gradient. (Reprint with small modifications from (Mori, 2007))

- $t_2$  A magnetic field gradient  $G$  is applied for a short time  $\delta$ . It changes the Larmor frequency depending on the position in the brain. This is called the dephasing gradient.
- $t_3$  In the absence of gradient fields all spins rotate at the same angular frequency but, as a result of the precedent dephasing gradient pulse, with different phases that depend on the position in the brain. Molecules diffuse for a defined time  $\Delta$ .
- $t_4$  A second gradient  $-G$  is applied. It is active for the same time  $\delta$  like the dephasing gradient and has the same strength but goes in the opposite direction compared to the first gradient. This is called the rephasing gradient.



$t_5$  The signal intensity  $S$  is recorded. The spins of the protons that have not moved along the gradient field are again in phase, while the spins of the protons that have moved along the gradient are out of phase. The phase shift, and consequently the signal attenuation, depends on the distances that water molecules have traveled in the direction of the gradient.

In theory, if no diffusion occurs during  $t_3$ , the signal intensity  $S$  at  $t_5$  should be the same as in the reference measurement  $S_0$  during  $t_1$ . In cases where water molecules have traveled along the gradient direction,  $S$  is smaller than  $S_0$ , because not all spins return to phase as they obtain (due to the change in position) a different gradient amplitude for rephasing as for dephasing. The more spins are out of phase and the greater the phase-offset, the lower is the intensity of  $S$ .

This protocol is sensitive for molecular motion only in the direction along the gradient. In order to measure the diffusion in three dimensions, several directions have to be sampled consecutively (Tuch et al., 2002; Jones, 2004).

Stejskal and Tanner (1965) showed that for the narrow pulse assumption ( $\frac{1}{3}\delta \ll \Delta$ ) the ratio of the signal before and after diffusion can be described as an exponential function

$$\frac{S}{S_0} = e^{-\gamma^2 D \delta^2 \Delta G^2} \quad (5.5)$$

where  $\gamma$  is the gyromagnetic ratio,  $D$  the apparent diffusion coefficient,  $\delta$  the duration of the gradient pulses,  $\Delta$  the diffusion time and  $G$  the amplitude of the magnetic gradient. The only unknown in this equation is the apparent diffusion coefficient  $D$ , which can be determined by the described measurement.

In order to simplify equation 5.5 the constants  $\gamma$ ,  $\delta$  and  $G$  can be summarized in the so called *q-value* that is defined as

$$q = \gamma \delta G \quad (5.6)$$

In clinical environments, the so called *b-value* (Le Bihan, 1991) is mostly used instead of the *q-value*. The *b-value* is defined as

$$b = q^2 \Delta = \gamma^2 \delta^2 G^2 \Delta \quad (5.7)$$

Accordingly, Eq. 5.5 can be written as

$$E = \frac{S}{S_0} = e^{-bD} \quad (5.8)$$

where  $E$  is the signal attenuation.

As it is difficult to interpret the signal attenuation profile directly, local models with meaningful parameters are usually fitted into the signal attenuation profile.

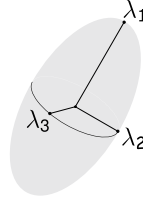


Figure 5.7: The diffusion tensor visualized as ellipsoid. The eigenvalues  $\lambda_{1,2,3}$  of the tensor matrix describe the ellipsoid's axes.

## 5.4 Local models of diffusion MRI

### 5.4.1 Diffusion tensor

With *diffusion tensor imaging* (DTI) (Basser et al., 1994), the diffusion of water molecules is described by a Gaussian distribution. The signal attenuation  $E$  along the gradient direction  $\vec{r}$  is defined as

$$E = e^{-b\vec{r}^T D \vec{r}} \quad (5.9)$$

where  $b$  is the b-value and  $D$  the *diffusion tensor*, which can be written as a symmetric  $3 \times 3$  matrix

$$D = \begin{bmatrix} D_{xx} & D_{xy} & D_{xz} \\ D_{xy} & D_{yy} & D_{yz} \\ D_{xz} & D_{yz} & D_{zz} \end{bmatrix}. \quad (5.10)$$

Combining equations 5.9 and 5.10, the 6 independent parameters of the diffusion tensor can be computed when the signal attenuation is measured with at least 6 independent diffusion directions. Usually, all measurements are performed using the same b-value. Visualizing the direction of the diffusion measurements as vectors with the lengths of the b-values leads to a spherical representation of the acquisition scheme.

The diffusion tensor is often visualized as an ellipsoid as shown in Fig. 5.7. The three eigenvalues  $\lambda_1$ ,  $\lambda_2$  and  $\lambda_3$  (which, due to  $D$ 's symmetry, correspond to  $D_{xx}$ ,  $D_{yy}$  and  $D_{zz}$  respectively) describe the lengths of the ellipsoid's axes, while the remaining components of the tensor matrix define their orientation. The shape of the ellipsoid represents the anisotropy of diffusion. A spherical tensor indicates completely isotropic

diffusion, while a more cigar shaped ellipsoid indicates anisotropic diffusion with less restrictions in the direction of  $\lambda_1$ .

The shape of the ellipsoid, and accordingly the anisotropy of diffusion, is most often described by the rotationally invariant parameter *fractional anisotropy* (FA) (Basser et al., 1996) that is defined as the standard deviation of the eigenvalues divided by the average of squares, or the eigenvalues

$$FA = \sqrt{\frac{3}{2}} \frac{\sqrt{(\lambda_1 - \bar{\lambda})^2 + (\lambda_2 - \bar{\lambda})^2 + (\lambda_3 - \bar{\lambda})^2}}{\sqrt{(\lambda_1^2 + \lambda_2^2 + \lambda_3^2)}} \quad (5.11)$$

where  $\lambda_{1,2,3}$  are the three eigenvalues of the diffusion tensor and  $\bar{\lambda} = (\lambda_1 + \lambda_2 + \lambda_3)/3$  (see Eq. 5.4.1). An equivalent expression for FA that does not require the computation of  $\bar{\lambda}$  is

$$FA = \sqrt{\frac{1}{2}} \frac{\sqrt{(\lambda_1 - \lambda_2)^2 + (\lambda_1 - \lambda_3)^2 + (\lambda_2 - \lambda_3)^2}}{\sqrt{(\lambda_1^2 + \lambda_2^2 + \lambda_3^2)}} \quad (5.12)$$

For positive eigenvalues, FA ranges between zero (isotropic diffusion) and one (diffusion occurs only in a single direction).

Another frequently used index is the so called *mean diffusivity* (MD), which describes the average diffusivity in a voxel and is defined as the average of the three eigenvalues:

$$MD = (\lambda_1 + \lambda_2 + \lambda_3) / 3. \quad (5.13)$$

FA is a very sensitive but not specific index. A change in FA can be the result of change in length or width of the diffusion ellipsoid. In order to quantify these effects separately, two additional indices, namely the *axial diffusivity* (AD) or *parallel diffusivity* ( $ADC(\parallel)$ )

$$AD = ADC(\parallel) = \lambda_1 \quad (5.14)$$

and the *radial diffusivity* (RD) also called *perpendicular diffusivity* ( $ADC(\perp)$ )

$$RD = ADC(\perp) = (\lambda_1 + \lambda_2) / 2. \quad (5.15)$$

are defined.

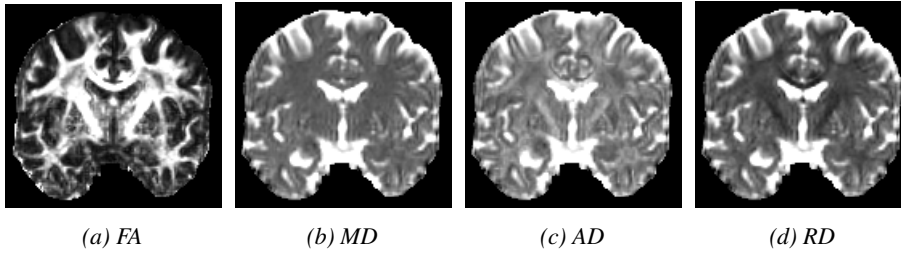


Figure 5.8: Indices of the diffusion tensor. a) fractional anisotropy (FA), b) mean diffusivity (MD), c) axial diffusivity (AD) and d) radial diffusivity (RD). Value ranges are optimized for best contrast.

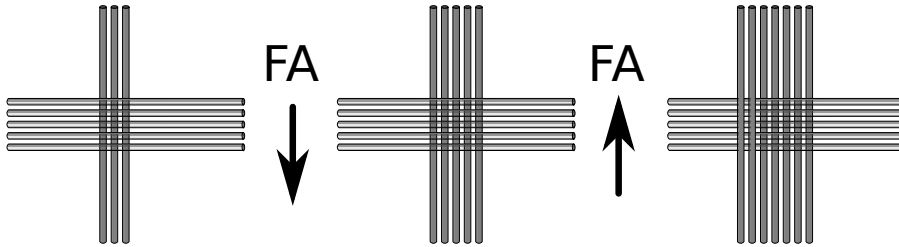


Figure 5.9: Fiber configuration influencing FA. While the vertical fiber configuration becomes constantly “stronger” from left to right but the FA first decreases and then increases.

Maps of these indices are visualized in Fig. 5.8. A practical issue of the indices derived from the diffusion tensor is the ambiguity of the biological sources that influence its values. FA for example is often associated with axonal properties like myelination, although according to Beaulieux and colleagues (2002) the most dominant factor for the diffusion profile are the axonal membranes themselves. Consequently, the configuration of fibers influences the value of FA most but is also ambiguous as described by Jbabdi and colleagues (2010) and Fig. 5.9. An increased number of fibers in one bundle in a crossing region can lead to both increased and decreased FA, depending on the number of fibers in the other bundle. Last but not least, all measures derived from DTI are scalar indices that do not differentiate different fiber bundles in a voxel.

With the low requirements on the measurement protocol, the simple mathematics that is required to compute the diffusion tensor and the sensitivity of its indices, DTI has become the most widely used model in dMRI.

As DTI assumes anisotropic Gaussian distribution as it is expected only in regions where all axonal fibers within one voxel run parallel, the model is, strictly speaking, only valid in about 10 % to 37 % of the white matter voxels in the human brain (Jeurissen et al., 2013; Schultz, 2012).

### 5.4.2 Multi-tensor

In order to circumvent some of the limitations that are characteristic for the single-tensor, models with multiple tensors have been introduced (Tuch et al., 2002; Alexander, 2005; Malcolm et al., 2009). They replace the simple Gaussian model with a mixture of  $n$  Gaussian densities.

$$E = \sum_{i=1}^n a_i \exp(-b\vec{r}^T D_i \vec{r}) \quad (5.16)$$

where  $D_i$  is the tensor matrix of the  $i$ th population and  $a_i \in [0, 1]$  with  $\sum a_i = 1$  is the volume fraction of each population.

This approach seems very attractive, as properties of different fiber bundles can be characterized separately with the well established indices of the diffusion tensor. Unfortunately, estimating the model parameters is numerically challenging as it is, compared to the single-tensor case (Eq. 5.9), no longer possible to linearize Eq. 5.16 by taking the logarithm on both sides. There are multiple solutions to increase numerical stability of fitting the multi-tensor model e.g. restricting the number of diffusion tensors (Caan et al., 2010), acquiring data with multiple b-values (Scherrer and Warfield, 2010), incorporating physiological constraints (Tuch et al., 2002) or taking neighborhood information into account (Pasternak et al., 2008).

### 5.4.3 Multi-compartment models

#### Ball-and-stick

The *ball-and-stick model* is a simple multi-compartment model, which has been introduced by Behrens and colleagues (2003; 2007). It assumes that water molecules either belong to an isotropic compartment (the ball) or are associated to one of multiple

directional compartments (the sticks) with infinite isotropy. The signal attenuation  $E$  for each diffusion-weighted measurement at each voxel can be expressed as

$$E = \left( 1 - \sum_{j=1}^N f_j \right) e^{-b_i d} + \sum_{j=1}^N f_j e^{-b_i d r_i^T R_j A R_j^T r_i}, \quad (5.17)$$

where  $d$  is the diffusivity,  $b_i$  and  $r_i$  are the b-value and gradient direction associated with the  $i$ th acquisition.  $f_j$  is the signal contributed by the  $j$ th fiber orientation and  $R_j A R_j^T$  is an anisotropic diffusion tensor that is aligned with the  $j$ th fiber orientation.  $N$  is the maximum number of fibers and  $A$  constant matrix

$$A = \begin{pmatrix} 1 & 0 & 0 \\ 0 & 0 & 0 \\ 0 & 0 & 0 \end{pmatrix} \quad (5.18)$$

which is rotated into the direction of the  $j$ th fiber by  $R_j$  (Behrens et al., 2007). The isotropic and directional compartments are all modeled by standard or specially constrained tensors, so that the ball-and-stick model can be seen as a special case of the multi-tensor model.

The model has been developed for probabilistic tractography (see chapter 5.6.2) rather than for the quantification of microstructural tissue properties. Accordingly and due to the simplicity of the model, it is, apart from the direction of fiber populations and their uncertainty, probably not possible to derive meaningful indices from the model in order to describe the tissue's micro-structure (Jbabdi et al., 2007).

### Ball-and-rackets

An extension to the ball-and-stick model, that is called *ball-and-rackets model*, has been proposed by Sotiropoulos and colleagues (2012). It explicitly models the effect of fiber fanning by using Bingham functions and represents a special case of the model introduced by Kaden and colleagues (2007).

### Composite hindered and restricted model of diffusion

The *composite hindered and restricted model of diffusion* (CHARMED) described by Assaf and colleagues (2004; 2005) combines models of extra-axonal and intra-axonal diffusion. In the extra-axonal areas the diffusion of water molecules is only hindered (not restricted) by axons and other cells, so that the diffusion process can be described with the Gaussian model. The intra-axonal water is restricted by the axon membranes, and a model of diffusion within a cylinder is used.

$$E = f_h \cdot E_h + f_r \cdot E_r \quad (5.19)$$

where  $E$  is the observed signal attenuation and  $E_h$  and  $E_r$  are the signal attenuations of the hindered and restricted compartments, respectively, that are modeled separately.  $f_h$  and  $f_r$  are the corresponding population fractions.

Multiple fiber direction can be modeled by adding terms for additional restricted compartments. For low  $q$ -values, a single diffusion tensor is sufficient to model the hindered diffusion even in configurations with multiple fiber directions (Basser and Jones, 2002).

### AxCaliber

In 2008 Assaf and colleagues proposed a method called *AxCaliber*, which is an extension to the CHARMED framework and allows to estimate the distribution of axonal diameters. With AxCaliber, different degrees of diffusion weighting as well as different diffusion times are evaluated in order to estimate the distribution of axon diameters, which leads to long acquisition times.

Until now the distribution of axonal diameters can only be estimated in voxels of a single, parallel fiber population, and where the direction is known a priori like in the optic nerve, the spinal cord or the corpus callosum.

### NODDI

Going one step further, Zhang and colleagues (2012) introduced a method called NODDI (*neurite orientation dispersion and density imaging*) that describes a three-compartment model. Intra- and extra-cellular compartments as well as *corticospinal*



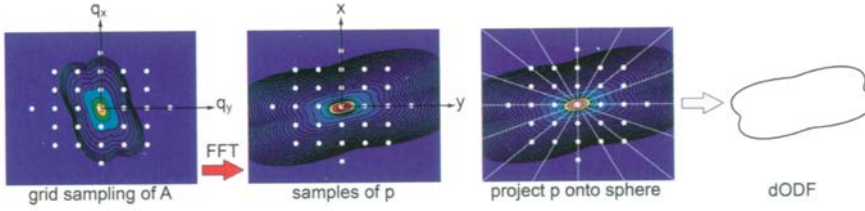


Figure 5.10: 2D schematic illustration of diffusion spectrum imaging. Signal attenuations are measured on a rectangular grid of different  $q$ -values and transformed via FFT to a grid of displacements. These displacement probabilities are then projected onto a sphere to obtain the dODF. (from (Alexander and Seunarine, 2011))

*fluid* (CSF) are modeled by an orientation-dispersed cylinder plus an anisotropic and isotropic compartment, respectively.

#### 5.4.4 Diffusion spectrum imaging

*Diffusion spectrum imaging* (DSI) (Wedeen et al., 2000; Tuch, 2002; Lin et al., 2003; Wedeen et al., 2005) is a model-free approach to describe the diffusion of water molecules. In contrast to the models described so far it uses a different acquisition protocol that measures data on a regular rectangular grid of different  $q$ -values (see Fig 5.10). With this configuration of measurements the *fast Fourier transform* (FFT) can be used to calculate the probability distribution  $p$  of the displacement of water molecules in each direction. In order to obtain a useful representation of  $p$ , the discrete representation from the FFT is projected to a sphere, which results in an *orientation density function* (ODF). As the ODF from DSI describes the diffusion of water molecules, it is called *diffusion orientation density function* (dODF) and in the case of DSI defined as

$$dODF_{DSI}(\hat{x}) = \int_0^\infty f(\alpha) p(\alpha \hat{x}) d\alpha \quad (5.20)$$

where  $\hat{x}$  is a unit vector in the direction of  $x$ .  $\alpha$  is the index of the contour, and  $f(\alpha)$  weights the influence of the different contours of  $p$ . Initially  $f(\alpha)$  was set to 1 (Wedeen et al., 2000), but was later changed to  $f(\alpha) = \alpha^2$  (Wedeen et al., 2005), which emphasizes higher frequencies and results in sharper peaks (Alexander and Seunarine, 2011).

The acquisition requirements for DSI are quite high (Wedeen et al., 2000; Kuo et al., 2008). They require 203 or 515 measurements, with a b-value of up to 4000 s/mm<sup>2</sup> or 6500 s/mm<sup>2</sup>, respectively. Consequently, very strong gradient systems are needed in order to reduce the gradient pulse time as much as possible (Alexander and Seunarine, 2011).

### 5.4.5 Q-ball

*Q-ball imaging* (Tuch, 2002; Tuch, 2004; Descoteaux, 2008; Aganj et al., 2010) is a simplification of DSI and uses a spherical acquisition scheme with a single shell, reducing the acquisition time compared to DSI.

The dODF is approximated with the *Funk Radon transform* (FRT) (Funk, 1915) that maps one function of the unit sphere to another. To compute the dODF, for every direction  $\hat{x}$ , the values of the signal attenuation  $E(\mathbf{q})$  on the great circle of the plane perpendicular to  $\hat{x}$  through the origin are integrated as visualized in Fig. 5.11. Mathematically this can be expressed as

$$dODF_{Qball}(\hat{x}) = \int_{\mathcal{C}(\hat{x})} E(\mathbf{q}) d\hat{\mathbf{q}} \quad (5.21)$$

where  $\hat{x}$  is the unit vector in the direction  $x$ , and  $E(\mathbf{q})$  is the signal attenuation on the great circle  $\mathcal{C}(\hat{x})$  (Alexander and Seunarine, 2011).

### Enhancements

While Tuch implemented a numerical solution to solve the FRT, Descoteaux (2008, 2009) introduced a fast and robust analytical solution for the reconstruction of Q-balls. This is achieved by proving a new corollary of the Funk-Hecke theorem and using spherical harmonics (see section 5.5) in order to obtain a simplification of the FRT.

Aganj and colleagues (2010) proposed a new solution which, considering the solid angle factor, uses the mathematically correct definition of the ODF and results in a normalized ODF that also produces sharper lobes than previous implementations.

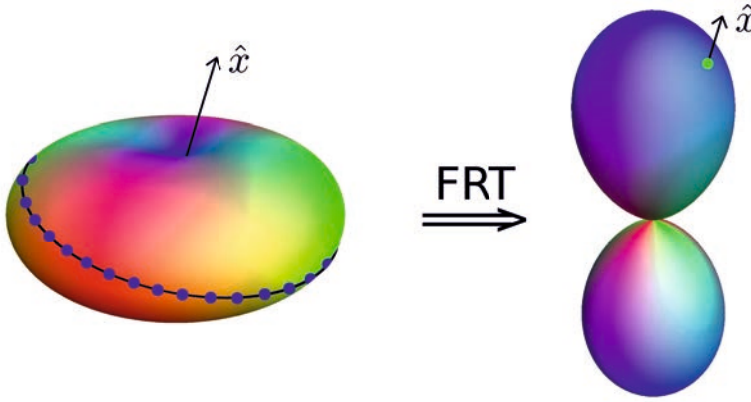


Figure 5.11: Funk Radon transform to compute the  $q$ -ball's  $dODF$ . For every direction ( $\hat{x}$ ) samples (blue spots) from the signal attenuation profile (left) on a plane perpendicular to  $\hat{x}$  are integrated in order to obtain values of the  $dODF$  (right, green spot).

### Generalized fractional anisotropy

In analogy to the FA index from the diffusion tensor Tuch (2004) defined the *generalized fractional anisotropy* (GFA) as

$$GFA = \frac{\sqrt{\int (dODF(\hat{x}) - \overline{dODF})^2 d\hat{x}}}{\sqrt{\int dODF(\hat{x})^2 d\hat{x}}} \quad (5.22)$$

with  $\overline{dODF} = (4\pi)^{-1} \int dODF(\hat{x}) d\hat{x}$ .

It has been shown (Gorczewski et al., 2009) that GFA computed from the original  $q$ -ball and FA have a linear dependence. However, it should be noted that the GFA behaves differently when it is computed with consideration of the solid angle compared to the original version (Fritzsche et al., 2010).

### Peak fractional anisotropy

Ghosh and Deriche (2011) introduced an index called *peak fractional anisotropy* (PFA), which describes the geometric characteristic of every peak in the ODF. An ellipsoid is fitted into each lobe of the ODF, so that the ellipsoid's main direction and length

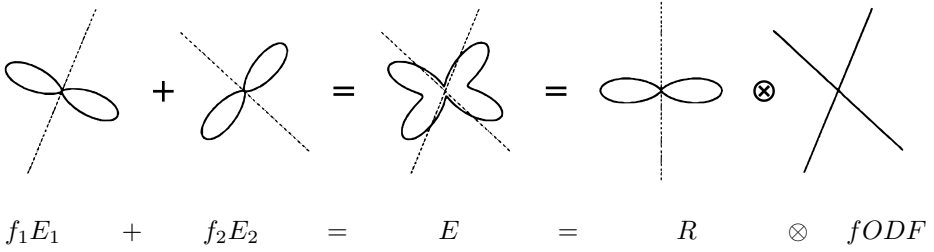


Figure 5.12: Principle of spherical deconvolution. The signal attenuation profile  $E$  is the sum of the signal attenuation profiles of all fiber bundles  $E_i$  with their volume fractions  $f_i$ . It can also be considered as the result of the convolution of the  $fODF$  with the kernel  $R$ . The deconvolution inverts the convolution process and computes the  $fODF$  from the a signal attenuation profile and the kernel. (Modified reprint from (Tournier et al., 2004))

correspond with the lobe's direction and length, respectively. The width is defined by the curvature at the lobe's peak. This ellipsoid establishes a correspondence with a fiber bundle specific diffusion tensor and allows to derive the same well known and established indices for each fiber bundle separately.

### 5.4.6 Spherical deconvolution

*Spherical deconvolution* (SD) (Anderson and Ding, 2002; Tournier et al., 2004; Kaden et al., 2007; Descoteaux et al., 2009; Dell'Acqua et al., 2010) follows a completely different concept. The models introduced so far describe the diffusion profile in a voxel that leads to implicit conclusions about the directional fiber configuration and microstructural properties. In contrast, SD assumes that the diffusion characteristics of all fiber populations found in the brain are identical (Tournier et al., 2004) and uses the signal profile of a completely parallel fiber population as convolution kernel.

The signal attenuation profile  $E$  measured in a voxel is considered as the result of the convolution of the directional fiber configuration described by the *fiber orientation density function* (fODF) with the kernel (see Fig. 5.12). Conversely, deconvolving the measured signal attenuation profile  $E$  with a kernel  $R$  directly results in the  $fODF$  in that voxel.

$$E = fODF \otimes R \quad (5.23)$$

The name "spherical deconvolution" (also known as "spherical harmonic deconvolution") originates from *spherical harmonics* (SH) (see chapter 5.5 for details), which are used to simplify the computation of the deconvolution and to represent the fODF. Spherical harmonics form a set of orthonormal basis functions on the sphere, analogous to the Fourier series in Cartesian space. Accordingly, the shape of the fODF (as well as the signal attenuation profile and the kernel) is described by a number of coefficients that weight the different basis functions. The coefficients are enumerated by order and phase factor. While the angular frequency increases with the order, the phase factor describes different shapes (see Fig. 5.13, negative values of the basis functions are colored gray). As the profile of the signal attenuation is symmetric to the center, only symmetric SH basis functions are required. These are, when using e.g. the orthonormal basis proposed by Descoteaux (2006), the functions of even order.

The spherical harmonic coefficients for the signal attenuation profile can be computed by a simple linear least squares fit (Alexander et al., 2002), but require at least as many independent diffusion directions as coefficients. In practice it might be advisable to measure more directions than at least required for the desired order to compensate for noise in the measurement.

Higher orders of SD do not only require more measurements, but are also prone to produce biologically impossible negative spurious lobes in the fODF. These effects can either be handled by filtering (Tournier et al., 2004) or suppressing negative lobes (Tournier et al., 2007). A simple low-pass filter multiplies the coefficients with a factor depending on the order. Tournier (2004) proposed the following filter that heavily suppresses higher order coefficients:

coefficient order	0	2	4	6	8	10	12
factor	1	1	1	0.8	0.1	0.02	0.002

The disadvantage of such a low-pass filter is the loss of angular resolution. To circumvent this issue, Tournier (2007) proposed a method to suppress negative lobes without sacrificing the angular resolution. It is referred to as *constrained spherical deconvolution* (CSD). CSD is an iterative approach based on a modified Tikhonov regularization method (Hansen, 1994). In a first step, an initial estimate of the fODF is obtained using only lower order coefficients. Then, negative lobes are identified and suppressed using higher order coefficients. Finally, the fODF is obtained again with the new coefficients

that are used as initial guess for the next iteration. In the implementation of Tournier, negative lobes are significantly reduced but not completely eliminated.

Dell’Acqua and colleagues proposed a deconvolution performed by a modified version of the Richardson-Lucy algorithm (Dell’Acqua et al., 2007), which reduces noise by separating an isotropic compartment from the anisotropic fibers (Dell’Acqua et al., 2010). A comparison of CSD (Tournier et al., 2007) and the Richardson-Lucy algorithm (Dell’Acqua et al., 2010) is provided by Parker and colleagues (2012).

Kaden and colleagues presented a deconvolution method that parameterizes the fODF by a finite number of Bingham distributions (Kaden et al., 2007).

### **Peak length**

Dell’Acqua and colleagues (2013) as well as Raffelt and colleagues (2012) derived an index from fODFs by extracting the length of every fODF peak as a bundle specific index. This index describes the density of fibers in the direction of the peak, and hence holds biophysical meaning for every fiber bundle separately.

### **Indices based on Bingham functions**

Fiber bundles are composed of many axons that are not necessarily strictly aligned in a single direction and are reflected by so-called lobes (i.e. distinct local maxima) of the fODF. Hence, the microstructural properties of fiber bundles are better described by the surrounding of a local maximum of the fODF than just by a single direction. Using spherical harmonics it is easy to compute values of the fODF in a distinct direction, but it is not possible to derive shape parameters from the SH coefficients directly. Therefore, Raffelt and colleagues (2014) developed a method to fit a Bingham function (scaled Bingham distribution) into the fODF’s local maxima. The Bingham distribution is an antipodally symmetric distribution on the sphere, analogue to the general bivariate normal distribution, and is defined by parameters that can be directly used to quantify the shape of fODF lobes and to directly describe the statistical moments of the fiber direction distribution within a bundle.

In order to evaluate the presented method and to quantify directional characteristics of fiber bundles, four indices were used (Raffelt et al., 2014):

- The bundle specific *Fiber Density* (FD) is the integral of angular fiber densities and is computed by integrating the corresponding Bingham function. If the number of axons in the kernel voxels is known, FD can be measured absolutely in  $\frac{1}{mm^3}$ . Otherwise, FD represents the dimensionless relative fiber density compared to the kernel voxels.
- The *maximal Angular Fiber Density* ( $AFD_{max}$ ) in a bundle (see section “Peak length” above) is the local maximum of the fODF and is represented by the scaling parameter of the respective Bingham function. Similar to FD,  $AFD_{max}$  can be measured in  $\frac{1}{mm^3 \cdot rad}$  or expressed as relative value in the unit  $\frac{1}{rad}$ . This index is not directly analyzed; it is mentioned in this list only for defining the Fiber Spread (see below).
- The *Fiber Spread* (FS) of a fiber bundle is measured indirectly and is defined as the ratio of FD and  $AFD_{max}$ :

$$FS = \frac{FD}{AFD_{max}} \quad (5.24)$$

It represents the angular width of a uniform distribution with the amplitude  $AFD_{max}$ . This opening angle can range between 0 and  $\pi$ .

- The *Fiber Fraction* (FF) describes how dominant (in terms of fiber density) the fiber bundle of interest is compared to all fiber bundles in that location. For N (here  $N \leq 3$ ) crossing-fiber bundles, the fiber fraction of the bundle of interest (b) is defined as

$$FF_b = \frac{FD_b}{\sum_{i=1}^N FD_i}. \quad (5.25)$$

A visualization of these indices and a comparison with FA is provided in chapter 6.4.2, while a validation of stability in regards to different deconvolution kernels is presented in chapter 7.2.

## 5.5 fODF representation with spherical harmonics

Similar to the Fourier series in the Cartesian space, spherical harmonics form a set of orthonormal basis functions on the sphere. Descoteaux and colleagues (2006) proposed the following basis functions:

$$Y_\ell^m(\theta, \phi) = \sqrt{\frac{2\ell + 1}{4\pi} \frac{(\ell - m)!}{(\ell + m)!}} P_\ell^m(\cos(\theta)) e^{im(\phi)} \quad (5.26)$$

where  $P_\ell^m$  is an associated Legendre polynomial. Each function can be identified by its order  $\ell$  and its rank or phase factor  $m$ .

When using spherical harmonics to describe the shape of a signal attenuation profile or ODF, certain assumptions can be made regarding the symmetry. As the diffusion process is symmetric around the origin, only antipodally symmetric basis functions are required. In the set of basis functions defined in Eq. 5.26, functions of even order are antipodally symmetrical while those of uneven order are antipodally antisymmetric (Descoteaux et al., 2006). With an index  $j$  that is computed as

$$j(\ell, m) = \frac{1}{2} (\ell^2 + \ell + 2) + m \quad (5.27)$$

where  $\ell = 0, 2, 4, 6, \dots, L$  with  $L$  being the highest order and  $m = -\ell, \dots, 0, \dots, +\ell$ , a modified spherical harmonic base can be defined as

$$Y_j(\theta, \phi) = \begin{cases} \operatorname{Re} \left( Y_\ell^{|m|}(\theta, \phi) \right), & \text{if } m > 0 \\ Y_\ell^m(\theta, \phi), & \text{if } m = 0 \\ \operatorname{Im} \left( Y_\ell^m(\theta, \phi) \right), & \text{if } m < 0 \end{cases} \quad (5.28)$$

The angular frequency increases with order  $\ell$ , while the phase factor describes different shapes, which can be seen in Fig. 5.13. Consequently, spherical harmonics of higher orders provide a higher level of detail and also a higher angular resolution. The



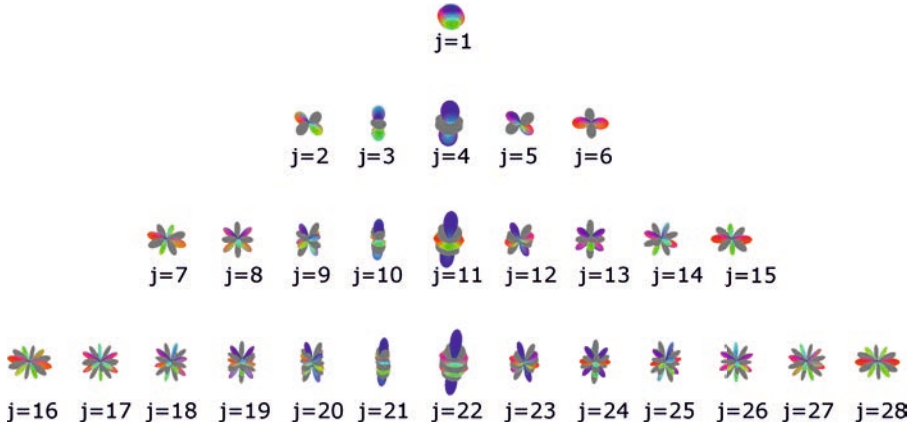


Figure 5.13: Glyph representation of spherical harmonic base functions. The rows show the glyphs of order 0, 2, 4 and 6, respectively, while the columns define the rank. Negative lobes are colored gray.

function  $F$  can be computed as a series expansion of the spherical harmonics

$$F(\theta, \phi) = \sum_{j=0}^J c_j Y_j(\theta, \phi) \quad (5.29)$$

where  $c_j$  are the weighting coefficients and  $J = \frac{1}{2}(\ell + 2)(\ell + 1)$  is the number of coefficients and base functions that depends on the spherical harmonic order.

As the series are truncated and hence miss the higher frequencies, spherical harmonics cannot represent the signal attenuation profile exactly, but only as a smooth approximation as shown in Fig. 5.14.

## 5.6 Reconstruction of white matter fiber tracts by tractography

### 5.6.1 Deterministic tractography

A visually appealing application of dMRI is tractography. Here, the most prominent directions of nerve fiber bundles are extracted from the local models and are used for

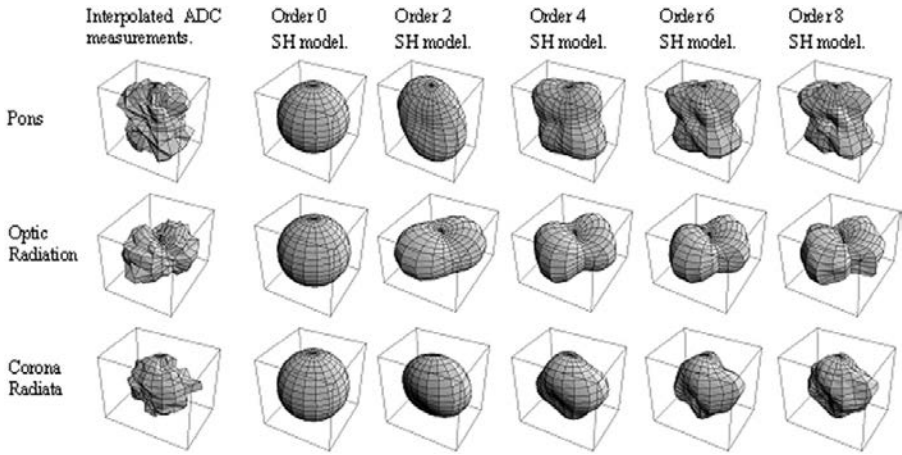


Figure 5.14: Signal attenuation profile approximation with spherical harmonics of different order. Typical signal attenuation profiles from voxels in the pons, optic radiation and corona radiata (left) together with SH models of orders 0, 2, 4, 6 and 8 (second from left to right). (Reprint from (Alexander et al., 2002))

retrieving the course of white matter fiber pathways (Mori et al., 1999; Basser et al., 2000; Mori and van Zijl, 2002).

One of the first methods for tractography has been introduced by Mori and colleagues (1999). It uses the diffusion tensor as a local model and propagates the path as a streamline according to the main direction of the local tensors from one voxel to the next until a stopping criterion is fulfilled. The stopping criteria most frequently used are a very low anisotropy and a high curvature of the track (see Fig. 5.15). Several variations and improvements have been published since then. These include, for example, tensor deflection (Lazar et al., 2003) where the direction of the local model is not followed strictly in every voxel, but the incoming track's direction is deflected according to the tensor's anisotropy.

Tractography has also been adapted to multiple tensor and higher order local models that are able to distinguish multiple fiber directions (Wedeen et al., 2008; Descoteaux et al., 2009; Malcolm et al., 2010; Tournier et al., 2012) to improve the reconstruction in regions of crossing fibers that cannot be described adequately by the diffusion tensor (for a review, see, Lenglet et al., 2009). There are two limiting issues to all these deterministic streamline approaches: error propagation and a bias for following only

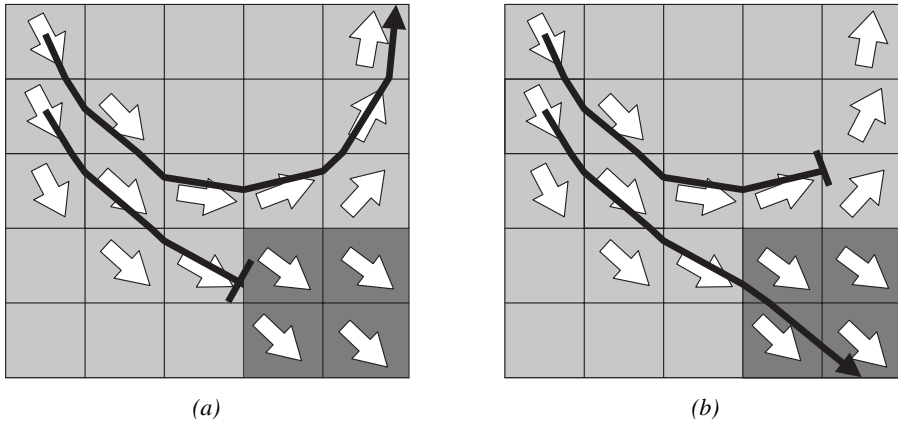


Figure 5.15: Principle of deterministic tractography. The tract is propagated from one voxel to the next in the direction of the principle direction of the diffusion tensor (white arrows). The propagation is stopped when either a) the fractional anisotropy is lower than a defined threshold (darker gray fields) and/ or b) when the track would bend too sharp. (reprint from (Mori, 2007))

the central line of fanning fiber bundles. Error propagation occurs if the diffusion profile in a voxel is corrupted by, for example, noise, and the track is continued in the wrong direction. This error accumulates as tracking progresses. The bias for major fiber bundles results from the computation of the single best direction, in most cases the locally most probable direction, that is then followed. In areas where fibers are crossing or fanning, only one of the multiple, similarly probable, directions is chosen, the others are neglected.

### 5.6.2 Probabilistic tractography

Probabilistic tractography (Koch et al., 2002; Behrens et al., 2003; Parker and Alexander, 2005; Anwander et al., 2007; Kaden et al., 2007; Jeurissen et al., 2011) is an approach to ameliorate these problems. In contrast to streamline tractography the probabilistic approach does not produce distinct pathways. Accordingly, probabilistic tractography cannot be used for virtual dissection of specific fiber bundles, as it is possible with deterministic tractography. Instead it results in a set of tracks for each seed location. This set of tracts can be transformed into a visitation map approximating the probabilities of all voxels to be connected to the seed location (see Fig. 5.16). This

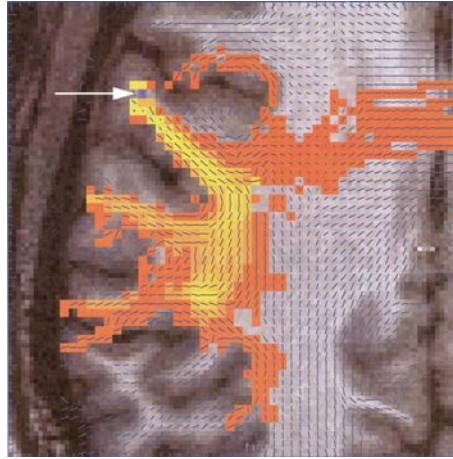


Figure 5.16: Visitation map from probabilistic tractography. Several tracks were started in the seed location (white arrow) to propagate through the tensor field. Voxels that have been touched by the probabilistic streamlines are colored from red to yellow. The more tracks touched a voxel the more yellow it appears. The short blue lines indicate the tensors' principle directions. (reprint from (Koch et al., 2002))

is achieved by starting multiple (often several thousand) tracks in every voxel, and not only following the principle directions, in each voxel but varying the angle randomly according to the estimated uncertainty of the main directions or according to a local fiber orientation density function.

As can be seen in Fig. 5.16, it is difficult to derive a real measure of connectivity from probabilistic tractography. A high value in the visitation map does not necessarily mean a high connectivity to the seed locations, as fibers might just pass the area without entering the cortex (like e.g. in the corpus callosum). On the other hand, areas that are far away from the seed location, logically have a lower value in the visitation map than close-by areas, because the long pathway offers more possibilities for the tracks to deviate from the optimal course. Up to now no real solution has been proposed to this problem. Another issue of probabilistic tractography shows up when comparing the connectivity between subjects. It is not always clear if the reason why one connection receives lower probability values is that it is weaker or that another pathway is more probable and attracts more tracks, so that less reach the area of interest.

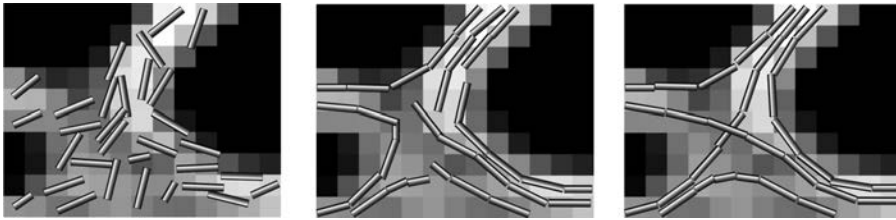


Figure 5.17: Principle of global tractography with self-organizing particles. Fibers are built with small line elements that contribute an anisotropic term to the simulated diffusion weighted signal. Optimizing the number and orientation of the elements adjusts the simulated to the measured signal. (reprint from (Kreher et al., 2008))

### 5.6.3 Global tractography

Global tractography methods abandon the sequential principle, which is inherent in the previously described techniques, and which is responsible for error propagation. One type of global tractography (Kreher et al., 2008; Fillard et al., 2009; Reisert et al., 2011), which is visualized in Fig. 5.17, uses self-organization principles and builds all tracks simultaneously by joining multiple particles modeled into each voxel.

Another type of global tractography, firstly proposed by Tuch (2002), describes a method of modeling fiber pathways with cubic splines, which produces smooth curves between two fixed endpoints that are optimized through the field of diffusion directions extracted from q-ball imaging. Within the optimization process, control points of the curve are dynamically added or removed. The result is the most probable pathway of fibers between the two locations under the assumption that an axonal connection does indeed exist.

Jbabdi and colleagues (2007) used a Bayesian framework for evaluation of the most probable pathway using several parameters like local diffusion properties, fiber orientations, amount of anisotropy and noise. The major issues for this method are, according to the authors, the planar initialization and connections where multiple pathways exist that pass through different regions of the brain (e.g. the ventral and dorsal connections between Broca's and Wernicke's Area).

For a detailed review of tractography methods refer to (Behrens and Jbabdi, 2009).

## 5.7 Comparing microstructural differences within or between groups

### 5.7.1 Voxel-based analysis

*Voxel-based morphometry* (VBM) (Ashburner and Friston, 2000; Good et al., 2001) is a method for evaluation of the gray matter volume or concentrations in every voxel. In order to obtain a voxel-wise correspondence across subjects, images are warped onto a common template. Segmentation produces probability maps of different tissue compartments like gray matter, white matter and cerebrospinal fluid. These probability maps (usually only of gray matter) are then smoothed with a Gaussian kernel in order to increase the signal to noise ratio, to ensure Gaussianity required for correction for multiple comparisons with random-field theory (Worsley et al., 1992), to increase sensitivity for specific effect sizes and to compensate for misalignments (Ashburner and Friston, 2001; Jones et al., 2005). Optionally, the probability maps are modulated with the Jacobian determinants of the deformation field in order to preserve concentrations or volumes (Good et al., 2001).

With the same protocol, smoothed maps of dMRI indices like FA can be analyzed instead of the tissue probability maps (Sommer et al., 2002; Snook et al., 2007; Seok et al., 2007). This is called *voxel-based analysis* (VBA) because it compares quantitative values instead of the morphometry of certain brain structures.

The advantage of this method is that no a priori hypotheses about the location of anatomical differences are required. Still, the expected effect size should be known in order to define a smoothing kernel of appropriate size. The main disadvantage is that imperfections in the spatial normalization step may be interpreted as differences in index values. Due to the required smoothing, this method cannot compare direction dependent indices.

### 5.7.2 Region-based analysis

In *region-based analysis* (RBA) (Snook et al., 2007; Faria et al., 2010), regions of interest (ROI) are defined in every individual dataset. The value of the index of interest is averaged within this region. These regions can either be drawn manually or mapped

automatically by aligning an atlas with the desired ROI(s). While the manual method is very laborious and might impose rater specific biases, the automatic registration with an atlas bears the risk of imperfect alignments and the risk of bias due to macroanatomical differences between the groups.

In both cases, the user has to have a distinct hypothesis about the location and size of the expected dissimilarity.

If there are no a priori hypotheses regarding the expected differences, an atlas (Mori et al., 2008; Lim et al., 2013) with multiple regions covering the whole brain can be aligned with each dataset. Nevertheless, the selected atlas has to be suitable for the current research question as well as fit the data. With very small ROIs, one cannot be sure that in every subject the same anatomical or functional region is selected. This is due to anatomical variations and also due to possible misalignments from the registration process. Larger ROIs, on the other hand, are less sensitive to anatomical variations and registration errors. They also require larger effect sizes to become significant. The smaller the ROIs, the more are required to cover the whole brain area. This imposes the risk of type II error when correcting for multiple comparisons. Actually, the tests are not independent, as axonal pathways might pass through multiple ROIs. As volumes of the regions and the number of neighboring ROIs vary, cluster based approaches for the correction of multiple comparisons are difficult to define.

The advantage of this method is that unsmoothed values in well defined ROIs can be compared across or within groups of subjects. If there is only a single ROI defined, it is not even necessary to correct for multiple comparisons because only one test is performed. On the downside, precise a priori knowledge is required to define distinct ROIs, otherwise the analysis of the whole brain area becomes statistically challenging.

The possibility to evaluate direction dependent indices is rather theoretical. If the strength of fiber populations in a region is very discriminative, it would be possible to extract indices of the dominant and minor population separately for comparison. The number of regions where this condition is stable enough for analysis might be quite limited.

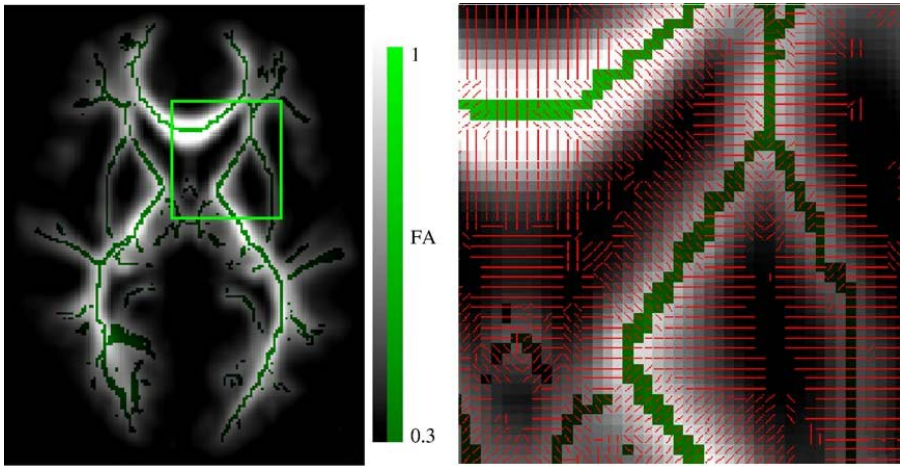


Figure 5.18: Principle of tract-based spatial statistics (TBSS). A common WM skeleton (green) is computed from an average of all normalized FA maps. Then, the maximal FA values of each subject are projected perpendicular to the skeleton (red lines). The skeleton forms a common reference system that enables a voxel-wise comparison of related maximal FA values. (reprint from (Smith et al., 2006))

### 5.7.3 Tract-based spatial statistics

With *tract-based spatial statistics* (TBSS<sup>2</sup>) as introduced by Smith and colleagues (2006), a common skeleton of white matter is created and serves as a reference frame for all subjects. First, the FA maps of all subjects are normalized to a standard template. Then a one-pixel wide skeleton is created from the average of all normalized FA maps. Due to normalization this skeleton approximately fits to all subjects. Finally, the maximal FA values of each subject are projected perpendicular onto the skeleton as shown in Fig. 5.18. This projection corrects for small misalignments of the individual subject with the common skeleton. After the skeleton has been defined based on the FA maps, also other rotationally invariant indices than FA (like e.g. axial, radial or mean diffusivity) can be projected onto the skeleton and compared across subjects.

One drawback of the method is that due to very low anisotropy values, the skeleton cannot represent areas of heavy crossings accurately. Also, the method indicates where in the brain differences exist but not the connections that are actually affected. Using

<sup>2</sup><http://fsl.fmrib.ox.ac.uk/fsl/fslwiki/TBSS>



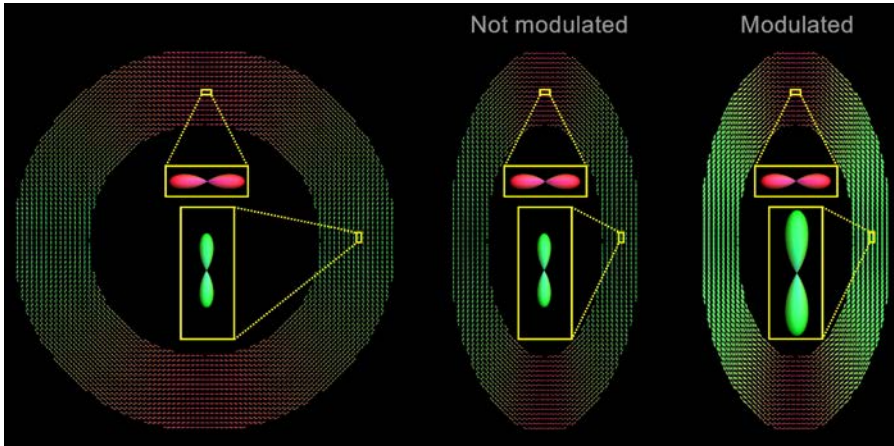


Figure 5.19: Effect of fODF modulation shown on a “ring” phantom. The original ring is depicted on the left. Compressing the ring along the horizontal axis increases the fiber density in the vertical but not the horizontal line. This increase of fiber density (resulting in larger glyphs) is accounted for through modulation (right) but not when the fODFs are not modulated (middle). (modified reprint from (Raffelt et al., 2012))

the maximal FA value is possible, because the index maps are implicitly smoothed during the normalization process so that outliers due to noise or measuring artifacts are smoothed out.

The method has been extended by Jbabdi and colleagues (Jbabdi et al., 2010; Douaud et al., 2011) in a way that handles direction dependent *partial volume fractions* (PVF) from the ball-and-stick model and potentially indices of other crossing-fiber models.

#### 5.7.4 Raffelt’s method

Raffelt and colleagues (2012) perform a voxel-based comparison of the fiber orientation density. First, the data sets are aligned using a non-linear transform. Then fODFs are modulated to account for changes that occur during spatial normalization (see Fig. 5.19). In every voxel amplitudes of the fODF are sampled in 200 directions. For each direction fODF amplitudes exceeding a defined threshold are compared between the groups, resulting in up to 200 t-statistics per voxel. This method indicates the location in the brain where differences between groups occur, but similar to TBSS, it

does not directly show which fiber pathways or connections are affected, or what the anatomical discrepancy might be.

### 5.7.5 Tract-based analysis

In order to analyze distinct fiber pathways that connect functional regions, several methods of *tract-based analysis* (TBA) have been developed. In the simplest form, tractography is used for defining a region of interest as the volume occupied by the pathway between two defined areas in the brain. As proposed, for example, by Lebel and colleagues (2008), indices of diffusion models like FA are averaged in this ROI for each dataset and statistically evaluated. More advanced methods of TBA also take the spatial arrangement of the index values into account by parameterizing the tractography streamlines along their arc length and by summarizing the indices according to their position between the two regions of interest. The difficulty with this approach is that the definition of correspondences along the tract is not trivial. Several solutions to this have been proposed (Gong et al., 2005; Corouge et al., 2006; O'Donnell et al., 2009; Colby et al., 2012) that all measure absolute or relative distances, either on some central line or on all streamlines. Malcolm and colleagues (2009) have presented a study where they compare FA, trace and eigenvalue ratio of a single-tensor and a two-tensor model. This method actually isolates some bundle-specific information but uses rather unspecific indices.

As many fiber tracts in the brain have a rather sheet-like appearance, Yushkevich and colleagues (2008) model sheet-like tracts by a medial representation to reduce data dimensionality and average tensor-based features onto this medial representation.

Most of these methods have been applied to rotationally invariant indices. One has to keep in mind that, if a fiber tract crosses voxels with multiple fiber orientations, part of the information reflected by the index does not refer to that tract. As many of the white matter voxels indeed contain more than one fiber population (Behrens et al., 2007; Schultz, 2012; Jeurissen et al., 2013), it is of great interest to develop more methods that can handle crossing fibers adequately in order to eliminate information that is not associated with the tract of interest and to improve specificity with regards to the underlying tissue microstructure.



## 6 | Methods

### 6.1 Overview

The framework presented in this thesis consists of multiple steps that are described in detail in this chapter. At first, the data detailed in section 6.2 are preprocessed following the procedure described in section 6.3. The computation of the local model and the biophysical meaningful indices is specified in section 6.4. Section 6.5 introduces *Plausibility Tracking* - the core method of this thesis. Applications of Plausibility Tracking including the comparison of direction dependent indices across subjects are presented in section 6.6

### 6.2 MRI data

Data from nine children (five girls, mean age 7.0 years, stddev 1.1) and nine adults (five female, 27.8 years, stddev 2.7) previously presented by Brauer and colleagues (2011; 2013) were used, when not stated otherwise. The data were acquired on a Siemens 3T Trio scanner with 1.7 mm isotropic voxel size, GRAPPA acceleration factor 2.  $3 \times 60$  diffusion directions with a b-value of  $1000 \text{ s/mm}^2$ , and 21 images without diffusion weighting (b0 images) were measured for each subject. Anatomical images were acquired with T1 and T2 weighting in 1.0 mm resolution. All subjects were right handed and healthy. Written informed consent was obtained from the participants in accordance with the ethical approval from the University of Leipzig. Children gave verbal assent prior to scanning, and written consent was obtained from their parent or guardian. In order to minimize effects due to different brain sizes adults with relatively

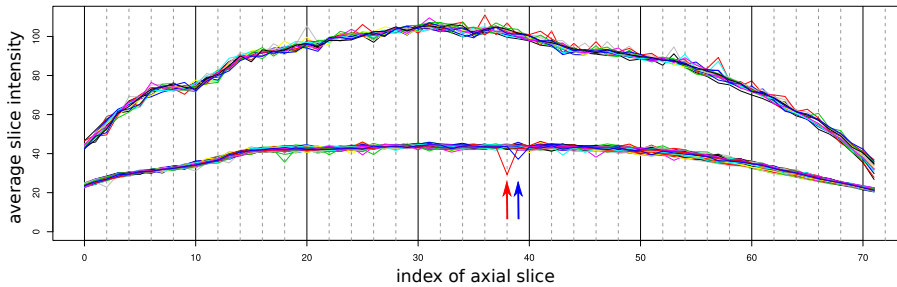


Figure 6.1: Average intensities of axial slices from dMRI volumes of a single subject. Each line represents a volume in the dMRI dataset. The average intensities are plotted for each axial slice. Slices with signal dropout due to subject motion can be identified as their average intensity is lower than that of the neighboring slices. Two examples are indicated by red and blue arrows. Volumes without diffusion weighting are generally brighter and appear above those with diffusion weighting.

small heads were selected for the study. A t-test revealed no significant difference in brain size between children and adults ( $p=0.45$ ).

## 6.3 Preprocessing

### 6.3.1 Removal of corrupted volumes

Before processing the data, the few dMRI volumes corrupted by movement of the participants were removed from the datasets. First, an automatic method was used to remove volumes of low quality. The algorithm is based on the fact that motion during the acquisition attenuates the signal in a slice. Usually the average voxel intensity of two consecutive slices (interleaved acquisition) does not change significantly. Only when motion extinguishes the signal in parts of a slice, its average voxel intensity differs greatly from its neighbor's intensity and indicates corruption of the volume. A difference in intensity is considered significant, if it is greater than three times the median of all differences. This threshold is defined separately for the b0 volumes and the diffusion weighted data. Volumes are removed from the data set if they hold at least one slice which is identified as corrupted.

Fig. 6.1 shows the average values of the axial slices from the dataset of one single subject. Every colored line represents one dMRI volume, and the average intensity

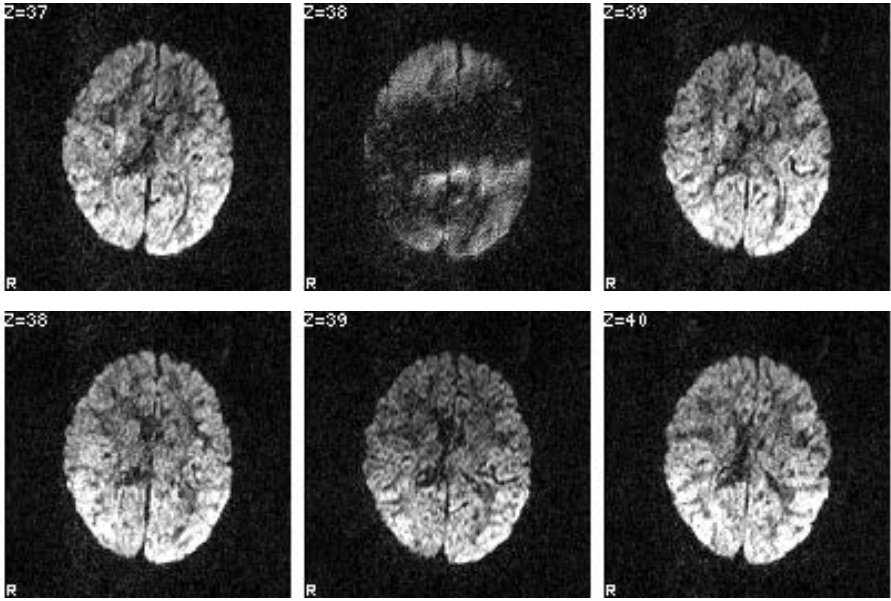


Figure 6.2: Consecutive axial slices from two different volumes with signal dropout due to motion. The signal dropout in the lower volume is significantly less severe than in the upper volume but still detectable as can be seen in Fig. 6.1.

is plotted for every axial slice. Volumes without diffusion weighting ( $b=0$ ) are much brighter and consequently appear above the volumes with diffusion weighting. The 38<sup>th</sup> axial slice (red arrow) of the volume represented by a red line is significantly darker than its neighboring slices. This indicates a signal dropout leading to a rejection of this volume. This slice is shown together with its neighboring slices in the upper row of Fig. 6.2. The same figure also shows consecutive slices of another volume that is less severely corrupted in axial slice 39 (visualized as blue line with blue arrow in Fig. 6.1).

In a following control step visual inspection of the datasets ensured the satisfactory quality of the remaining data. It was not necessary neither to remove further volumes nor to re-add automatically rejected volumes. The data sets used for further analysis have 185 to 198 out of 201 volumes.

### 6.3.2 Spatial normalization and interpolation

The complete analysis described in this thesis was performed on 1.0 mm isotropic voxel size. This resolution was chosen as a compromise between accuracy and speed. All indices and fODFs were computed in advance voxel by voxel and accessed through nearest-neighbor interpolation from then on. This dramatically reduces computational costs of recurring interpolation during the optimization process (see below), but provides finer grained information than the original 1.7 mm voxel size. To avoid multiple interpolation operations on the diffusion weighed images, motion correction, alignment with the MNI coordinate system (Collins et al., 1998) as well as interpolation to 1.0 mm isotropic voxel size were performed in a single step. Best results were achieved through the following protocol: Performing motion correction on the original dMRI data using FSL (Smith et al., 2004; Woolrich et al., 2009) (<http://fsl.fmrib.ox.ac.uk/fsl/fsl-4.1.9>), separating background from the dMRI volumes and computing an FA map, rigidly aligning this FA map with an FA map in MNI space (Jones and Cercignani, 2010) and transforming the average b0 image accordingly. Aligning all dMRI volumes to the b0 image and correcting the gradient vectors with the same transformation. This removed the volume-shifting and affine distortion effects of subject movements and resampled the diffusion data to 1.0 mm isotropic voxel size with a single trilinear interpolation. Distortions due to eddy currents were sufficiently suppressed by the double spin echo sequence used for the acquisition so that no explicit correction was necessary.

### 6.3.3 Brain extraction

The brain region was determined using FSL's brain extraction tool (*bet*). A student's t-test revealed no significant difference in brain volume between children and adults ( $p=0.45$ ).

### 6.3.4 Creation of white matter mask

A mask for white matter region was defined in order to restrict the analysis to that region. Standard approaches either apply a threshold on the FA map or compute a white matter probability map from the anatomical T1 weighted image. Here, a

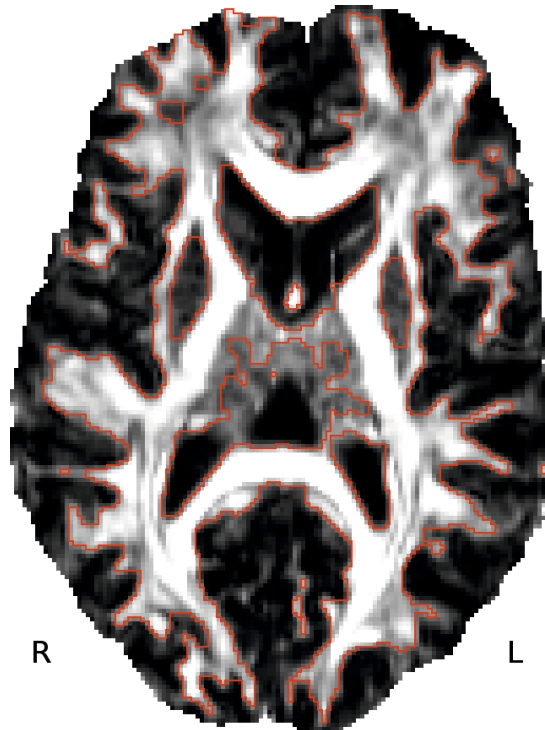


*Figure 6.3: Outline of the white matter mask obtained from segmentation of FA map.*

combined method is used. Due to small non-linear distortions in the dMRI datasets caused by susceptibility artifacts, computing the white matter mask based on the T1 weighted image would result in a map that is not perfectly aligned with the diffusion data. Thresholding the FA map holds the risk of producing holes in crossing regions where the FA values are low. SPM's (<http://www.fil.ion.ucl.ac.uk/spm>) segmentation algorithm (Ashburner and Friston, 2005) was applied to the FA map. As the FA map is perfectly aligned with the diffusion data, and the segmentation and registration algorithm incorporates not only intensity but also spatial information, this method results in highly reliable white matter probability maps that can be thresholded to obtain the white matter mask as shown in Fig. 6.3.



## 6.4 Local modeling

### 6.4.1 Spherical deconvolution

CSD as implemented in MRtrix (Tournier et al., 2012) (<http://www.brain.org.au/software/mrtrix>) was used to compute the fODF in every voxel. For this approach it is necessary to have some knowledge of the signal attenuation that would be generated from completely parallel fibers (deconvolution kernel). The voxels that are used to compute this kernel response should be chosen from regions where all axonal fibers within one voxel run in the same direction.

A white matter skeleton was computed for every individual subject based on its smoothed FA map using TBSS/FSL software (Smith et al., 2006). From this skeleton, only the 300 voxels with the highest FA within the given range [0.5–0.9] that were located within the corpus callosum region were chosen. The lower threshold ensured that the mono-directionality of the fibers and voxels with  $FA > 0.9$  were removed because such high values indicate the possibility of being affected by an imaging artifact. In the following, the voxels that are used to compute the kernel response will be called *kernel voxels*.

In order to compare indices across subjects, a common kernel is required. Otherwise, subject specific characteristics might be coded into the kernel and neglected in the comparison. CSD coefficients for the kernel response were computed directly from an axially symmetric diffusion tensor. For this tensor, the principal eigenvalue  $\lambda_1$  was calculated by the average of all  $\lambda_1$  values of all kernel voxels averaged over all subjects. To ensure axial symmetry, the remaining eigenvalues  $\lambda_2$  and  $\lambda_3$  were set to an equal value that was computed by averaging  $\lambda_2$  and  $\lambda_3$  of the kernel voxels. This procedure led to the following configuration:

$$\lambda_1 = 0.0014, \quad \lambda_2 = \lambda_3 = 0.000177 \quad \Rightarrow \quad FA = 0.86, \quad MD = 0.0006$$

The stability of these parameter settings have been tested by assessing FD, FF and FS in different fiber configurations with kernels of higher and lower values of FA and MD. Results are presented in chapter 7.2.

Deviating from the protocol proposed by Tournier (<http://www.brain.org.au/software/mrtrix/tractography/preprocess.html#csd>), CSD was not performed on the diffusion weighted signal but on the signal attenuation, which is required for the interpretation of the derived indices. The signal attenuation was obtained by dividing the diffusion-weighted images by the average b0 image.

### 6.4.2 Indices derived from spherical deconvolution and the diffusion tensor

With CSD, the fODF was computed in every voxel and provides a measure of the fiber density in every direction.

In the current analysis the indices based on Bingham fits to the fODFs were computed with CSD of order 6. With the high angular resolution of the dMRI data an order of up to 8 would be possible. Nevertheless, order 6 was chosen because higher orders increase the number of spurious peaks (Anderson, 2005). This was also shown by Descoteaux and colleagues (2009) on dMRI data with a b-value of 1000 s/mm<sup>2</sup>, and Parker and colleagues (2012) confirmed this finding on synthetic data.

All indices were computed for all subjects in the whole brain using inhouse software as described by Riffert and colleagues (2014). The three largest fiber compartments of each voxel were used; smaller compartments were considered as noise and ignored.

The indices based on Bingham functions were compared with the standard indices derived from the diffusion tensor. The tensor as well as its indices FA, RD and AD were computed using the program *emphdtifit* from the FSL software package.

In order to illustrate the relationship between the indices based on Bingham functions and FA, four different fiber configurations extracted from real data were visualized as fODF glyphs and tensors (Fig. 6.4). The corresponding indices FD, FF, FS and FA were plotted for the two largest peaks. From the shape of the tensor and the corresponding FA values alone it was not possible to distinguish between crossing and fanning fiber configurations. In contrast, the indices derived from the Bingham functions provided detailed information about the existence of minor fiber directions as well as the density and fanning of fibers within each fiber bundle. FD, FF and FS quan-

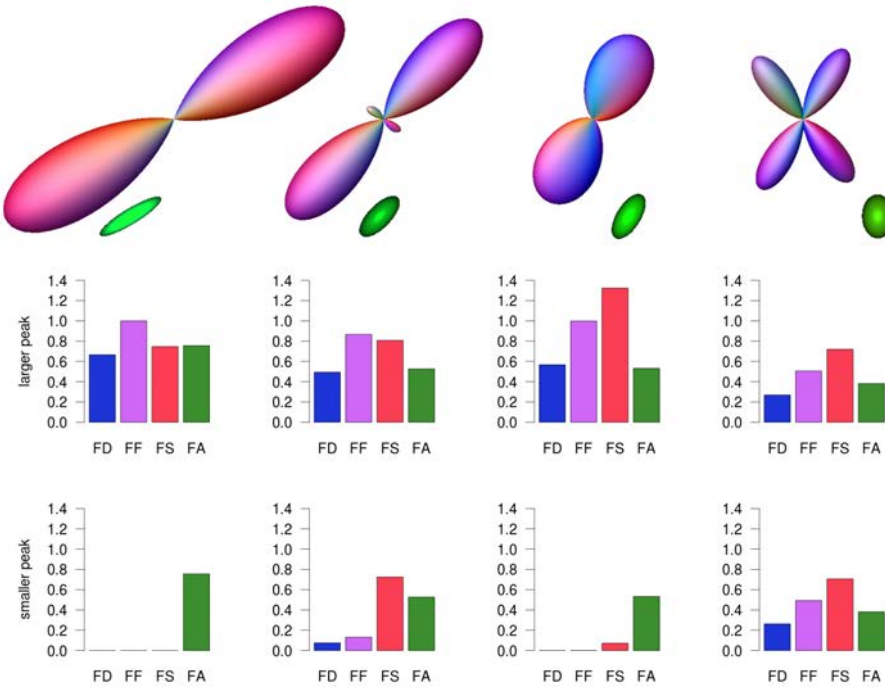


Figure 6.4: Comparing indices of different fiber configurations. The top row shows glyphs (purple) and tensors (green) from different areas in the brain of an arbitrary participant. The second and third rows visualize the indices derived from Bingham fitting for the first and second peak, respectively. To give a comparison, the FA values are visualized in both rows.

tify the different parameters of the fiber bundles analogue to the visual representation as glyphs.

If the real fiber densities in the subjects' kernel voxels were known, it would be possible to multiply this number with the FD value in order to get an estimate of the biological fiber density in a bundle. Alternatively, a standard value of  $3.717 \times 10^5$  fibers per  $\text{mm}^3$  as published by Aboitiz and colleagues (1992) could be used as approximation. As the absolute density of fibers is not known in this study and is difficult to estimate due to missing information for children, FD is expressed relative to the FD in the kernel voxels.

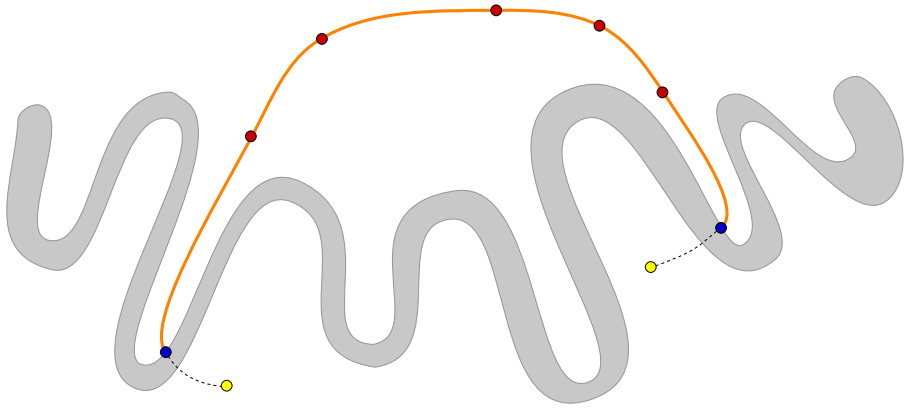


Figure 6.5: Modeling the connecting pathway using Catmull-Rom splines. Three different types of control points define a pathway: the fixed end locations (blue), the control points on the path (red) and the two outer control points that define the direction (yellow) at the fixed locations.

## 6.5 Plausibility Tracking

### 6.5.1 Introduction

The purpose of Plausibility Tracking is to model the path of a fiber track between two defined endpoints in the form of a parametrized curve. The endpoints are fixed but the curve is optimized for describing the most plausible path through the brain. Possible axonal pathways were modeled with Catmull-Rom splines (Catmull and Rom, 1974). These are cubic splines that are parametrized solely by the location of control points, and hence are fast and easy to optimize.

The control points can be divided into three different categories as visualized in Fig. 6.5. The first type comprises the two fixed locations on the gray-white matter interface, whose connecting path is to be determined. Their position will not change in the following optimization process. The second category comprises the control points along the track. Their positions and numbers are flexible. A higher number of control points allows for a more accurate modeling of the path, but also bears the risk of overfitting and increases processing time. Finally, there is a pair of two extra control points outside the curve that are required for defining the direction of the curve at the fixed locations.

## 6.5.2 Initialization

The speed and quality of finding the optimal parameters for the spline curve greatly depends on initialization. In the presented workflow probabilistic tractography was used to get an estimate of the connecting pathway and to obtain the initial parameters by computing an average track. Deterministic streamline tractography was not suitable for this initialization because it followed only the most probable path and is not able to follow e.g. all transcallosal connections. Probabilistic tractography as described above determines the probability of two regions being connected, and also finds connections that do not follow the major fiber bundles (Yo et al., 2009). By definition, the tracks obtained from probabilistic tractography are jagged, and a single track does not necessarily reflect a possible axonal pathway. However, when taking into account multiple tracks that pass through two regions of interest, the majority of them follow approximately the anatomically expected pathway.

Probabilistic tractography based on CSD was performed using the MRtrix software package (Tournier et al., 2012). In order to retrieve a set of probabilistic tracks that describe the connection of two locations in the brain, only tracks were selected that passed through both connection points within a defined radius  $r$  of 2.5 mm. At least 11 tracts<sup>1</sup> had to connect two points in order to render a connection significant. To compute the control points of a spline that describes the average of the  $N$  selected tracks  $T = \{t_1, t_2, \dots, t_N\}$ , a two-stage procedure was followed. First, each probabilistic track  $t_i \in T$  was parametrized along its arc length to define a fixed number  $M$  of regularly distributed track points  $P_i = \{p_{i1}, p_{i2}, \dots, p_{iM}\}$ . Second, the coordinates of the spline control points  $C = \{c_1, c_2, \dots, c_M\}$  were computed by taking the medians of all corresponding track points. The fixed locations that were the endpoints of the curve defined additional control points  $c_0$  and  $c_{M+1}$ , which were not modified during the optimization process. Catmull-Rom splines are cubic splines that are described by the control points along their path plus two extra control points  $c_{-1}$  and  $c_{M+2}$  that define the direction at the fixed connection points  $c_0$  and  $c_{M+1}$ . These two extra control points were initially set in the linear extrapolation of the fixed connection points and

---

<sup>1</sup>This number showed a reasonable results for the previously defined number of probabilistic tracks and the radius. Similar to the problem of thresholding maps from probabilistic tractography, there is no algorithm for computing the value from the data.

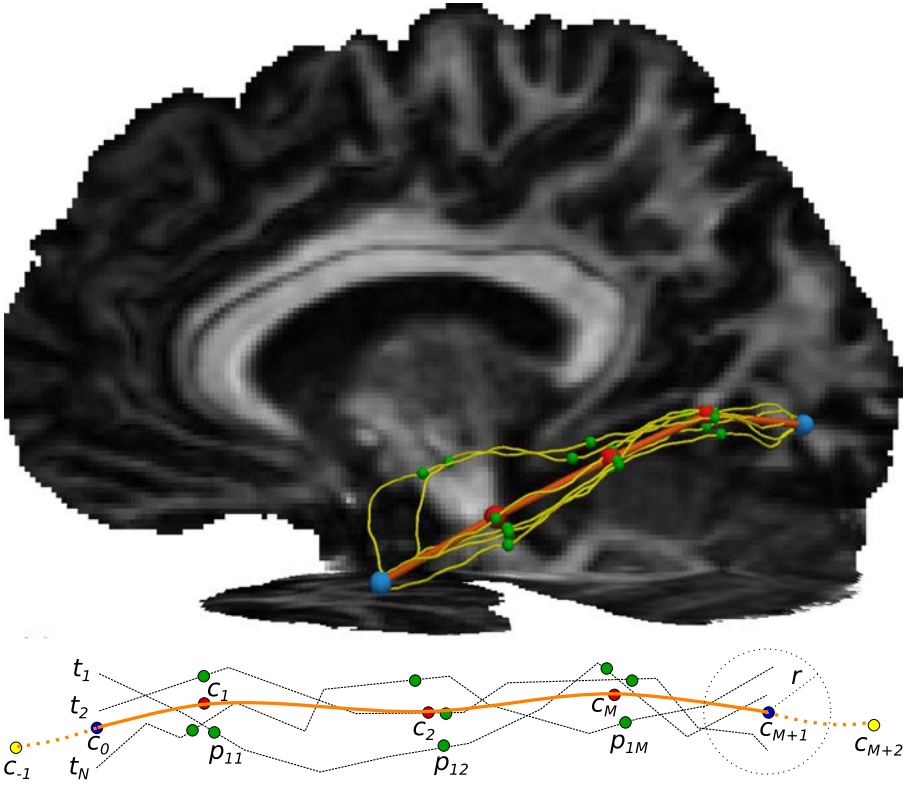


Figure 6.6: Initialization based on probabilistic tractography. The method is visualized with real data (top) and as a schematic drawing (bottom). Control points  $c$  for the Catmull-Rom splines are computed in a multi-stage procedure. Tracks  $t$  are parametrized along their arc length to obtain track points  $p$  (green). The coordinates of corresponding track points  $p$  are then averaged to obtain spline control points  $c$  (red). Additional spline control points outside the track ( $c_{-1}$  and  $c_{M+2}$  (yellow)) are placed in the linear prolongation of the endpoints  $c_0$  and  $c_{M+1}$  (blue).

their neighboring control points. The computation of the fixed control points based on probabilistic tractography is visualized in Fig. 6.6.

### 6.5.3 Optimization

After initialization the spline parameters were optimized. This process consisted of two major components: the metric to evaluate the quality of the current parameter set, and the algorithm that chooses the next parameter set.

The metric in this method computed the current optimization value based on measurements from CSD. Spherical deconvolution has been chosen because the local fODF values are, in theory, proportional to the density of axonal fibers with respect to the current local direction. Assuming that fibers are organized in bundles, the plausibility of a given local direction depends on the alignment with the bundle's direction and the spread of fibers within the bundle.

Instead of using the absolute fODF amplitude  $fODF(\vec{u})$  in the current direction  $\vec{u}$  its value relative to its closest peak's  $p(\vec{u})$  amplitude  $fODF(p(\vec{u}))$  has been computed. This provided a measure of probability within the fiber bundle which is called "local plausibility"  $\chi(\vec{u})$  and can be written as

$$\chi(\vec{u}) = \frac{fODF(\vec{u})}{fODF(p(\vec{u}))}. \quad (6.1)$$

The idea of the local plausibility  $\chi(\vec{u})$  is supported by Fig. 6.7. As  $fODF(\vec{u})$  is by definition always smaller than or equal to the corresponding  $fODF(p(\vec{u}))$ , the local plausibility  $\chi(\vec{u})$  ranged between 0 and 1. The maximal value was reached if the curve's local direction was perfectly aligned with one of the model's peak directions  $p(\vec{u})$ . Any deviation from the closest peak's direction lead to smaller values, depending on the distribution of fiber directions modeled in the peaks. In peaks that represented strongly aligned fiber bundles and hence showed a low spread, small directional deviations lead to strong decreases in the obtained value. Vice versa,  $\chi(\vec{u})$  decreased only moderately if the distribution of fiber directions was widespread and the glyphs had broad lobes. Even in peaks where the model was not able to distinguish two separate directions, reasonable values were obtained because  $\chi(\vec{u})$  can be close to 1 even if the angle to the closest peak is relatively large (see Fig. 6.7). The fact that  $fODF(\vec{u})$  became 1 if  $\vec{u}$  is perfectly aligned with *any* of the model's peak directions is coherent with the assumption that the plausibility of a fiber direction can also be maximal in minor fiber bundles.

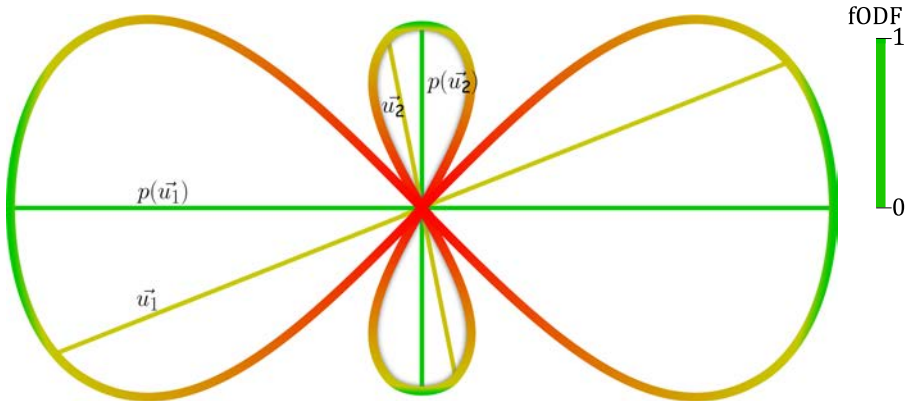


Figure 6.7: Schematic drawing of a glyph with two peaks. The local plausibility value is computed as the ratio of the fODF values of the local fiber direction  $\vec{u}$  (yellow) and its corresponding peak direction  $p(\vec{u})$  (green). The wider the peak, the slower the plausibility value decreases with deviation from the peak direction.

In this context there is a difference between probability and plausibility: The probability of a track is high if it follows a pathway that potentially many fibers share. The plausibility of a track is characterized by a maximal accordance with local fiber directions. It is therefore proportional to the probability of the track orientation under the condition that the track belongs to a particular bundle (which can also be a minor one). Even in a highly unbalanced crossing it is considered more plausible that a track is well aligned with a less dominant fiber bundle than being only moderately well aligned with a major fiber bundle.

Smith and colleagues (2012) also use the term *plausibility* for *spherical-deconvolution informed filtering of tractograms (SIFT)*. This method removes previously generated streamlines from whole brain tractography in a way that the accumulated streamline length passing a voxel in each direction corresponds with the fiber densities of the local model. There are 2 major differences compared to Plausibility Tracking. First, SIFT is a post-processing method that filters already generated tractograms while Plausibility Tracking creates connecting pathways. Second, SIFT ensures that the accumulated streamline length within a voxel correlates with the fiber densities of the local model which requires whole brain tractography while Plausibility Tracking can be used to model the pathway of distinct connections in the brain.



The global plausibility  $X$  of a pathway was then computed as the average of all local plausibility values  $X_i(\vec{u})$ . As the initial parameters of the splines were already expected to be close to optimum, a downhill optimization procedure could be used. Unfortunately, gradient information was not available to guide the optimizer because  $\chi(\vec{u})$  was not always continuous. Therefore, a downhill simplex optimization procedure (Nelder and Mead, 1965) that does not require gradients was applied.

An optimization solely based on the global plausibility  $X$  was not practical for two reasons. First, in some configurations the path produced sharp bends. This was handled by adding a term  $\Gamma$  that penalized excessive curvature of the path.  $\Gamma$  was defined as

$$\Gamma = \begin{cases} 1, & \text{if } \max(\alpha_i(d)) < \frac{\pi}{4} \\ \exp\left(-\frac{1}{2\sigma^2} \left(\max(\alpha_i(d)) - \frac{\pi}{4}\right)^2\right), & \text{if } \max(\alpha_i(d)) \geq \frac{\pi}{4} \end{cases} \quad (6.2)$$

where  $\alpha_i(d)$  is the angle between the tangents of two points on the curve with distance  $d$  (set to 5 mm) from the  $i$ -th of  $n$  points of the spline path and  $\sigma$  was set to  $\pi/4$  and weighted the influence of  $\Gamma$ . This penalized bends if the angle between the two tangents became smaller than  $\pi/4$ . The Gaussian shape of the penalty function ensured a mild penalty for marginal undercuts of the given angle, but pushed  $\Gamma$  close to 0 if the angle became much smaller. A direct conversion to the radius of curvature as used in streamline tractography is not possible.

Another constraint for the optimizer was set for the distribution of control points. Control points that were very closely spaced caused looping artifacts. In order to ensure a relatively homogenous distribution of control points another term  $E$  had been added that constrained the minimum distance of two control points. It was defined as

$$E = 1 - \exp\left(-\frac{1}{2\sigma^2} \left(\frac{\min(D)}{\text{average}(D)}\right)^2\right) \quad (6.3)$$

where  $D$  is a set of distances between neighboring control points and  $\sigma$  was set to 0.2. Again, the Gaussian shape of this penalty function put a mild penalty on small irregularities in the distribution of control points, but pushed  $E$  close to 0 for a strong inhomogeneity in the distribution.

In some cases additional constraints in form of waypoint masks were required to ensure that the pathway followed a distinct route. Waypoint masks were implemented

as image files that have a value of 1.0 for voxels within the mask and lower values for voxels outside the mask, decreasing with increasing distance to the mask. For each mask, the maximum voxel value passed by a track was stored and the minimum of these values for all way-point masks was considered as the closeness  $C$  to the waypoint masks. A value of  $C = 1.0$  indicated that all waypoint masks were crossed by the track.

Furthermore, the pathway was not allowed to leave the white matter area. However, just disqualifying the path as invalid when it leaves white matter did not provide the optimizer with any information in which direction to search for better parameter settings. Therefore, a modified plausibility measure  $\chi^*(\vec{u})$  that took the white matter area and optional waypoint masks into account was defined as

$$\chi^*(\vec{u}) = \begin{cases} \chi(\vec{u}), & \text{if } \vec{u} \text{ is in white matter and } C=1 \\ -\beta(1 - (p_{wm}(\vec{u}) \times C)), & \text{if } \vec{u} \text{ is not in white matter and/or } C < 1 \end{cases} \quad (6.4)$$

where  $p_{wm}(\vec{u})$  is the probability of  $\vec{u}$  being in white matter and  $\beta$  is a weighting factor that was set to 10.  $C$  is the closeness to the waypoint masks that was by default set to 1.0 if no waypoint masks were specified. The decision whether  $\vec{u}$  was in white matter or not was based on a thresholded map of white matter probability (see chapter 6.3). In this way the number of points outside the white matter area and the distance to the gray-white matter boundary as well as the distance to the waypoint masks were taken into account.

The optimization value  $\Omega$  for the path was then computed as

$$\Omega = -X^* \Gamma E. \quad (6.5)$$

A number of parameters had to be chosen for the described algorithm. The values specified have been evaluated empirically when testing the algorithm on phantom data and different fiber pathways in the human brain. As it turned out, the used values for the parameters of curvature, control point distribution and white matter probability were applicable for a wide range of fiber pathways. They provided a good compromise for straight and curved pathways and prevented loops as well as very sharp bends. In contrast, however, the search radius and the number of required probabilistic streamlines for the initialization as well as the number of control points depended very much on the

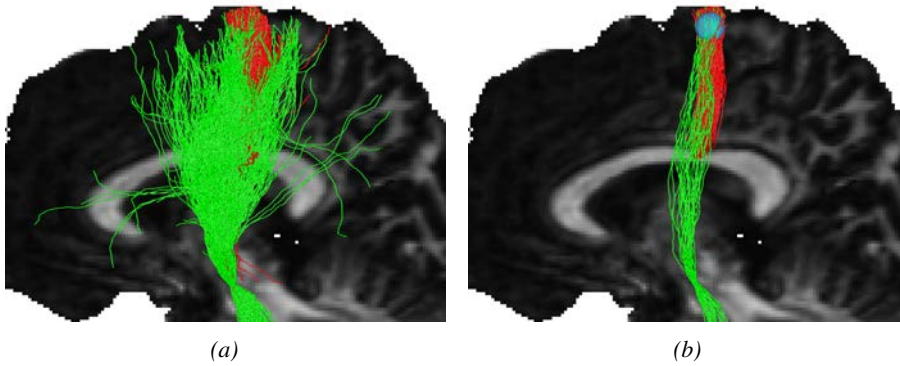


Figure 6.8: Parameters for minimum number of probabilistic streamlines and search radius. 500 streamlines were seeded in the corpus callosum (red) and the same number in the ventral part of the corticospinal tract (green). Most tracks from the corpus callosum were captured by the sphere while the tracks from the corticospinal tract were fanning out to a larger region so that less crossed the sphere.

pathway of interest. The number of required probabilistic streamlines also depended on the desired confidence that a connection was considered as real and on the number of streamlines actually expected in each region of interest. The latter is similar to the unsolved problem at which value to threshold maps of probabilistic tractography. Visual inspection revealed that a minimum of 11 probabilistic streamlines was a good value for the given setup. The estimation of the minimum number of probabilistic tracks and the size of the search radius is visualized in Fig. 6.8. 500 streamlines were seeded in the corpus callosum (red) and the same number in the ventral part of the corticospinal tract (green) as shown in Fig. 6.8a. Most tracks from the corpus callosum were captured by a sphere of radius  $r=5.0$  mm while the tracks from the corticospinal tract were fanning out to a larger region so that less crossed the sphere (Fig. 6.8b). Accordingly, a smaller search radius and/ or larger number of minimally required streamlines can be used for coherent fiber bundles while a smaller number of minimally required streamlines might be required if the streamlines are proceeding to different or larger areas in the brain. Finally, a reasonable number for the minimum number of required streamlines also depends on the number of generated streamlines. The search radius ensured that streamlines which passed close by the defined coordinate could be considered for the connection. The larger the radius, the larger the number of required probabilistic

streamlines should be. The number of control points depended on the complexity of the shape of the fiber pathway, which was difficult to assess in advance. For specific fiber pathways, the number of control points could be assessed empirically. This can be seen in chapter 7.4.1, where several different fiber bundles have been reconstructed with the described parameter values and the number of control points being the only parameter that had been adapted. When testing the plausibility of connection between a fixed location and various distributed other locations, it was useful estimating the number of control points from the length of the initial track by placing control points every 15 mm or 20 mm (as done in chapter 7.3.2).

## 6.6 Applications

### 6.6.1 Reconstruction of distinct fiber pathways

Plausibility Tracking can be used for reconstruction of the connecting fiber pathway between two regions of interest. These regions can be obtained from various sources. Someone familiar with the human anatomy might draw the ROIs into the individual data sets based on anatomical prior knowledge. This method was applied to one single subject in order to reconstruct parts of the left corticospinal tract, the arcuate and uncinate fasciculus as well as the cingulum. Depending on the fiber bundle of interest, the ROIs can have very different shapes and volumes. For example, the cortical area was defined as the voxels at the dorsomedial ends of the white matter covering a lengthy area. The fixed locations for the arcuate fasciculus are located on sagittal planes through Broca's and Wernicke's areas. All other ROIs were defined with a compact shape in the terminal regions of the respective fiber bundles.

Further possible methods would be to align an atlas with pre-defined regions with the individual subject or to apply (semi-)automatic segmentation methods which would reduce the user's subjective influence.

The only parameter in Plausibility Tracking that was adopted to account for the different shapes of the fiber bundles was the number of control points. Stronger curved pathways obviously required more control points in order to reconstruct the fiber bundles accurately. All other parameter values described above proved to be stable for all four fiber bundles, despite their different shapes.

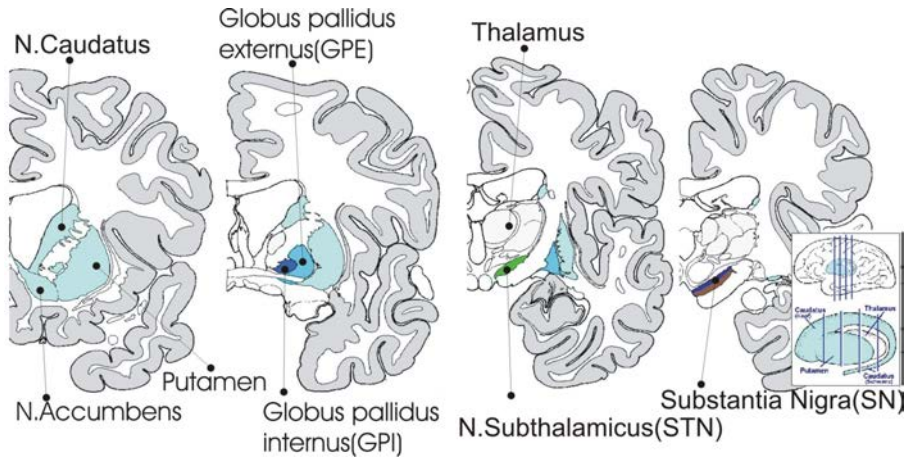


Figure 6.9: Anatomy of basal ganglia. Schematic drawings of successive coronal sections through the basal ganglia show the location of putamen, globus pallidus and substantia nigra. (from: [commons.wikimedia.org/wiki/File:Anatomie-Basalganglien-A.jpg](https://commons.wikimedia.org/wiki/File:Anatomie-Basalganglien-A.jpg))

### 6.6.2 Connections through minor pathways

Modeling minor fiber pathways requires careful initialization as the majority of probabilistic streamlines tend to follow the dominant pathways represented by the major directions of the local model. In order to limit the probabilistic tracks to the pathway of interest, waypoint masks might be necessary to guide the initial probabilistic tractography and/ or Plausibility Tracking. These masks can either be defined on a common template and registered to the individual anatomy or, alternatively, the masks can be drawn on every individual data set.

In this project<sup>2</sup> the connections between substantia nigra and putamen, which traverse the globus pallidus, are modeled (see Fig. 6.9). Tracking this connection is expected to be difficult for two reasons: a) The dMRI data in this areas show a low signal to noise ratio caused by the high concentration of iron in the globus pallidus. b) Due to the dominance of fibers in the external medullary lamina of the globus pallidus, only a fraction of the initialized probabilistic tracks find their way from the globus

<sup>2</sup>This is a cooperation project with Andreas Hintzen and Marc Tittgemeyer from the *Max Planck Institute for Neurological Research*, research group "Cortical Networks". All dMRI data and masks were provided by the cooperation partners.

pallidus into the putamen (4.6 %). Most of the probabilistic streamlines are deflected in the external medullary lamina of the globus pallidus and do not continue to spread within the globus pallidus into the putamen as described by Cossette and colleagues (1999). Therefore, waypoint masks for the initialization through probabilistic tractography and for Plausibility Tracking have been defined. Areas of substantia nigra and the putamen as well as waypoint masks covering the dorsal surface of the substantia nigra and the medial surface of the putamen were drawn on an MNI template and registered to the b0 images of the subjects.

Data were acquired using the following protocol: acquisition on a Siemens 3T Trio scanner with a double spin echo diffusion weighted EPI sequence, GRAPPA acceleration factor 2 and 1.7 mm isotropic voxel size, 60 diffusion directions with a b-value of 1000 s/mm<sup>2</sup> and 6 images without diffusion weighting (b0 images).

Diffusion weighted data were interpolated to 1.0 mm isotropic voxel size. Regions of substantia nigra and the putamen as well as the waypoint masks were defined on a template with the same resolution. The kernel voxels were obtained for every subject individually as described in chapter 6.4. MRtrix (Tournier et al., 2012) was used for constrained spherical deconvolution (order=6) and probabilistic tractography. The latter was performed with the default parameters except for the step size (-step 0.9), number of desired tracks (-number 10 000), maximum track length (-length 60) and the number of trials (-trials 50).

### 6.6.3 Mapping indices onto individual fiber bundles

Having a local direction in every voxel along the connecting pathway makes it possible to analyze not only directionally invariant but also direction dependent indices. In order to compare locally corresponding quantities across subjects, two steps are necessary. First, the pathway of every subject has to be parametrized or segmented in a reproducible and comparable manner. Second, the indices have to be accumulated within their segments for statistical evaluation.

In the method presented here, the parameterization is performed with an extended version of Corouge's approach (Corouge et al., 2006). While these authors specify common start and endpoints by the intersection of the fiber tracts with two planes, multiple intersecting planes (as suggested by Corouge) along the pathway are defined here.

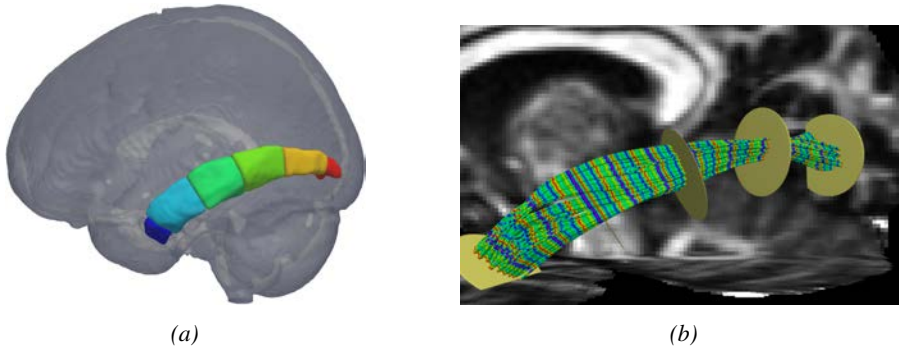


Figure 6.10: Atlas and tracks of the left inferior longitudinal fasciculus of a single subject. *a)* The outer sections (blue and red) of an atlas define the areas for the fixed locations of the tracks (temporal pole and medial occipital lobe), while sampling of indices takes place only in the four central sections. *b)* Yellow disks represent the planes between the sections. The colored stripes on the track indicate corresponding samples that are summarized perpendicular to the pathway's main direction.

It is also ensured that every section in all individuals has the same number of evenly spaced samples. This procedure generates the same number of samples in every track in all subjects and ensures perpendicular correspondence of samples even along curved pathways. The planes are computed for every subject individually, guided by a purpose-built white matter volume atlas (see Fig. 6.10a) that is aligned<sup>3</sup> with each subject's anatomy. This atlas can be generated in any suitable way, depending on the available information. Here, it is constructed semi-automatically by manually defining seed and inclusion regions to extract the pathway from probabilistic tractography in all subjects. The individual tracks are sampled to voxel maps, transformed to standard space and averaged. Thresholding and dilating the averaged track map resulted in a binary mask of the pathway. This mask was then divided manually into roughly equidistant sections. The sections were aligned with interesting features of the tracts, such as crossing areas. Finally the intersection planes for tract parametrization (Fig. 6.10b) were fitted to the boundaries between the sections using a support vector machine algorithm (Joachims,

<sup>3</sup>The registration task is performed with the Advanced Normalization Tools (ANTS <http://www.picssl.upenn.edu/ANTS/>) (Avants et al., 2008; Avants et al., 2011) that showed high class results in a comparison of different non-linear registration methods for atlas mapping (Klein et al., 2009). The FA map that corresponds to the atlas and the individual FA maps serve as basis for the registration as they are located natively in the diffusion space.

1999). These planes support a reproducible and comparable parametrization of the pathway across subjects.

Similar to Colby and colleagues (2012), the values of indices along the pathway are sampled for every spline curve at a rate of 20 samples per atlas section (distance between successive points about 1 mm), thus dividing each section into 20 segments. As a consequence, voxel values from the index maps are potentially considered several times in the accumulation. This approach effectively causes a weighting of the index values: voxels that are passed more often by the modeled fiber tracks than others are considered to be more representative of the current connection and privileged accordingly.

There are three different types of indices that can be evaluated. In the simplest case, these are rotationally invariant and bundle-independent values (e.g. FA) that are sensitive to microstructural properties of the underlying tissue in every voxel. The second type comprises compartmental (i.e., one value per bundle) indices like FD, FS and FF. The third category of indices that can be evaluated with the presented method contains functions of the direction, like the amplitude of the fODF or the local plausibility as used for the plausibility tracking (see above).

### 6.6.4 Comparing indices between groups

After thorough validation of Plausibility Tracking the complete workflow was applied to two different fiber bundles. First, in order to demonstrate the explanatory power of the direction dependent indices, they were mapped onto an inter-hemispheric pathway connecting the left and right Brodmann Area 45 (Brodmann, 1909). Second, as in the example of the left *inferior longitudinal fasciculus* (ILF), it is shown how differences between groups of subjects can be interpreted more specifically than with the widely used tensor derived indices.

As shown in Fig. 6.10b, the corresponding samples from all tracks of a subject form segments across the pathway. The measurement values at the sample locations are summarized by calculating the median for every segment. Consequently, for every index, the medians per segment and subject are calculated. As these median values are not necessarily normally distributed across subjects, a non-parametric permutation test (Nichols and Holmes, 2002) that implicitly accounts for multiple comparisons was



chosen. After writing the median values to an image file, the *randomise* tool implemented in the FSL software package (Smith et al., 2004; Woolrich et al., 2009) that performs the non-parametric randomization test was used. In addition, post-processing by Threshold-Free-Cluster-Enhancement as described by Smith and colleagues (2009) was performed. Significance was defined for  $p < 0.05$ , resulting from two one-sided tests (as there is no a priori knowledge on the sign of the difference) at  $p < 0.025$  and subsequent Bonferroni correction.

## 7 | Results

### 7.1 Overview

The validity of the parameters to compute the fODF by constrained spherical deconvolution are verified in section 7.2. The local model builds the basis for Plausibility Tracking and has an influence on the tracking results. The influence of the deconvolution kernel on the indices that describe the white matter's microstructure is described in the same section.

In section 7.3, the correct function and general behavior of Plausibility Tracking is demonstrated on data set of a phantom and a human brain. The phantom had been built for comparison of the performance of different tractography methods. The pathway of the artificial fibers is exactly known so that the modeled pathways can easily be compared with the ground truth. On the human data, Plausibility Tracking is compared with results of deterministic and probabilistic tractography. This visualizes the differences and commonalities of the methods and reveals new potentials to characterize the human connectome.

The applications in section 7.4 demonstrate the feasibility of Plausibility Tracking for reconstructing distinct major fiber bundles and track them along minor pathways. Finally, the framework is completed by mapping of indices onto individual fiber bundles and comparison of these between groups.

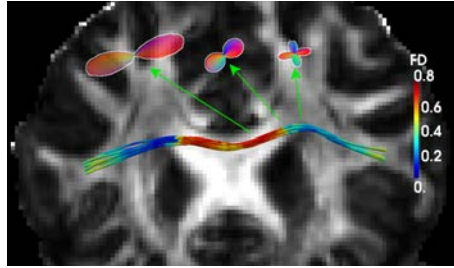


Figure 7.1: Glyphs showing different fiber configurations along a connection between left and right BA45. Fibers are running parallel within the corpus callosum and show a fanning configuration in the transition to the intersection with the corona radiata where the model shows a crossing configuration.

## 7.2 Local modeling

In order to validate the stability of the parameters of the deconvolution kernel described in chapter 6.4, voxels with known fiber configuration were extracted from a single subject and their signal attenuation was deconvolved with different kernels. A voxel with parallel fibers was extracted from the *corpus callosum* (CC), two with fanning fibers from the transition of the CC to the crossing with the *superior longitudinal fasciculus* (SLF) as well as from the *corona radiata* (CR). One voxel with a crossing configuration was extracted from the intersection of CC and SLF. An anatomical reference for these voxels (except for the first fanning configuration extracted from the CR) is provided by Fig. 7.1.

The major parameters modifying a tensor are its shape (described by the FA) and size (described by the MD). Fig. 7.2a shows the glyphs of the selected voxels with constant MD (0.0006) and varying FA ranging between 0.75 and 0.95, while Fig. 7.2b shows the glyphs computed with constant FA (0.85) and different values of MD ranging between 0.0004 and 0.0008.

At first glance, the differences are quite subtle. A close look, however, at the first fanning voxel reveals that higher values of FA and MD increase the tendency for false crossings. An important aspect of this observation is if CSD derived indices that are used for the quantification are able to describe the fiber configuration adequately. In theory, for the dominant bundle, FD should be constant in all configurations while

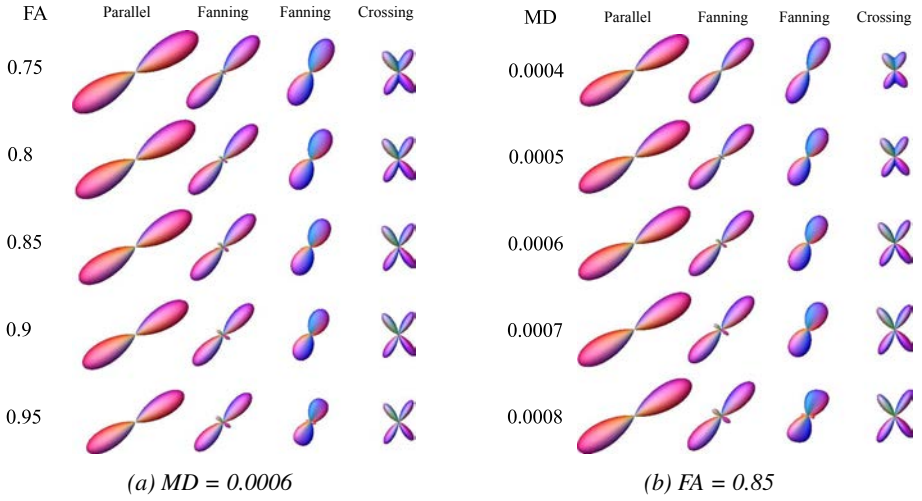


Figure 7.2: Glyphs of voxels with parallel fibers,  $2\times$  fanning and crossing fiber configurations computed with different deconvolution kernels. (a) MD of the deconvolution kernel is kept constant while FA ranges between 0.75 and 0.95. (b) FA of the deconvolution kernel is kept constant while MD ranges between 0.0004 and 0.0008

FF should always be 1 in the parallel and fanning fiber cases and 0.5 for the crossing configuration (assuming an equal crossing of two fiber populations). FS is expected to be higher in fanning areas than for a parallel fiber configuration. Fig. 7.3 shows the graphs of FD, FF and FS with varying FA and MD.

FF seems to be quite unaffected by different values of FA and MD in the parallel and crossing configuration but decreases with increasing FA and MD in the fanning areas. Hence, if the kernel is chosen too sharp or too large, the fODF tends to show crossing configurations in fanning areas.

FS increases in the fanning areas with increasing FA and MD, so that a higher FA and MD values seem desirable while the parallel and crossing configuration show only small variations.

FD is approximately constant in all configurations but should be 1.0 where only one fiber population exists. This theoretical value was not met, mainly due to limitations in the spherical harmonic approximation (see Riffert et. al 2014). The fODF in the corpus callosum should be close to a Dirac function. Truncated spherical harmonics expan-

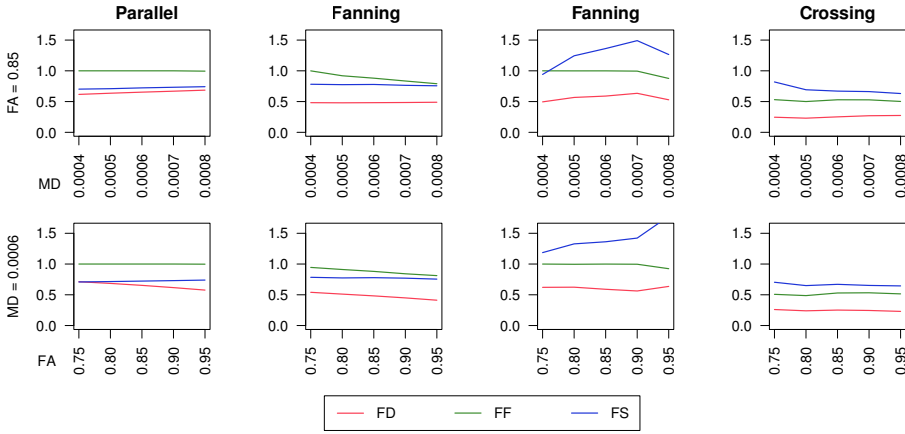


Figure 7.3: FD, FF and FS in parallel,  $2\times$  fanning and crossing fiber configurations computed from CSD with different response kernels. The upper row shows results with deconvolution kernels of constant FA and varying MD while the bottom row shows results with constant MD and different values for FA.

sion are not suitable for describing such sharp functions. Despite the deviation from the theoretical value due to limitations of the spherical harmonic approximation (see section 8.3 in the chapter Discussion), FD has shown to be a valuable marker (Riffert et al., 2014).

The parameters chosen to compute the deconvolution kernel seem to adequately and reliably describe the fiber configuration.

## 7.3 Plausibility Tracking

### 7.3.1 Validation with data of a phantom

When introducing a new method of tractography, one way to evaluate its performance is to apply it to data of a realistic phantom with known fiber pathways. Accordingly, Plausibility Tracking was applied to the phantom of the FiberCup (Poupon et al., 2008; Fillard et al., 2011) (<http://www.lnao.fr/spip.php?rubrique79>). This phantom shows various fiber configurations from parallel and bending to crossing and touching. The ground truth of fiber pathways for this phantom are depicted in Fig. 7.4a.

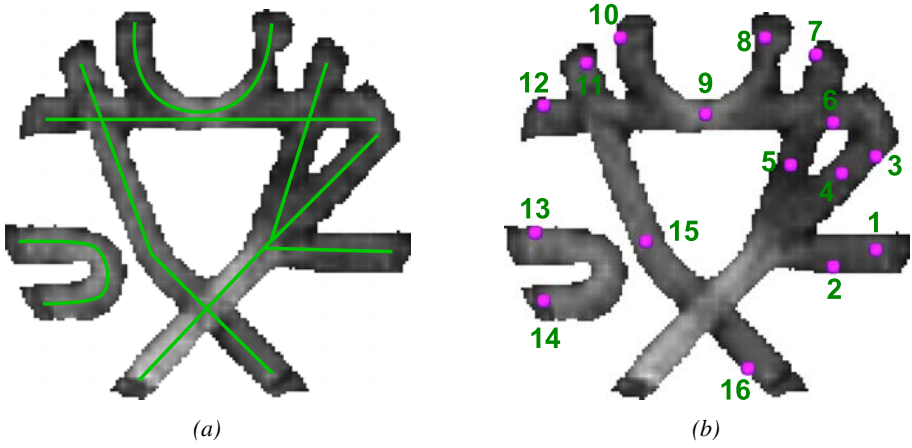


Figure 7.4: Phantom of the FiberCup. a) The green lines indicate the directions in which the synthetic fibers are arranged in the phantom. b) The locations of the spatial positions are marked in purple.

For the evaluation of Plausibility Tracking, the data with a b-value of  $1500 \text{ s/mm}^2$  and a resolution of  $3 \text{ mm}^3$  were used and interpolated to  $1 \text{ mm}^3$ . The deconvolution was performed with 6<sup>th</sup> order, and the kernel is defined by a tensor with the following parameters:

$$\lambda_1 = 0.00184192, \quad \lambda_2 = \lambda_3 = 0.00111604 \quad \Rightarrow \quad FA = 0.2993, \quad MD = 0.001358$$

These parameters were computed from the 37 voxels with highest FA. They differ significantly from those of human white matter because the diffusive properties of the plastic fibers used for the phantom are different from those of axons in the human brain.

In contrast to streamline tractography methods it is not possible to start Plausibility Tracking in a single voxel and see where the track ends. Hence, Plausibility Tracking was started in the spatial locations suggested by the FiberCup (see Fig. 7.4b). All voxels at the borders of the phantom were considered as possible connection points. Consequently, there are multiple tracks originating from every spatial location that may be rated according to their individual plausibility value (Fig. 7.5 and Fig. 7.6).

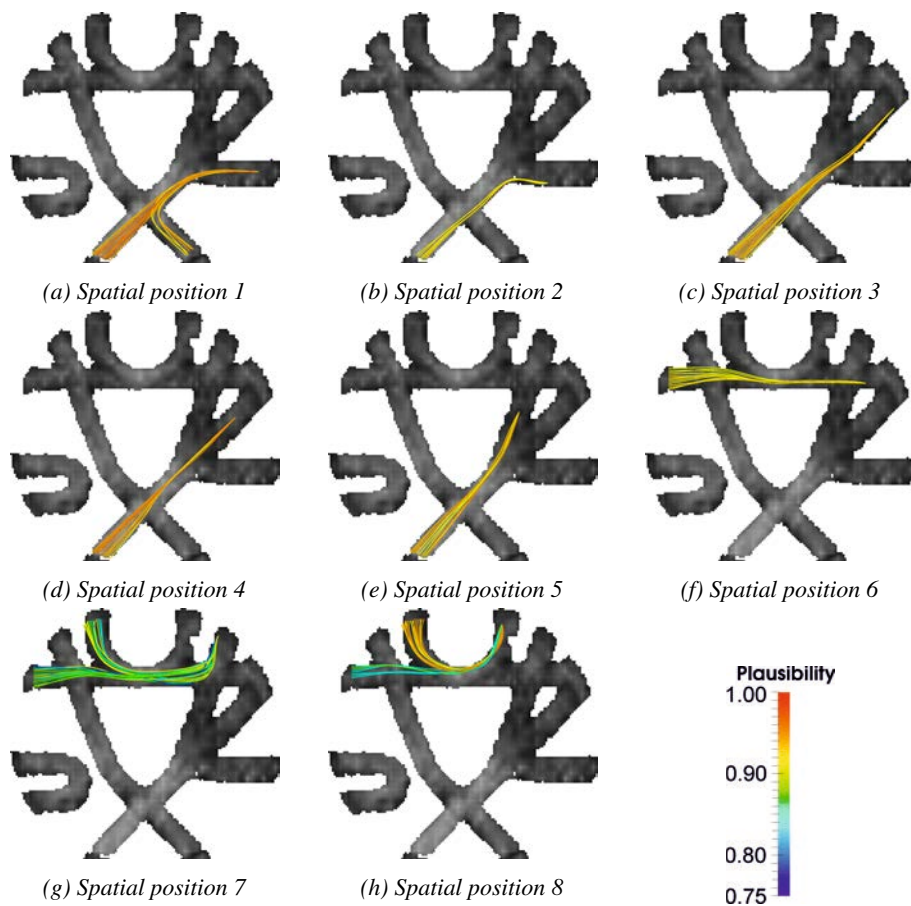


Figure 7.5: Plausibility Tracking applied to phantom data of the FiberCup. Here, tracks that connect the spatial locations 1–8 are shown.

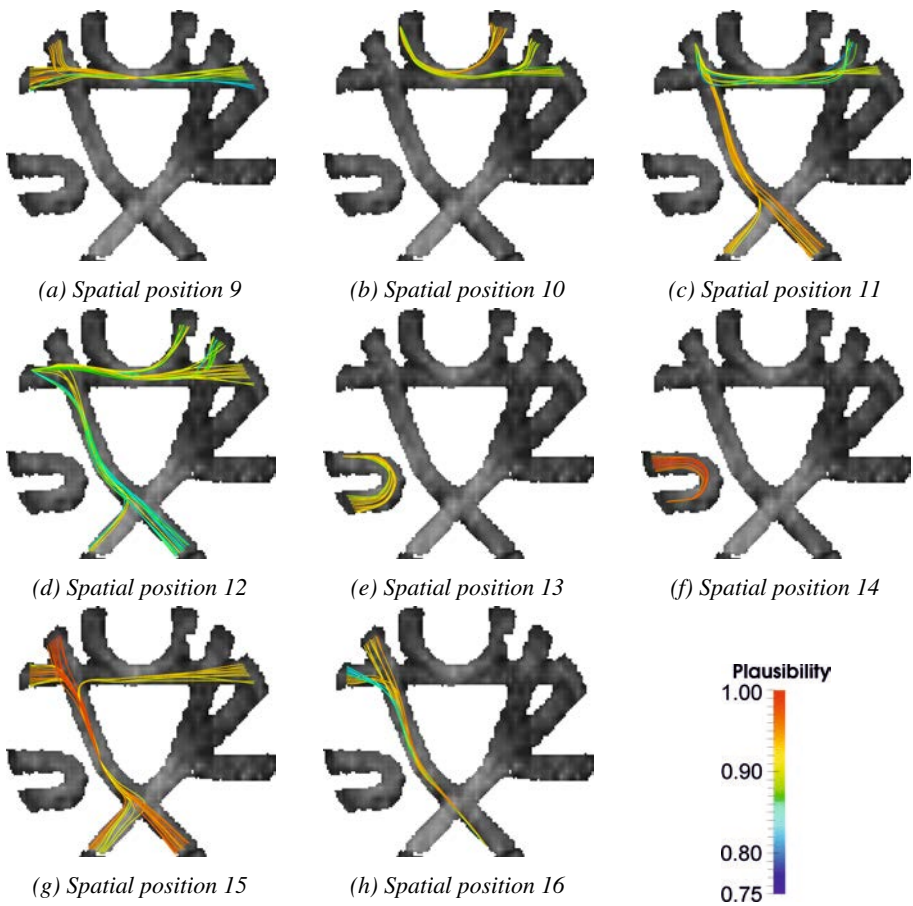
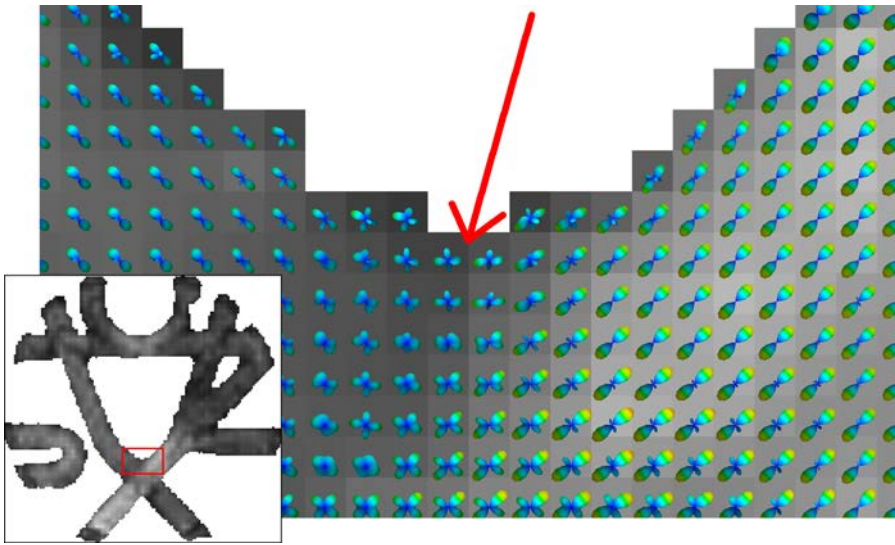


Figure 7.6: Plausibility Tracking applied to phantom data of the FiberCup. Here, tracks that connect the spatial locations 9–16 are shown.





*Figure 7.7: Close up on the fODF glyphs in the lower crossing region (red rectangle). Not all glyphs follow the strict orthogonal directions of the fiber configuration (red arrow).*

Comparison of results with Fig. 7.4a reveals that pathways also gained relatively high plausibility values if they did not follow the expected path. This effect may have multiple reasons. On the one hand, the global nature of Plausibility Tracking permitted local inaccuracies and hence tolerated suboptimal alignment with the local model in some regions. On the other hand, the tilt of the fODFs in crossing regions (as described e.g. by Riffert et al., 2014) sometimes even supported these bendings as shown in Fig. 7.7. Despite these considerations, the results are very convincing which becomes most obvious when looking at Fig. 7.8 showing only the most plausible track for every given spatial location.

Except in case of spatial position 7, which is marked in red (Fig. 7.8), all of the most plausible tracks follow the expected pathway closely. The reason for failure in spatial position 7 was that not enough probabilistic streamlines from the initialization reached the expected border voxels. The inability of probabilistic tractography to adequately represent this pathway has also been shown in the supplementary material of the FiberCup publication (Fillard et al., 2011) and is visualized in Fig. 7.9b. In contrast to the method presented here, Fillard and colleagues used a different method

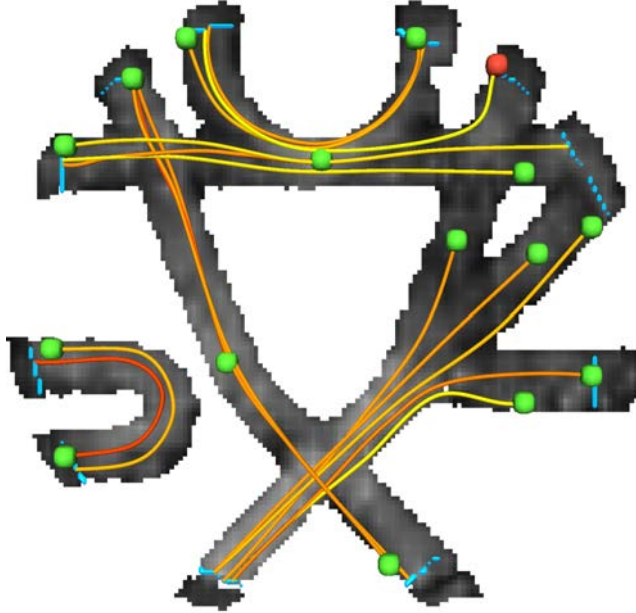


Figure 7.8: Most plausible pathway for each spatial location (green and red). All tracks except for spatial location 7 (red) follow the expected pathway. The potential target voxels at the phantom's border are marked in light blue.

of probabilistic tractography (*bedpostx* from the FSL software package), which is based on the ball-and-sticks local model (see section 5.4.3). Obviously, the fibers passing through spatial position 7 seem to be difficult to follow with different methods of probabilistic tractography. In the contest of the FiberCup only 2 out of 10 methods were able to reconstruct the expected pathway.

A quantitative comparison of the methods which participated in the FiberCup is not possible because the most plausible tracks from Plausibility Tracking connected only into one direction so that the tracks were generally shorter than the FiberCup's software for rating the results expects. Consequently, the scoring would have been reduced. However, the results from Plausibility Tracking are visually extremely similar compared to those of the global tractography method published by Reisert and colleagues (2009), which scored highest at the FiberCup (see Fig. 7.9a).

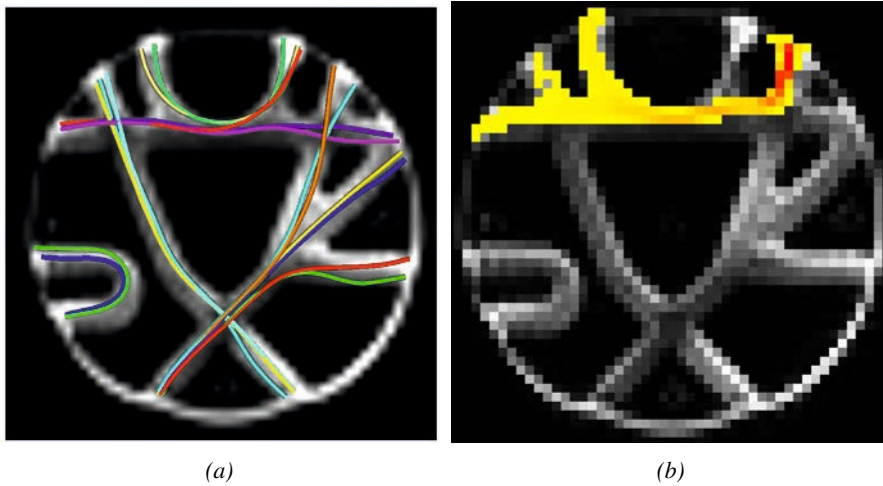


Figure 7.9: Results of the winning method of the FiberCup and probabilistic tractography on the phantom. a) Result of the winning global tractography method of the FiberCup. b) Visitation map of probabilistic tractography performed with bedpostx seeded in spatial position 7. (reprints from (Fillard et al., 2011) and its supplementary material, respectively)

### 7.3.2 Comparison with deterministic and probabilistic tractography

Plausibility Tracking was also tested for connecting different regions in the brain of one adult data set from the cohort described in chapter 6.2. In order to evaluate the method on major pathways, it was compared to probabilistic as well as deterministic tractography, as implemented in MRtrix. Three separate points  $A$  were chosen in the *prefrontal cortex* (PFC), within *Brodmann area 45* (BA45) and in the *dorsal motor cortex* (MC), all in the left hemisphere of a single subject. Then the (according to the underlying dMRI data) most plausible connections with a large number of other points  $B_i$  covering the gray-white matter interface that was reached by probabilistic tractography, excluding locations of the same gyrus in which the corresponding  $A$  is located, were computed. In the case of  $A_{PFC}$ , points  $B_{PFC,i}$  were limited to the right PFC to demonstrate the possibility to focus the analysis on distinct connections.

Plausibility tracks were initialized with a control point distance of 15 mm based on 25 000 probabilistic streamlines started in each of the voxels containing  $A_{PFC}$ ,  $A_{BA45}$

and  $A_{MC}$ , respectively. The deterministic streamlines were selected from whole-brain tractography performed with MRtrix based on CSD generating 250 000 tracks. In order to obtain a reasonable number of deterministic tracks, those were selected that intersect with a sphere of radius 3.6 mm around the points  $A_{PFC}$ ,  $A_{BA45}$  and  $A_{MC}$ , respectively. Constraining the spheres to the white matter led to effective volumes of  $86 \text{ mm}^3$  (PFC),  $149 \text{ mm}^3$  (BA45) and  $178 \text{ mm}^3$  (MC).

Fig. 7.10 shows a comparison of probabilistic tractography, deterministic streamline tractography and Plausibility Tracking. Note that here, for the purpose of comparison, the probabilistic tractography is represented as a collection of streamlines rather than a visitation map, which is common practice. This implies that no thresholding is applied. For some connections, the results of the three methods look quite similar, e.g. when considering connections with  $A_{MC}$  as shown in Fig. 7.10. In other areas it is possible to find connections in a much wider range with Plausibility Tracking than with deterministic tractography. More specifically, Plausibility Tracking finds connections to more locations within a single target area as well as to more different target areas compared to deterministic tractography. On the other hand, Plausibility Tracking removes many implausible tracks that obscure the fiber bundles in probabilistic tractography. These tracks may have low plausibility scores or do not connect the predefined regions. Moreover, the plausibility tracks are smooth due to the representation with splines.

Fig. 7.11 shows the probability distribution of plausibility values for the computed connections. In most cases the method was able to find very plausible connections for the selected pathways in the brain. The peak at a plausibility of zero is due to the fact that the track's plausibility was set to zero if the pathway leaves the white matter area, even if only in a small fraction of the path. This strict criterion was chosen because it was considered better to eliminate some correct tracks rather than accept questionable ones. To ensure comparability, the same plausibility threshold was used for all connections (0.85). With this threshold, a relatively small fraction of tracks was excluded (see Fig. 7.11).

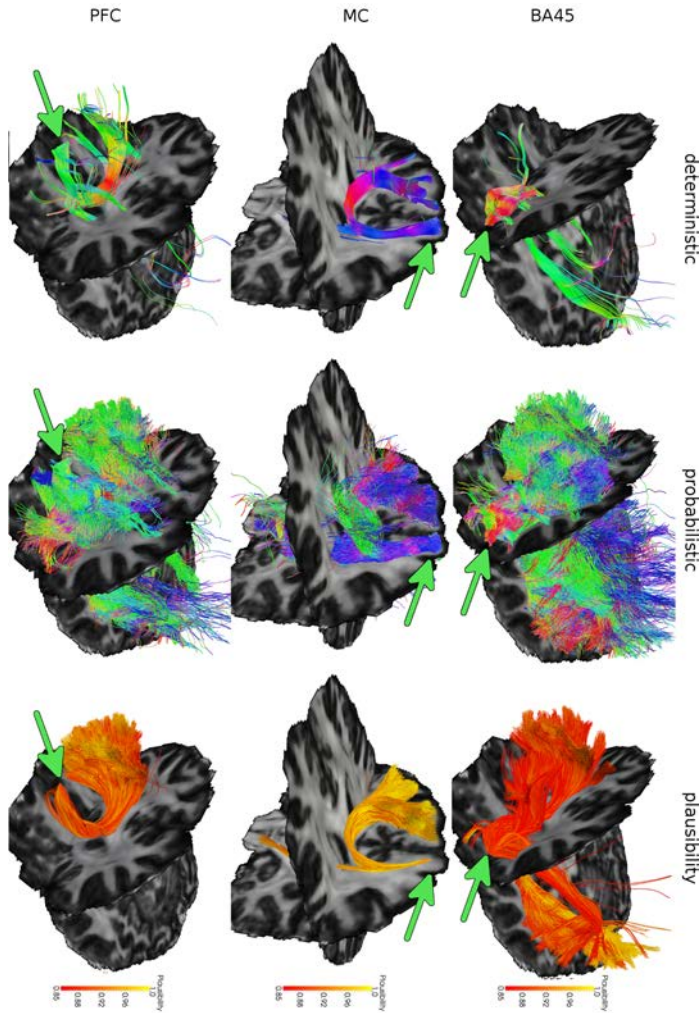


Figure 7.10: Comparison of deterministic and probabilistic tractography with Plausibility Tracking. Plausibility Tracking (right column) finds connections to a much wider range of areas than deterministic streamlines (left column) and shows much smoother and less noisy pathways than probabilistic tractography (middle column). As expected, in many cases the most plausible pathways coincide with the deterministic streamlines. Tracks with a plausibility (according to the underlying dMRI data) lower than 0.85 are not shown. Arrows indicate the seed regions. While the coloring of the Plausibility tracking represents the plausibility values (according to the scale bar), the colors of the probabilistic and deterministic tractography results indicate the local streamline orientation in standard RGB color-coding.

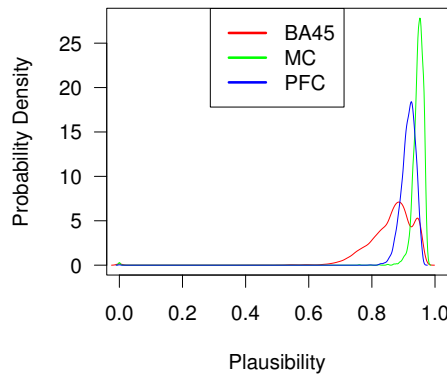


Figure 7.11: Distribution of the plausibility of connections with points in BA45, MC and PFC.

## 7.4 Applications

### 7.4.1 Reconstruction of distinct fiber bundles

Plausibility Tracking was used for reconstruction of different fiber bundles in the human brain. Fig. 7.12 shows the arcuate and uncinate fasciculus as well as the corticospinal tract and cingulum. All tracks were computed with the parameters described in section 6.5, only the number of control points has been adapted to account for the individual shape of pathways.

Table. 7.1 lists the number of tracks that have been computed for every fiber bundle and the percentage of tracks that reached plausibility values above 80 %. It also tells the number of control points ranging from 5 for the rather straight CST and 9 for the more complexly shaped cingulum bundle. The processing time for each bundle was achieved on a computer workstation with an Intel® Core™ i7-2600K CPU at 3.40 GHz. As expected, the processing time greatly depends on the number of tracks that build the fiber bundle. A second influence is the number of control points as can be seen in the last column. The higher the number of control points, the longer it takes to compute the most plausible pathway of a connection although the relation does not appear to be linear.

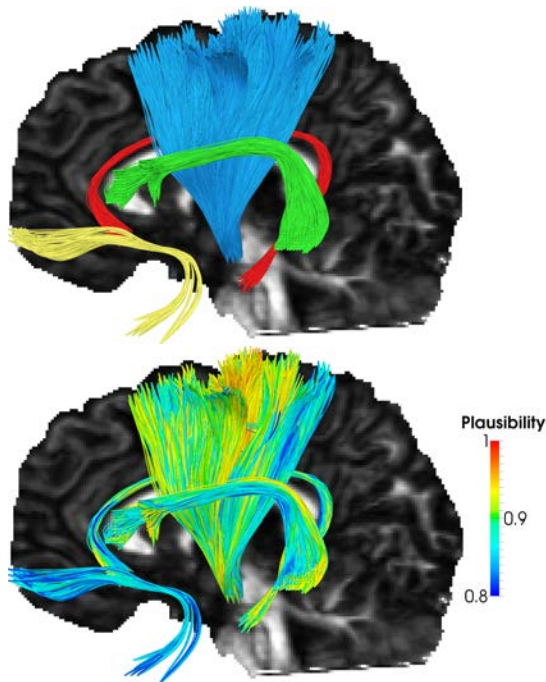


Figure 7.12: Reconstruction of four major fiber bundles. In the upper picture, the arcuate (green) and uncinate (yellow) fasciculus as well as the CST (blue) and the cingulum (red) are shown. The bottom view visualizes the plausibility values of the tracks. Only tracks with a plausibility higher then 0.8 are shown.

Pathway	Number of Tracks	Plausibility >0.8	Control Points	Time [minutes]	Seconds per Track
<div></div> Arcuatus	7986	90.1 %	7	89.0	0.67
<div></div> Uncinate	1259	98.8 %	7	21.0	1.00
<div></div> CST	11643	98.5 %	5	92.7	0.48
<div></div> Cingulum	650	99.2 %	9	18.8	1.73

Table 7.1: Computational performance of Plausibility Tracking shown on four different fiber bundles. The processing time greatly depends on the number of tracks and number of control points.

### 7.4.2 Connections through minor pathways

Having seen good results with the reconstruction of long major pathways raised the question if Plausibility Tracking could also be applied to short minor pathways. As described in the methods section, an additional constraint by waypoint masks may support the initialization through probabilistic tractography as well as the optimization for the most plausible pathway. When using waypoint masks, the obtained pathway is the most plausible under the condition that all waypoint masks are crossed. An example of Plausibility Tracking with this constraint can be seen in Fig. 7.13 where the most plausible tracks between substantia nigra and putamen are shown with and without constraints for the initializing probabilistic tracks and Plausibility Tracking.

Fig. 7.14a shows the dominance of the fiber bundle (most dominant, second or third) that was chosen in every voxel. The connections situated more dorsally mainly passed through the most dominant fiber directions, while the ventral tracks mainly used minor directions. Despite the minority of these directions, the local plausibility values obtained in these regions were almost as high as those obtained in the dorsal connection, as can be seen in Fig. 7.14b.

### 7.4.3 Mapping indices onto individual fiber bundles

The purpose of using an atlas that defines multiple planes is to ensure that corresponding parameters which are mapped onto the pathway are accumulated in a reproducible manner across subjects. Fig. 7.15 visualizes the improvement when the parametrization of a fiber bundle was guided by multiple planes. The arcuate fasciculus follows a complexly shaped pathway and is therefore excellently suited for showing the advantage of this method. The borders between sections, which were used to accumulate index values along the fiber bundle, were much better defined when using multiple planes.

To show the potential of the presented method, indices derived from the fODF via Bingham functions were mapped onto an inter-hemispheric pathway between left and right BA45, which holds parallel, crossing and fanning fibers as shown in Fig. 7.16. As expected, FD and FF of this pathway are highest within the *corpus callosum* (CC), decrease to a minimum when crossing the *superior longitudinal fasciculus* (SLF) and the *corona radiata* (CR) and increase slightly in the regions of BA45. One can assume



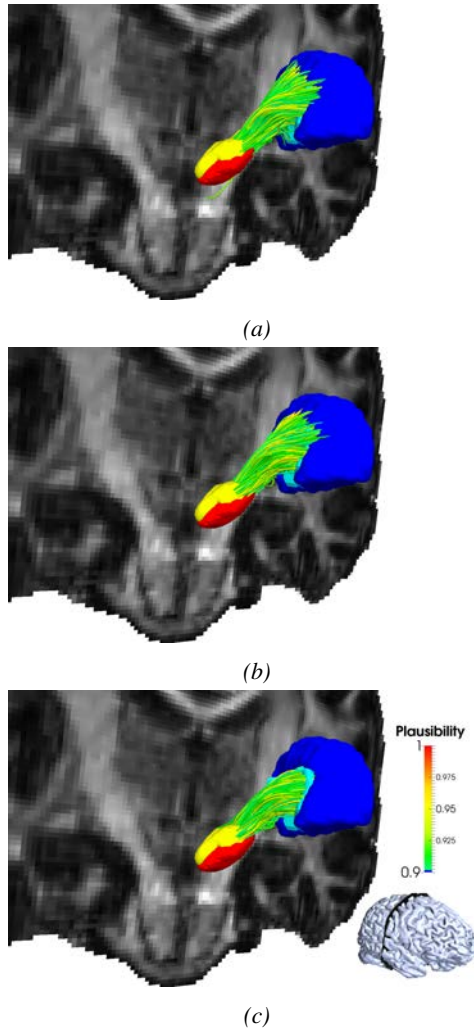


Figure 7.13: Effect of waypoint masks (yellow and light-blue) on the connection between substantia nigra (red) and putamen (blue). Colors of the tracks indicate their plausibility. The orientation is supported by a coronal slice of an FA map in the background and the three dimensional brain in the foreground. a) Waypoint masks have not been used to constrain the connection. b) Waypoint masks were used to force probabilistic tracks that were used for the initialization. c) Waypoint masks were used for both, the initializing probabilistic tracks and Plausibility Tracking.

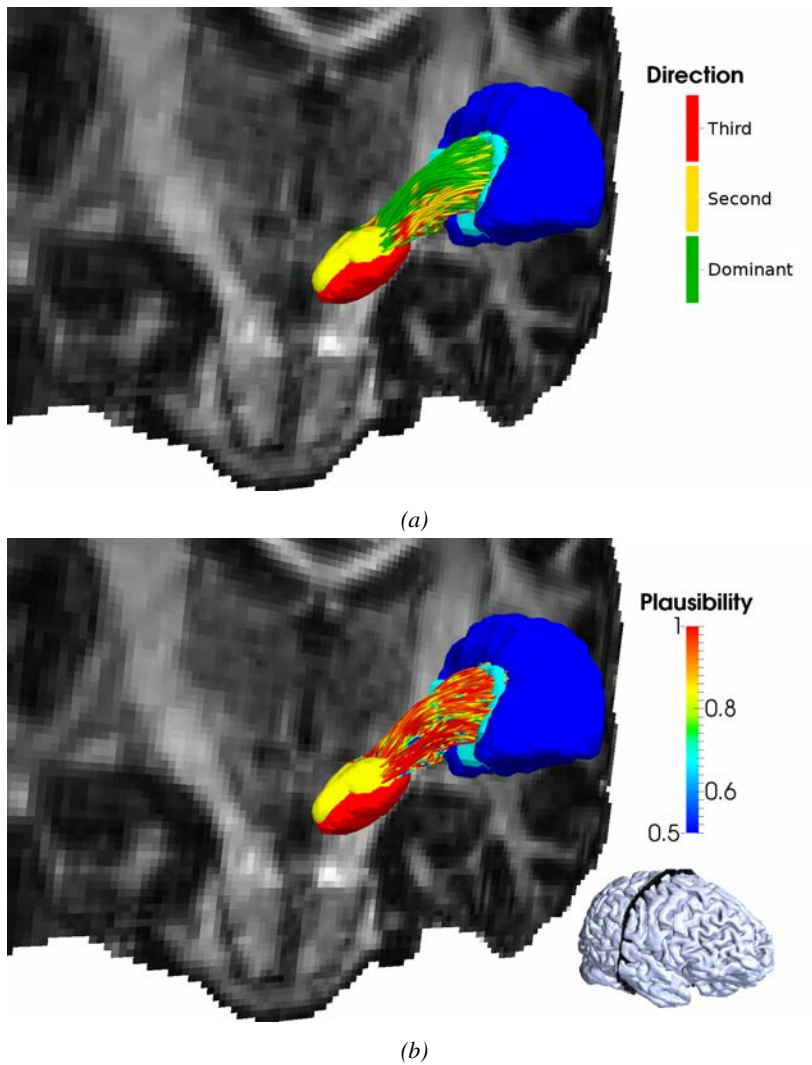


Figure 7.14: Connection between substantia nigra and putamen. a) The dorsal tracks mainly use the most dominant fiber direction (green) while the more ventral tracks pass through second (yellow) or even least dominant (red) directions. b) Local plausibility values mapped onto the pathway. The ventral connections reach equally high local plausibility values as the dorsal tracks although they pass through minor dominant fiber bundles.

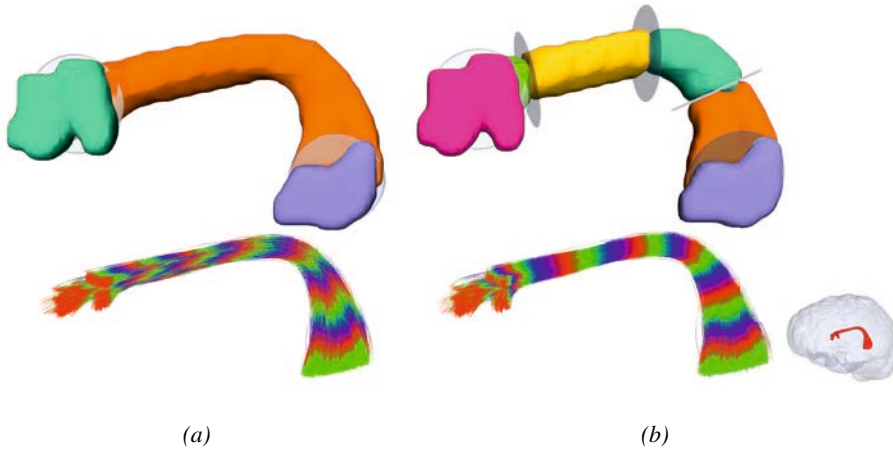


Figure 7.15: Parametrization of the left arcuate fasciculus of a single subject. The top row shows the atlas that defines the intersecting planes. These planes are placed between different labels of the atlas. Neighboring sections, in which indices are accumulated, are represented by red, green and blue colors in the bottom row. The small head on the lower right shows the position of the arcuate fasciculus in the brain. a) Two planes are not sufficient to guarantee a clean parametrization of the whole fiber bundle. The sections are not clearly separated from each other. b) Well defined borders between neighboring compartments are visible when guiding the parametrization with multiple planes.

that the compact fiber configuration in the corpus callosum widens in the crossing area to allow fibers from SLF and CR to intersect. Accordingly, FF decreases because not all fibers in this area belong to the fiber bundle of interest. In the gyri, FD and FF increase again as the fiber bundle compacts. Still, FD and FF do not reach the same level as in the corpus callosum because short association fibers and other gyral connections consume space. The value of FS supports this observation as it increases in the transition areas of different fiber densities. Coming from the CC, fibers are fanning out to intersect with the crossing-fiber bundles. The increase of FS in the middle of the CC may be explained with partial voluming with the septum pellucidum.

#### 7.4.4 Comparing indices between groups

To compare direction dependent indices derived from CSD Plausibility Tracking was applied to the *inferior longitudinal fasciculus* (ILF) of all subjects. The ILF was defined

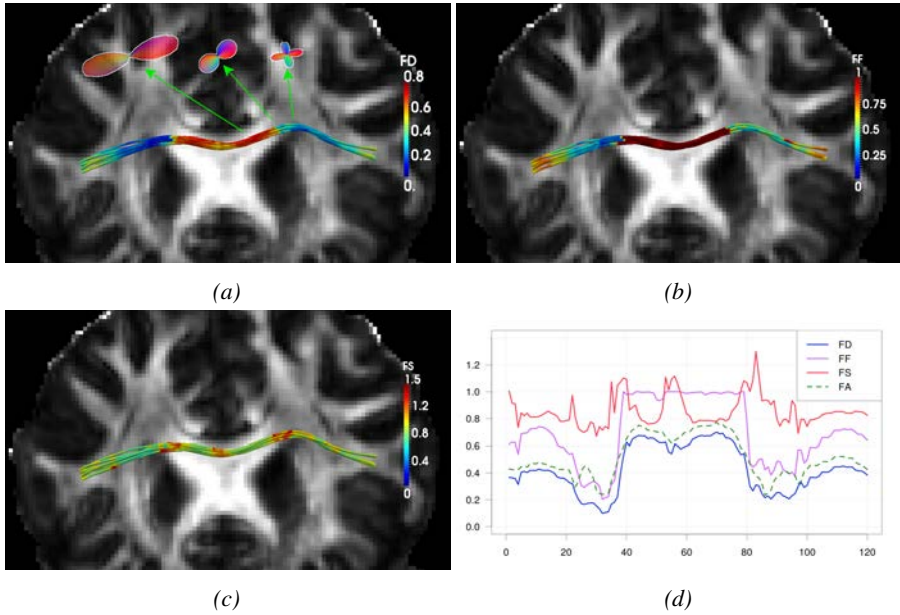


Figure 7.16: Indices along the inter-hemispheric connection between left and right BA45, overlaid to a coronal slice of an FA map. It can be seen that the values of FD and FF are highest in the corpus callosum as shown in panes (a) and (b), respectively. They show lowest values where the pathway crosses the corona radiata. In pane (c) one can also see that FS increases in areas where the density of fibers changes, e.g. in the transition from the corpus callosum to the crossing with the corona radiata. As a reference, the plot of FD, FF and FS (d) additionally shows the values of FA which show a similar profile as FD.

Exemplary fODFs with different fiber configurations are visualized as glyphs in pane (a).

by its end regions according to Mori and colleagues (2008), and initialized with five control points evenly distributed on the pathway. Tracks with a plausibility value less than 0.75 were considered implausible and therefore excluded from the analysis. Fig. 7.17 shows the plausible tracks of the ILF color coded with their plausibility value.

In order to get an impression of the distribution of plausibility values within the pathway, Fig. 7.18 shows the probability densities of the track's plausibility values per subject. For some connections (0.4% in children and 1.7% in adults) the optimizer was not able to find a plausible pathway within the white matter area, but the majority of tracks reached a plausibility of more than 0.75. The strong bimodal distribution of plausibility values as visualized in Fig. 7.18 clearly shows that the optimizer was either

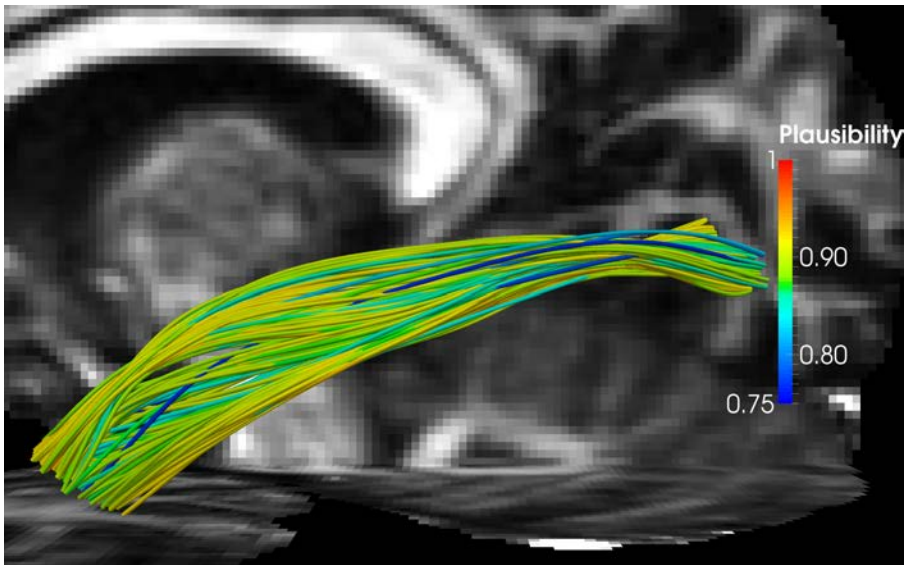


Figure 7.17: Pathway of the left ILF modeled by Plausibility Tracking in one subject, overlaid to a sagittal slice of a FA map through the left occipital cortex. The tracks with a plausibility value greater than 0.75 are shown and color coded with their individual plausibility value.

able to find a very plausible pathway or failed completely, which makes it easy to decide which tracks are realistic. Only very few connections show intermediate plausibility values. In order to suppress questionable tracks, only those with a plausibility of at least 0.75 were considered for further analysis.

Bingham derived indices were used in a group comparison study and placed in relation to indices of the diffusion tensor. All indices were mapped onto the individual pathways of the ILF (see Fig. 7.19) and accumulated separately for statistical evaluation.

In Fig. 7.20, Bingham derived indices (FD, FS and FF) and tensor derived indices (FA, AD, RD) were plotted as group medians along the left ILF from the temporal pole to the occipital region. The curves of FD and FA are remarkably similar, thus suggesting that the main factor influencing the FA in this region is the density of fibers in the main bundle. Consequently, they show a significant difference between children and adults at the same location on the pathway (as indicated by green shading). This significant difference emerges where fibers of the inferior fronto-occipital fasciculus

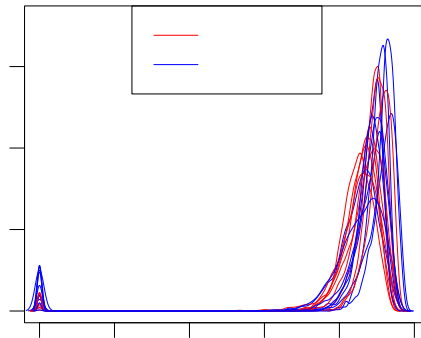


Figure 7.18: Distribution of plausibility values plotted for the ILF of all subjects.

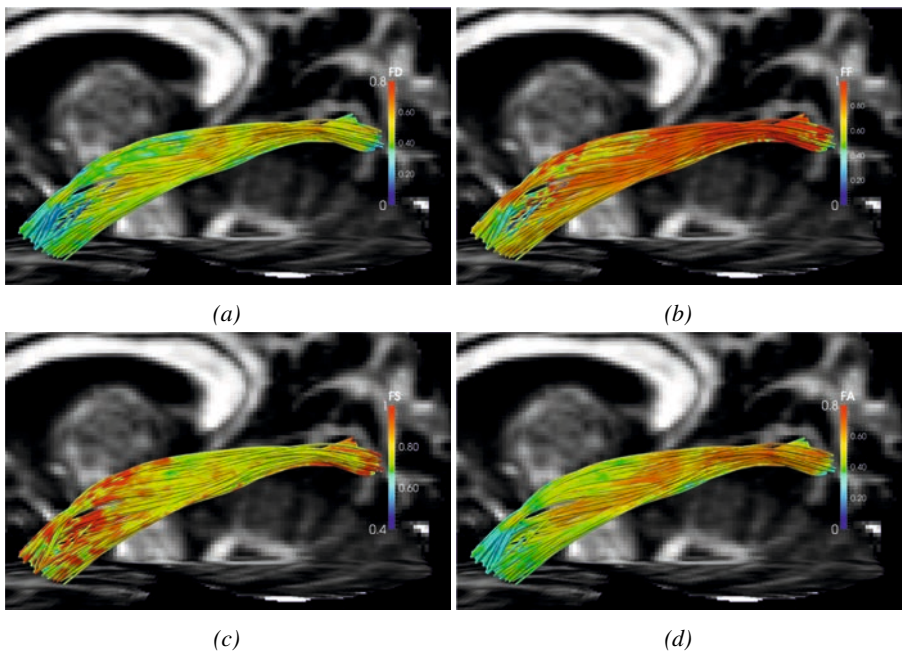


Figure 7.19: Indices mapped onto the ILF pathway of a representative subject. a) Fiber density (FD); b) Fiber fraction (FF); c) Fiber spread (FS); d) Fractional anisotropy (FA).

(IFOF) and a transcallosal fiber bundle join the ILF within the temporal lobe, which can be seen nicely in Fig. 7.21.

Along the ILF, RD appeared to be significantly higher in the group of children than in the adults within the anterior half of the ILF, which could be interpreted as areas of increased crossing and/ or fanning of fibers compared to adults. The difference in AD is an observation that is probably impossible to interpret in this context. In contrast, indices FS and FF provide a little more solid ground for a hypothesis about the fiber configuration in this area. All along the temporal lobe where the ILF interacts with the IFOF and the transcallosal fibers, FS was higher in children than in adults, suggesting that the fibers were spreading more strongly in the younger subjects than in the adults. One possible reason for this effect might be the pruning of connections that are not well aligned with the ILF. In the area where group differences of FD and FA become obvious, another effect seems to dominate the fiber configuration: FF was significantly higher in adults than in children, suggesting that the ILF matures later than the crossing-fiber bundles in this area.

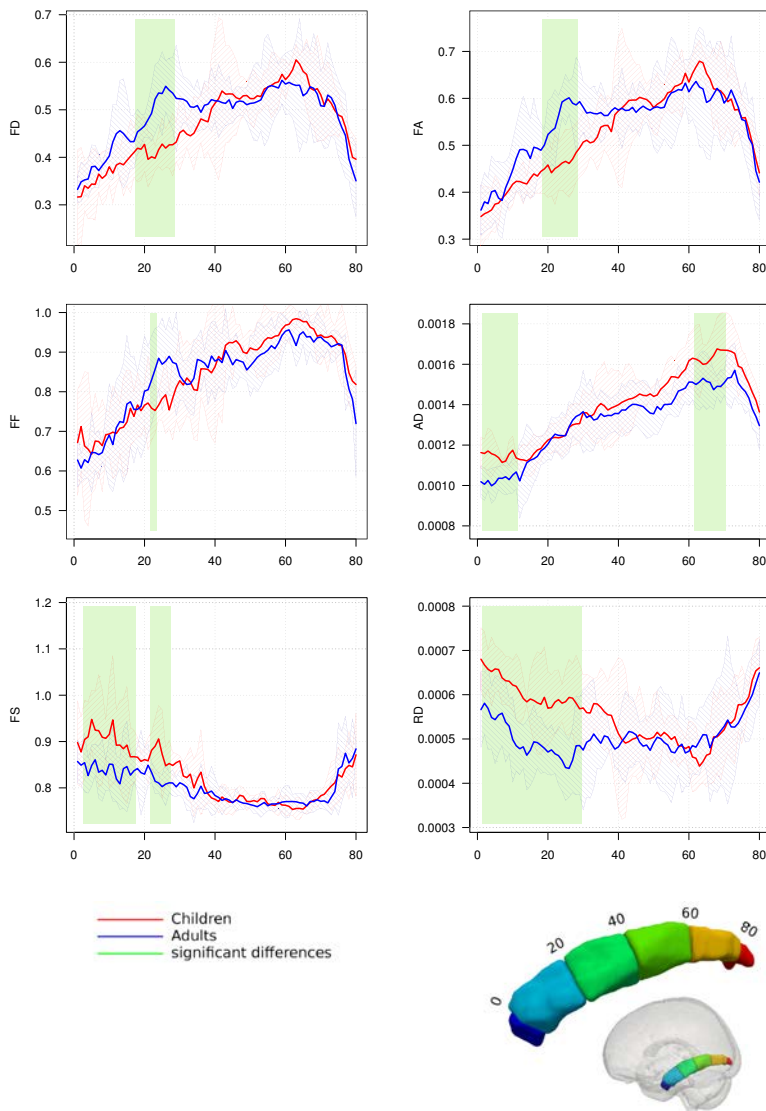


Figure 7.20: Different indices sampled along the ILF. The median values are plotted separately for children (red) and adults (blue) from temporal ( $x=0$ ) to occipital ( $x=80$ ). The shaded red and blue areas show the variation within the groups, computed as 2 MAD (Median Absolute Deviation). The areas highlighted in green indicate significant differences between the groups ( $p < 0.05$ , corrected).



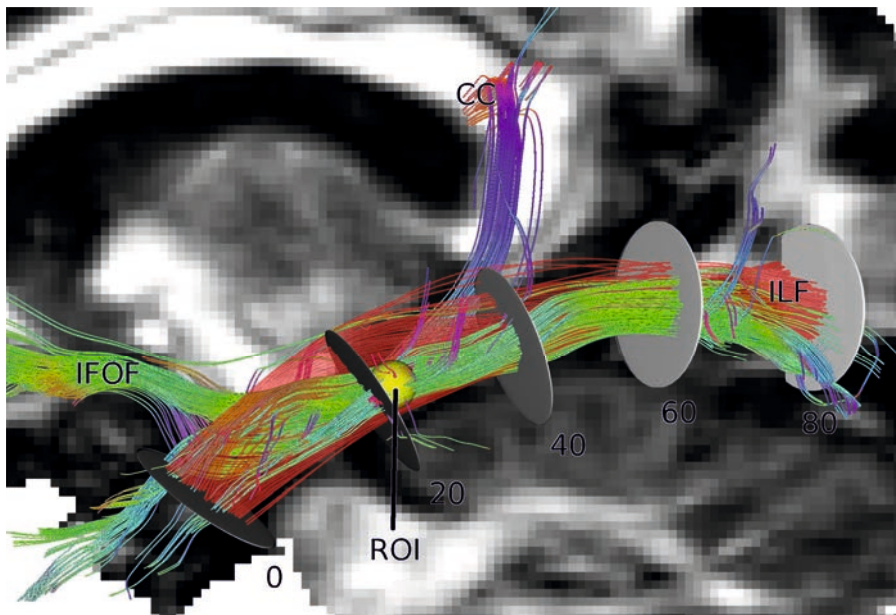


Figure 7.21: Fiber bundles interacting with the ILF within the temporal lobe. Tracks of deterministic streamline tractography that cross the ROI (yellow) are visualized together with the plausibility tracks of the ILF (red, transparent) and the planes that separate the sections of the atlas (gray disks).

## 8 | Discussion

### 8.1 Overview

In this thesis, a framework is presented for quantifying microstructural tissue properties along pathways that connect distant functionally or anatomically defined regions in the human brain. As a basis, a new global tractography method was applied and referred to as *Plausibility Tracking*, which is introduced in this thesis. Plausibility Tracking was used for determining local directions of the connecting pathway and to evaluate microstructural properties that correspond specifically to the pathway of interest. This allowed separation of the properties of different fiber compartments within a voxel and selection of data that were relevant for a specific connection. The hypothesis was that the new method can identify microstructural changes more specifically than previous methods. To evaluate this hypothesis, the method was applied to the inferior longitudinal fasciculus in a group of children and a group of adults.

The term *plausibility* describes how well the pathway of a fiber track can be explained by the local model that represents the underlying measurements of diffusion weighted MRI, and accordingly, the microstructural fiber configuration. Although the concept of plausibility is very general, here it relies on the theoretical assumption that the local model describes the local fiber configuration completely and axonal pathways can be described as smooth curves.

In section 8.2 of this chapter, the presented framework is compared to previous methods for comparing microstructural tissue properties between groups of subjects. The use of constrained spherical deconvolution and the indices obtained by fitting a Bingham function to the peaks of the fODFs are discussed in sections 8.3 and 8.4,

respectively. The new global tractography method named *Plausibility Tracking* is reviewed in section 8.5, followed by a discussion of how the indices are mapped onto the individual pathways in section 8.6. Chapter 9 finally summarizes the novelties presented in this thesis and gives an outlook on possible future developments.

## 8.2 Comparison to other methods

Compared to other existing methods for detecting changes or differences in the brain's white matter, this method differs in some ways. While with TBSS and VBA the whole brain is analyzed by default, TBA evaluates only distinct pathways.

TBSS is based on a skeleton of maximal FA and therefore inadequately represents areas with characteristically low FA, such as crossing. In addition, the limitation to the center line of the white matter with maximal FA gives rise to a bias in the estimated bundle properties. The third limitation comes from the use of tensor derived indices, which do not adequately represent the fiber configuration in crossing or fanning regions. This latter limitation was tackled by Jbabdi and colleagues (2010), who used a multi-compartment model.

VBA, on the other hand, does not explicitly concentrate on high FA values, but comes along with a strong smoothing that is prone to hiding local variances in the tissue's structure and changes the statistics (Jones et al., 2005). In contrast, the TBA method proposed in this thesis reduces smoothing to a minimum (caused only by motion correction), keeping the individual data as unbiased as possible. It allows the analysis of connections realized through minor fiber bundles as well as the major tracts and separates the dMRI information from different tracts.

In contrast to previous methods of TBA (Corouge et al., 2006; Lebel et al., 2008; Colby et al., 2012), this method analyzes direction dependent indices along the tract, which potentially gives more specific information about the underlying fiber structure than rotationally invariant indices do. For the method presented here, the user has to do both, choose a pathway of interest, and create a suitable atlas, if it does not already exist. The advantage of this slightly more laborious approach is that anatomical peculiarities of the individual pathways' shapes are taken into account and multiple intersecting planes guarantee a reliable correspondence across subjects.

## 8.3 Constrained spherical deconvolution

Constrained spherical deconvolution is a sophisticated method to describe fiber configurations in areas where axons are running in parallel as well as in areas of complex crossings. Nevertheless, it is not perfect and its limitations should be known. The spherical functions include negative values that (although suppressed as much as possible by the non-negativity constrained of CSD) produce negative lobes that area biologically impossible.

Negative as well as positive spurious peaks cannot be completely omitted as the model is composed of a truncated series of spherical functions that inevitably cause ringing artifacts. As demonstrated by Parker and colleagues (2012) these artificial peaks occur at predictable angles when using CSD. In a controlled environment with known fiber configuration these could be predicted and filtered out. Unfortunately, this task gets challenging with noisy data of unknown, complex fiber configurations. Possible solutions may include the use of multiple orders for the deconvolution and the integration of information from neighboring voxels. The use of higher orders is limited by two factors. First, it would be necessary to change the imaging protocol to record more diffusion directions, which would increase the scanning time. Second, higher orders are more sensitive to noise (Anderson, 2005) and hence produce a different kind of spurious peaks.

Probably the biggest issue arises from the fact that it is not possible to approximate sharp peaks with reasonable orders of CSD. Theoretically, when computing the deconvolution kernel from a voxel with parallel fibers and than deconvolving the signal attenuation from exactly the same voxel with the kernel, the fODF should resemble a Dirac function. Due to the truncation of the spherical harmonic series, this cannot be attained.

In contrast to most other methods CSD does not describe the diffusion in a voxel, but translates the measurements directly into a fiber orientation density function. The user does not have to estimate the fiber configuration from a given description of diffusion, instead he or she gets a direct measure of fiber density in every direction. One has to keep in mind that this measure is only valid under the assumption that the diffusive properties of all fiber bundles in the brain resemble those of the bundle that was used to compute the deconvolution kernel. To circumvent this issue, some research groups are

working on methods to estimate fiber bundle specific deconvolution kernels. However, no suitable solution has been published yet.

## 8.4 Indices based on Bingham functions

In this thesis, indices based on Bingham functions that are fitted into the peaks of fODFs (Riffert et al., 2014) are used to describe differences between children and adults in the ILF. They provide biophysically meaningful indices that describe the density of fibers in each fiber bundle. Additionally, measures that describe geometrical configurations of fibers and bundles are quantified. These are the fiber spread and fiber fraction. The spread describes the divergency of fibers within a bundle, the fiber fraction the density of the current fiber bundle in relation to crossing bundles. Biologically, the difference between spreading and crossing is hard to define and is not measurable with current resolutions of MR scanners. The distinctive feature used here is of a very practical nature: if the model is able to separate two directions, then they are considered different fiber bundles. If the model is not able to separate the bundles, their directional uncertainty is considered as fiber spread within the bundle. Accordingly, the definition of these two measures depends on the order of spherical harmonics used for CSD because higher orders are more suitable for the separation of peaks.

The fitting as described by Riffert and colleagues (2014) considers only the peak area of each glyph. This procedure reduces the risk of the Bingham function shape being influenced by other fiber bundles crossing at small angles. The downside is that only a small fraction of the fODF shape is used to fit the Bingham functions. Also, in contrast to the Bingham function, the fODF does not necessarily become zero between two crossing fiber bundles. Accordingly, the sum of fiber densities computed from the Bingham functions does not necessarily match the fiber density in the voxel as computed directly from the fODF.

The greatest problem is that the local model is not able to describe sharp peaks adequately, which was discussed in the previous section. The general question is if the level of abstraction, when fitting a model (the Bingham function) to another model (CSD), is suitable when other methods are able to directly fit the Bingham functions into the diffusion signal (Kaden et al., 2008; Sotiropoulos et al., 2012). A

great advantage of this procedure is that it elegantly circumvents the model selection problem, which is inherent to all multi-compartment models, by using CSD and a straight forward peak finding algorithm to decide how many fiber bundles should be modeled.

The reason for choosing indices from Bingham functions fitted into fODFs from constrained spherical deconvolution lies in the reliable model selection routine, the low requirements on the imaging protocol and the efficient computation time that all make the method applicable for every day use.

## 8.5 Plausibility Tracking

The tract specific analysis of direction dependent indices is supported by Plausibility Tracking, a new global tractography method that provides a reliable direction of the pathway all along the tract. In contrast to previously published methods of curve fitting (Tuch, 2002; Jbabdi et al., 2007), Plausibility Tracking is initialized by probabilistic tractography that produces a good estimate of the initial spline parameters. With this initialization, a fast gradient descent algorithm can be used to find the global optimum very quickly. Outliers from the initial probabilistic tractography have little impact on the outcome of the final Plausibility Tracking as a two stage filter is implicitly implemented. First, multiple probabilistic tracks are required to initialize a pathway so that connections with low probability (i.e., with very few probabilistic tracks) are ignored. Second, the estimation of the spline parameters acts as a filter itself because connections that are implausible in the light of the diffusion data obtain a low plausibility value and can be removed. Additional post-processing methods like the recently introduced *spherical-deconvolution informed filtering of tractograms* (SIFT) (Smith et al., 2012) could also be applied.

The measure of plausibility is based solely on the agreement with the direction and uncertainty of one of the peaks described by the local model, although the optimization process uses additional terms regarding curvature constraints and control point distribution. In this sense, *plausibility* denotes how well the local directions can be explained by the local model and assumes that the local model describes the underlying fiber configuration completely. In practice, this requirement is not fulfilled and can never be fully fulfilled due to technical limitations and the indirect estimation of the

fODF (Jones et al., 2013). However, the model has been regarded accurate enough to evaluate properties of differences in white matter tissue (Raffelt et al., 2012). On the other hand, the framework proposed here can be applied to any type of indices derived from local models of higher order.

Another assumption, that has direct influence on the plausibility, has been made regarding the smoothness of the pathway. This smoothness is introduced by modeling the pathway by a spline curve with a limited number of control points and forcing the optimizer to avoid sharp bends. Modeling axonal pathways with a smooth curve might appear questionable, as axons cannot be expected to constantly follow a smooth curve, but may show abrupt changes in direction of certain areas. On the other hand, although dMRI is performed at high resolution, it still summarizes the signal of thousands of axons within one voxel. Hence the “true” axonal pathway is out of reach of dMRI, and the assumption of smoothness refers to the average path of thousands of axons. The method presented here uses a global constraint for smoothness in the whole brain, which is a compromise that prevents implausible bends, but still allows modeling of curved pathways. Within the framework, it would also be possible to create an atlas with expected local curvature angles and adapt the constraint for smoothness locally.

In order to reduce partial voluming and obtain more detailed information about separate local fiber directions one may consider employing latest ultra-high field MR scanners with resolution-optimized protocols as introduced by Heidemann and colleagues (2010; 2012). The higher the spatial resolution, the less complex is the fiber configuration that has to be represented by the local model. In a gedankenexperiment the resolution could be increased to the voxel becoming the size of a single axon’s diameter. Then, a simple local model would be sufficient to describe the fiber layout. When using realistic higher special resolution data, fewer fibers are represented by every fODF and less smoothing is therefore required to model the pathway. Hence, the number of control points that define the spline can be increased accordingly.

The track’s global plausibility value is computed as average of all local plausibility values sampled along the pathway. The effect this simple definition has on local deviations from the optimal direction can be compensated for by sections with good directional accordance with the local model. Accordingly and in contrast to probabilistic tractography, the track’s length does not have a negative impact on its plausibility value. On the other hand, compensating for locally implausible situations poses the

risk of constructing pathways that are biologically impossible, like taking a shortcut through non-white matter areas. In order to prevent this a strict criterion has been set to disregard any pathway that leaves white matter.

## 8.6 Mapping of indices and statistical evaluation

In tract-based analysis it is common standard to pool index values according to the parametrization along the pathway (Corouge et al., 2006; Colby et al., 2012). The atlas-based definition of supporting planes, as described in section 6.6.3, increases the comparability between subjects as the spatial normalization process for the atlas takes characteristics of the individual anatomies into account. Due to the fact that only the atlas is transformed to the individual space instead of diffusion data or index maps, no smoothing artifacts from interpolation are introduced.

As a normal distribution of values cannot be assumed, the values are accumulated by computing their median value rather than the arithmetic mean. This method seems to be much more stable than collecting the maximal values as done in TBSS, but seems to produce less significant differences between the groups. Further evaluations on the distribution of values might provide hints for a more adequate summary of index values within the cross-sections of fiber bundles.

In the present study, direction dependent indices, as recently introduced by Riffert and colleagues (2014), were used to identify properties of the white matter structure. Their specificity was compared to those of indices derived from the diffusion tensor. It was shown that the biophysically meaningful indices allow a more specific characterization of the tissue microstructure than it is possible with the rotationally invariant indices of the diffusion tensor.

In principle, the method is suitable for all kinds of indices derived from a variety of different models. If there are less stringent constraints to the imaging protocol, indices of models that require multiple b-values can be very easily incorporated into the framework. Only the index-maps with their corresponding directions are required. In fact, the full potential of the presented method will unfold when additional indices based on models like CHARMED (Assaf et al., 2004) and AxCaliber (Assaf et al., 2008), which embody a more complete sampling of the diffusion propagator might bring even more insights into myelination or axonal diameter distribution.





## 9 | Summary and outlook

In this thesis, a framework is proposed for comparing direction dependent indices derived from dMRI across subjects. The fully automatic processing pipeline is already applied to more data-sets than presented here and proved its stability.

In order to obtain reliable local directions in the fiber bundles the global tractography method Plausibility Tracking is introduced. Plausibility Tracking provides the most plausible pathway, modeled as a smooth spline curve, between two locations in the brain. The plausibility of a connection is defined by the accordance of the track's directions with the local directions and their uncertainties based on data from dMRI. Compared to other tractography methods Plausibility Tracking provides a spatial expansion similar to probabilistic tractography coupled with smooth tracks, which are globally optimized using the fODF. Therefore this method is relatively robust against local noise and error propagation.

So far, the plausibility of a connection has only been used to identify reasonable tracks, although the measure has much more potential when it is used to characterize the anatomical connectivity between two regions in the brain. Additionally, it could be combined with an integration of local indices like fiber density along the pathway in order to estimate the performance of a connection.

The initialization through probabilistic tractography provides a reliable starting position for the optimization process that allows a fast computation of the most plausible pathways and increases the probability of finding the global optimum. Additionally, probabilistic tractography can be used to filter out improbable connections so that only realistic candidates are being processed.

The parametrization of the pathway is guided by an atlas that is aligned with each subject's anatomy. This procedure takes into account individual peculiarities of the fiber tracts and supports the comparison of corresponding sections of the pathway. In most (if not all) tract-based analysis studies, the indices describing microstructural tissue properties are summarized perpendicular to the pathways center line. Fig. 7.19 reveals that the pattern of index values is not necessarily aligned perpendicular to the pathway, which might decrease the sensitivity of the method. Depending on the stability of these patterns across subjects, the atlas could be used to restrict the collection of values to certain regions, or to abandon the perpendicularity completely and perform a more region based analysis.

It has been shown that the proposed method allows for a more specific interpretation of the white matter's microstructure compared to rotationally invariant indices derived from the diffusion tensor. With the combination of the pathway's shape, new indices could be computed. The average fiber density multiplied with the pathway's cross-section area, for example, would give an estimate of the number of axons forming the particular connection.

I hope the presented method will support researchers to provide new insights into the understanding of anatomy and function of the human brain.

## References

- Aboitiz F, Scheibel AB, Fisher RS, Zaidel E (1992) Fiber composition of the human corpus callosum. *Brain research* 598:143–153.
- Aganj I, Lenglet C, Sapiro G, Yacoub E, Ugurbil K, Harel N (2010) Reconstruction of the orientation distribution function in single-and multiple-shell q-ball imaging within constant solid angle. *Magnetic Resonance in Medicine* 64:554–566.
- Alexander DC (2005) Multiple-fiber reconstruction algorithms for diffusion MRI. *Annals of the New York Academy of Sciences* 1064:113–133.
- Alexander DC, Barker G, Arridge S (2002) Detection and modeling of non-Gaussian apparent diffusion coefficient profiles in human brain data. *Magnetic Resonance in Medicine* 48:331–340.
- Alexander DC, Seunarine KK (2011) *Diffusion MRI: Theory, Methods and Applications* (editor Jones, DK), chapter 27, pp. 451–464 Oxford University Press.
- Anderson A, Ding Z (2002) Sub-voxel measurement of fiber orientation using high angular resolution diffusion tensor imaging In *Book of abstracts: Tenth Annual Meeting of the International Society for Magnetic Resonance in Medicine*. Berkeley, CA: ISMRM, Vol. 10, p. 440.
- Anderson AW (2005) Measurement of fiber orientation distributions using high angular resolution diffusion imaging. *Magnetic Resonance in Medicine* 54:1194–1206.
- Anwander A, Tittgemeyer M, von Cramon DY, Friederici AD, Knösche TR (2007) Connectivity-based parcellation of broca’s area. *Cerebral Cortex* 17:816–825.

- Ashburner J, Friston KJ (2000) Voxel-based morphometry - the methods. *Neuroimage* 11:805–821.
- Ashburner J, Friston KJ (2001) Why voxel-based morphometry should be used. *Neuroimage* 14:1238–1243.
- Ashburner J, Friston KJ (2005) Unified segmentation. *Neuroimage* 26:839–851.
- Assaf Y, Basser PJ (2005) Composite hindered and restricted model of diffusion (CHARMED) MR imaging of the human brain. *Neuroimage* 27:48–58.
- Assaf Y, Blumenfeld-Katzir T, Yovel Y, Basser PJ (2008) AxCaliber: a method for measuring axon diameter distribution from diffusion MRI. *Magnetic Resonance in Medicine* 59:1347–1354.
- Assaf Y, Freidlin RZ, Rohde GK, Basser PJ (2004) New modeling and experimental framework to characterize hindered and restricted water diffusion in brain white matter. *Magnetic Resonance in Medicine* 52:965–978.
- Avants BB, Epstein CL, Grossman M, Gee JC (2008) Symmetric diffeomorphic image registration with cross-correlation: evaluating automated labeling of elderly and neurodegenerative brain. *Medical image analysis* 12:26–41.
- Avants BB, Tustison NJ, Song G, Cook PA, Klein A, Gee JC (2011) A reproducible evaluation of ANTs similarity metric performance in brain image registration. *Neuroimage* 54:2033–2044.
- Basser PJ, Jones DK (2002) Diffusion-tensor MRI: theory, experimental design and data analysis—a technical review. *NMR in Biomedicine* 15:456–467.
- Basser PJ, Mattiello J, LeBihan D et al. (1994) Estimation of the effective self-diffusion tensor from the NMR spin echo. *Journal of Magnetic Resonance-Series B* 103:247–254.
- Basser PJ, Pajevic S, Pierpaoli C, Duda J, Aldroubi A (2000) In vivo fiber tractography using DT-MRI data. *Magnetic resonance in medicine* 44:625–632.

Basser PJ, Pierpaoli C et al. (1996) Microstructural and physiological features of tissues elucidated by quantitative-diffusion-tensor MRI. *Journal of magnetic resonance. Series B* 111:209–219.

Bear MF, Connors BW, Paradiso MA (2007) *Neuroscience* Wolters Kluwer Health.

Beaulieu C (2002) The basis of anisotropic water diffusion in the nervous system—a technical review. *NMR in Biomedicine* 15:435–455.

Beaulieu C (2006) The biological basis of diffusion tractography In *Biomedical Imaging: Nano to Macro, 2006. 3rd IEEE International Symposium on*, pp. 347–350. IEEE.

Behrens T, Berg HJ, Jbabdi S, Rushworth M, Woolrich M (2007) Probabilistic diffusion tractography with multiple fibre orientations: What can we gain? *Neuroimage* 34:144–155.

Behrens T, Woolrich M, Jenkinson M, Johansen-Berg H, Nunes R, Clare S, Matthews P, Brady J, Smith S (2003) Characterization and propagation of uncertainty in diffusion-weighted MR imaging. *Magnetic Resonance in Medicine* 50:1077–1088.

Behrens TE, Jbabdi S (2009) MR diffusion tractography. *Diffusion MRI: from Quantitative Measurement to in vivo Neuroanatomy*. Elsevier Academic Press, New York pp. 333–351.

Brauer J, Anwander A, Friederici AD (2011) Neuroanatomical prerequisites for language functions in the maturing brain. *Cerebral Cortex* 21:459–466.

Brauer J, Anwander A, Perani D, Friederici AD (2013) Dorsal and ventral pathways in language development. *Brain and Language* 127:289–295.

Brodmann K (1909) *Vergleichende Lokalisationslehre der Großhirnrinde* Barth, Leipzig.

Caan MW, Khedoe H, Poot DH, den Dekker AJ, Olabarriaga SD, Grimbergen KA, van Vliet LJ, Vos FM (2010) Estimation of diffusion properties in crossing fiber bundles. *Medical Imaging, IEEE Transactions on* 29:1504–1515.

- Catmull E, Rom R (1974) A class of local interpolating splines. *Computer aided geometric design* 74:317–326.
- Colby JB, Soderberg L, Lebel C, Dinov ID, Thompson PM, Sowell ER (2012) Along-tract statistics allow for enhanced tractography analysis. *Neuroimage* 59:3227–3242.
- Collins DL, Zijdenbos AP, Kollokian V, Sled JG, Kabani NJ, Holmes CJ, Evans AC (1998) Design and construction of a realistic digital brain phantom. *Medical Imaging, IEEE Transactions on* 17:463–468.
- Corouge I, Fletcher PT, Joshi S, Gouttard S, Gerig G et al. (2006) Fiber tract-oriented statistics for quantitative diffusion tensor MRI analysis. *Medical Image Analysis* 10:786–798.
- Cory D (1990) Measurement of translational displacement probabilities by NMR: an indicator of compartmentation. *Magnetic resonance in medicine* 14:435–444.
- Cossette M, Lévesque M, Parent A (1999) Extrastriatal dopaminergic innervation of human basal ganglia. *Neuroscience research* 34:51–54.
- Dell’Acqua F, Rizzo G, Scifo P, Clarke RA, Scotti G, Fazio F (2007) A model-based deconvolution approach to solve fiber crossing in diffusion-weighted mr imaging. *Biomedical Engineering, IEEE Transactions on* 54:462–472.
- Dell’Acqua F, Scifo P, Rizzo G, Catani M, Simmons A, Scotti G, Fazio F (2010) A modified damped Richardson–Lucy algorithm to reduce isotropic background effects in spherical deconvolution. *Neuroimage* 49:1446–1458.
- Dell’Acqua F, Simmons A, Williams SC, Catani M (2013) Can spherical deconvolution provide more information than fiber orientations? Hindrance modulated orientational anisotropy, a true-tract specific index to characterize white matter diffusion. *Human Brain Mapping* 34:2464–2483.
- Descoteaux M (2008) High Angular Resolution Diffusion MRI Ph.D. diss.
- Descoteaux M, Angelino E, Fitzgibbons S, Deriche R (2006) Apparent diffusion coefficients from high angular resolution diffusion imaging: Estimation and applications. *Magnetic Resonance in Medicine* 56:395–410.

Descoteaux M, Deriche R, Knosche T, Anwander A (2009) Deterministic and probabilistic tractography based on complex fibre orientation distributions. *Medical Imaging, IEEE Transactions on* 28:269–286.

Douaud G, Jbabdi S, Behrens TE, Menke RA, Gass A, Monsch AU, Rao A, Whitcher B, Kindlmann G, Matthews PM et al. (2011) DTI measures in crossing-fibre areas: Increased diffusion anisotropy reveals early white matter alteration in MCI and mild Alzheimer's disease. *Neuroimage* 55:880–890.

Einstein A (1905) Über die von der molekularkinetischen Theorie der Wärme geforderte Bewegung von in ruhenden Flüssigkeiten suspendierten Teilchen. *Annalen der Physik* 322:549–560.

Faria A, Zhang J, Oishi K, Li X, Jiang H, Akhter K, Hermoye L, Lee SK, Hoon A, Stashinko E, Miller M, van Zijl P, Mori S (2010) Atlas-based analysis of neurodevelopment from infancy to adulthood using diffusion tensor imaging and applications for automated abnormality detection. *Neuroimage* 52:415–428.

Fillard P, Descoteaux M, Goh A, Gouttard S, Jeurissen B, Malcolm J, Ramirez-Manzanares A, Reisert M, Sakaie K, Tensaouti F et al. (2011) Quantitative evaluation of 10 tractography algorithms on a realistic diffusion MR phantom. *Neuroimage* 56:220–234.

Fillard P, Poupon C, Mangin JF (2009) A novel global tractography algorithm based on an adaptive spin glass model In *Medical Image Computing and Computer-Assisted Intervention–MICCAI 2009*, pp. 927–934. Springer.

Formica D, Silvestri S (2004) Biological effects of exposure to magnetic resonance imaging: an overview. *Biomedical engineering online* 3:11.

Fritzsche KH, Laun FB, Meinzer HP, Stieltjes B (2010) Opportunities and pitfalls in the quantification of fiber integrity: What can we gain from q-ball imaging? *NeuroImage* 51:242–251.

Funk P (1915) Über eine geometrische Anwendung der abelschen Integralgleichung. *Mathematische Annalen* 77:129–135.



- Ghosh A, Deriche R (2011) Extracting geometrical features & peak fractional anisotropy from the ODF for white matter characterization. In *Biomedical Imaging: From Nano to Macro, 2011 IEEE International Symposium on*, pp. 266–271. IEEE.
- Gong G, Jiang T, Zhu C, Zang Y, Wang F, Xie S, Xiao J, Guo X (2005) Asymmetry analysis of cingulum based on scale-invariant parameterization by diffusion tensor imaging. *Human brain mapping* 24:92–98.
- Good CD, Johnsrude IS, Ashburner J, Henson RN, Friston KJ, Frackowiak RS (2001) A voxel-based morphometric study of ageing in 465 normal adult human brains. *NeuroImage* 14:21–36.
- Gorczewski K, Mang S, Klose U (2009) Reproducibility and consistency of evaluation techniques for HARDI data. *Magnetic Resonance Materials in Physics, Biology and Medicine* 22:63–70.
- Hansen PC (1994) Regularization tools: A Matlab package for analysis and solution of discrete ill-posed problems. *Numerical algorithms* 6:1–35.
- Heidemann RM, Anwander A, Feiweier T, Knösche TR, Turner R (2012) k-space and q-space: combining ultra-high spatial and angular resolution in diffusion imaging using ZOOPPA at 7T. *NeuroImage* 60:967–978.
- Heidemann RM, Porter DA, Anwander A, Feiweier T, Heberlein K, Knösche TR, Turner R (2010) Diffusion imaging in humans at 7T using readout-segmented EPI and GRAPPA. *Magnetic Resonance in Medicine* 64:9–14.
- Jbabdi S, Behrens TE, Smith SM (2010) Crossing fibres in tract-based spatial statistics. *Neuroimage* 49:249–256.
- Jbabdi S, Woolrich M, Andersson J, Behrens T et al. (2007) A Bayesian framework for global tractography. *Neuroimage* 37:116.
- Jeurissen B, Leemans A, Tournier J, Jones D, Sijbers J (2010) Estimating the number of fiber orientations in diffusion MRI voxels: a constrained spherical deconvolution study. *Proceedings of the International Society for Magnetic Resonance in Medicine, Stockholm, Sweden* p. 573.

Jeurissen B, Leemans A, Jones DK, Tournier JD, Sijbers J (2011) Probabilistic fiber tracking using the residual bootstrap with constrained spherical deconvolution. *Human brain mapping* 32:461–479.

Jeurissen B, Leemans A, Tournier JD, Jones DK, Sijbers J (2013) Investigating the prevalence of complex fiber configurations in white matter tissue with diffusion magnetic resonance imaging: Prevalence of multifiber voxels in WM. *Human Brain Mapping* 34:2747–2766.

Joachims T (1999) Making large-scale SVM learning practical In Schölkopf B, Burges C, Smola A, editors, *Advances in kernel methods - support vector learning*. MIT-Press.

Jones DK (2004) The effect of gradient sampling schemes on measures derived from diffusion tensor MRI: A Monte Carlo study. *Magnetic Resonance in Medicine* 51:807–815.

Jones DK, Cercignani M (2010) Twenty-five pitfalls in the analysis of diffusion MRI data. *NMR in Biomedicine* 23:803–820.

Jones DK, Knösche TR, Turner R (2013) White matter integrity, fiber count, and other fallacies: the do's and don'ts of diffusion MRI. *Neuroimage* 37:239–254.

Jones DK, Symms MR, Cercignani M, Howard RJ et al. (2005) The effect of filter size on VBM analyses of DT-MRI data. *Neuroimage* 26:546–554.

Kaden E, Anwander A, Knösche TR (2008) Variational inference of the fiber orientation density using diffusion MR imaging. *Neuroimage* 42:1366.

Kaden E, Knösche TR, Anwander A (2007) Parametric spherical deconvolution: Inferring anatomical connectivity using diffusion MR imaging. *NeuroImage* 37:474–488.

Klein A, Andersson J, Ardekani BA, Ashburner J, Avants B, Chiang MC, Christensen GE, Collins DL, Gee J, Hellier P et al. (2009) Evaluation of 14 nonlinear deformation algorithms applied to human brain MRI registration. *Neuroimage* 46:786–802.

- Koch MA, Norris DG, Hund-Georgiadis M (2002) An investigation of functional and anatomical connectivity using magnetic resonance imaging. *Neuroimage* 16:241–250.
- Kreher B, Mader I, Kiselev V (2008) Gibbs tracking: a novel approach for the reconstruction of neuronal pathways. *Magnetic Resonance in Medicine* 60:953–963.
- Kuo LW, Chen JH, Wedeen VJ, Tseng W (2008) Optimization of diffusion spectrum imaging and q-ball imaging on clinical MRI system. *Neuroimage* 41:7.
- Lazar M, Weinstein DM, Tsuruda JS, Hasan KM, Arfanakis K, Meyerand ME, Badie B, Rowley HA, Haughton V, Field A et al. (2003) White matter tractography using diffusion tensor deflection. *Human brain mapping* 18:306–321.
- Le Bihan D (1991) Molecular diffusion nuclear magnetic resonance imaging. *Magnetic resonance quarterly* 7:1–30.
- Le Bihan D (2003) Looking into the functional architecture of the brain with diffusion MRI. *Nature Reviews Neuroscience* 4:469–480.
- Le Bihan D, Breton E, Lallemand D, Grenier P, Cabanis E, Laval-Jeantet M et al. (1986) MR imaging of intravoxel incoherent motions: application to diffusion and perfusion in neurologic disorders. *Radiology* 161:401–407.
- Lebel C, Walker L, Leemans A, Phillips L, Beaulieu C et al. (2008) Microstructural maturation of the human brain from childhood to adulthood. *Neuroimage* 40:1044–1055.
- Lenglet C, Campbell J, Descoteaux M, Haro G, Savadjiev P, Wassermann D, Anwander A, Deriche R, Pike GB, Sapiro G et al. (2009) Mathematical methods for diffusion MRI processing. *Neuroimage* 45:S111–S122.
- Lim IAL, Faria AV, Li X, Hsu JT, Airan RD, Mori S, van Zijl P (2013) Human brain atlas for automated region of interest selection in quantitative susceptibility mapping: Application to determine iron content in deep gray matter structures. *NeuroImage* 82:449–469.

Lin CP, Wedeen VJ, Chen JH, Yao C, Tseng WYI (2003) Validation of diffusion spectrum magnetic resonance imaging with manganese-enhanced rat optic tracts and ex vivo phantoms. *Neuroimage* 19:482–495.

Malcolm JG, Shenton ME, Rath Y (2010) Filtered multitensor tractography. *Medical Imaging, IEEE Transactions on* 29:1664–1675.

Malcolm J, Kubicki M, Shenton M, Rath Y (2009) The effect of local fiber model on population studies In *Diffusion Modeling and Fiber Cup*, pp. 33–40, London, United Kingdom. MICCAI.

Mori S (2007) *Introduction to diffusion tensor imaging* Elsevier.

Mori S, Crain BJ, Chacko V, Van Zijl P (1999) Three-dimensional tracking of axonal projections in the brain by magnetic resonance imaging. *Annals of neurology* 45:265–269.

Mori S, Oishi K, Jiang H, Jiang L, Li X, Akhter K, Hua K, Faria AV, Mahmood A, Woods R et al. (2008) Stereotaxic white matter atlas based on diffusion tensor imaging in an ICBM template. *Neuroimage* 40:570–582.

Mori S, van Zijl P (2002) Fiber tracking: principles and strategies—a technical review. *NMR in Biomedicine* 15:468–480.

Nelder JA, Mead R (1965) A simplex method for function minimization. *The computer journal* 7:308–313.

Nichols TE, Holmes AP (2002) Nonparametric permutation tests for functional neuroimaging: a primer with examples. *Human brain mapping* 15:1–25.

O'Donnell LJ, Westin CF, Golby AJ (2009) Tract-based morphometry for white matter group analysis. *Neuroimage* 45:832–844.

Parker G, Marshall A, Rosin PL, Drage N, Richmond S, Jones D (2012) A pitfall in the reconstruction of fibre ODFs using spherical deconvolution of diffusion MRI data. *Neuroimage* 65:433–448.

- Parker GJ, Alexander DC (2005) Probabilistic anatomical connectivity derived from the microscopic persistent angular structure of cerebral tissue. *Philosophical Transactions of the Royal Society B: Biological Sciences* 360:893–902.
- Pasternak O, Assaf Y, Intrator N, Sochen N (2008) Variational multiple-tensor fitting of fiber-ambiguous diffusion-weighted magnetic resonance imaging voxels. *Magnetic resonance imaging* 26:1133–1144.
- Poupon C, Rieul B, Kezele I, Perrin M, Poupon F, Mangin JF (2008) New diffusion phantoms dedicated to the study and validation of high-angular-resolution diffusion imaging (HARDI) models. *Magnetic Resonance in Medicine* 60:1276–1283.
- Purves D, Augustine G, Fitzpatrick D, Hall W, LaMantia A, McNamara J, Williams S (2004) *Neuroscience* Sinauer Associates Inc., 3 edition.
- Raffelt D, Tournier J, Rose S, Ridgway GR, Henderson R, Crozier S, Salvado O, Connelly A et al. (2012) Apparent fibre density: A novel measure for the analysis of diffusion-weighted magnetic resonance images. *Neuroimage* 59:3976–3994.
- Reisert M, Mader I, Anastasopoulos C, Weigel M, Schnell S, Kiselev V (2011) Global fiber reconstruction becomes practical. *Neuroimage* 54:955–962.
- Reisert M, Mader I, Kiselev V (2009) Tracking a physical phantom by global fibre reconstruction In *MICCAI Workshop on Diffusion Modelling and the Fiber Cup*, London, United Kingdom. MICCAI, Springer.
- Riffert TW, Schreiber J, Anwander A, Knösche TR (2014) Beyond fractional anisotropy: Extraction of bundle-specific structural metrics from crossing fiber models. *NeuroImage* 100:176–191.
- Scherrer B, Warfield SK (2010) Why multiple b-values are required for multi-tensor models. evaluation with a constrained log-euclidean model In *Biomedical Imaging: From Nano to Macro, 2010 IEEE International Symposium on*, pp. 1389–1392. IEEE.
- Schultz T (2012) Learning a reliable estimate of the number of fiber directions in diffusion MRI In Ayache N, Delingette H, Golland P, Mori K, editors, *Medical Image Computing and Computer-Assisted Intervention â MICCAI 2012*, number 7512 in Lecture Notes in Computer Science. Springer Berlin Heidelberg.

Seok JH, Park HJ, Chun JW, Lee SK, Cho HS, Kwon JS, Kim JJ (2007) White matter abnormalities associated with auditory hallucinations in schizophrenia: a combined study of voxel-based analyses of diffusion tensor imaging and structural magnetic resonance imaging. *Psychiatry Research: Neuroimaging* 156:93–104.

Smith RE, Tournier JD, Calamante F, Connelly A (2012) SIFT: Spherical-deconvolution informed filtering of tractograms. *NeuroImage* 67:298–312.

Smith SM, Jenkinson M, Johansen-Berg H, Rueckert D, Nichols TE, Mackay CE, Watkins KE, Ciccarelli O, Cader MZ, Matthews PM et al. (2006) Tract-based spatial statistics: voxelwise analysis of multi-subject diffusion data. *Neuroimage* 31:1487–1505.

Smith SM, Jenkinson M, Woolrich MW, Beckmann CF, Behrens T, Johansen-Berg H, Bannister PR, De Luca M, Drobnjak I, Flitney DE et al. (2004) Advances in functional and structural MR image analysis and implementation as FSL. *Neuroimage* 23:S208.

Smith SM, Nichols TE (2009) Threshold-free cluster enhancement: addressing problems of smoothing, threshold dependence and localisation in cluster inference. *Neuroimage* 44:83–98.

Snook L, Plewes C, Beaulieu C et al. (2007) Voxel based versus region of interest analysis in diffusion tensor imaging of neurodevelopment. *Neuroimage* 34:243–252.

Sommer M, Koch MA, Paulus W, Weiller C, Büchel C (2002) Disconnection of speech-relevant brain areas in persistent developmental stuttering. *The Lancet* 360:380–383.

Sotiropoulos SN, Behrens TE, Jbabdi S (2012) Ball and rackets: inferring fiber fanning from diffusion-weighted MRI. *Neuroimage* 60:1412–1425.

Stejskal E, Tanner J (1965) Spin diffusion measurements: spin echoes in the presence of a time-dependent field gradient. *The journal of chemical physics* 42:288.

Stieltjes B, Brunner RM, Fritzsche KH, Laun FB (2013) Introduction to diffusion imaging In *Diffusion Tensor Imaging*, pp. 5–40. Springer, Heidelberg.

- Tournier JD, Calamante F, Connelly A et al. (2007) Robust determination of the fibre orientation distribution in diffusion MRI: non-negativity constrained super-resolved spherical deconvolution. *NeuroImage* 35:1459–1472.
- Tournier JD, Calamante F, Connelly A et al. (2012) MRtrix: Diffusion tractography in crossing fiber regions. *International Journal of Imaging Systems and Technology* 22:53–66.
- Tournier JD, Calamante F, Gadian DG, Connelly A et al. (2004) Direct estimation of the fiber orientation density function from diffusion-weighted MRI data using spherical deconvolution. *NeuroImage* 23:1176–1185.
- Tuch DS (2002) Diffusion MRI of complex tissue structure Ph.D. diss., University of Chicago and Massachusetts Institute of Technology.
- Tuch DS (2004) Q-ball imaging. *Magnetic Resonance in Medicine* 52:1358–1372.
- Tuch DS, Reese TG, Wiegell MR, Makris N, Belliveau JW, Wedeen VJ (2002) High angular resolution diffusion imaging reveals intravoxel white matter fiber heterogeneity. *Magnetic Resonance in Medicine* 48:577–582.
- Wedeen VJ, Hagmann P, Tseng WYI, Reese TG, Weisskoff RM (2005) Mapping complex tissue architecture with diffusion spectrum magnetic resonance imaging. *Magnetic Resonance in Medicine* 54:1377–1386.
- Wedeen V, Reese T, Tuch D, Weigel M, Dou J, Weiskoff R, Chessler D (2000) Mapping fiber orientation spectra in cerebral white matter with fourier transform diffusion MRI In *Proceedings of the 8th Annual Meeting of ISMRM, Denver*, p. 82.
- Wedeen V, Wang R, Schmahmann J, Benner T, Tseng W, Dai G, Pandya D, Hagmann P, D’Arceuil H, De Crespigny A (2008) Diffusion spectrum magnetic resonance imaging (DSI) tractography of crossing fibers. *Neuroimage* 41:1267–1277.
- Woolrich MW, Jbabdi S, Patenaude B, Chappell M, Makni S, Behrens T, Beckmann C, Jenkinson M, Smith SM et al. (2009) Bayesian analysis of neuroimaging data in FSL. *Neuroimage* 45:S173–S186.

Worsley KJ, Evans AC, Marrett S, Neelin P (1992) A three-dimensional statistical analysis for CBF activation studies in human brain. *Journal of Cerebral Blood Flow and Metabolism* 12:900–900.

Yo TS, Anwender A, Descoteaux M, Fillard P, Poupon C, Knösche T (2009) Quantifying brain connectivity: a comparative tractography study In *Medical Image Computing and Computer-Assisted Intervention–MICCAI 2009*, pp. 886–893. Springer.

Yushkevich PA, Zhang H, Simon TJ, Gee JC (2008) Structure-specific statistical mapping of white matter tracts. *Neuroimage* 41:448–461.

Zhang H, Schneider T, Wheeler-Kingshott CA, Alexander DC (2012) NODDI: Practical in vivo neurite orientation dispersion and density imaging of the human brain. *Neuroimage* 61:1000–1016.





# List of Figures

5.1	The human brain. . . . .	17
5.2	Picture of a neuron. . . . .	18
5.3	The human brain at different scales. . . . .	19
5.4	Hindered and restricted diffusion. . . . .	21
5.5	Gaussian shape of the diffusion propagator. . . . .	22
5.6	Scheme of the dephase-rephase sequence to measure the diffusion of water molecules. . . . .	23
5.7	The diffusion tensor visualized as ellipsoid. . . . .	26
5.8	Indices of the diffusion tensor . . . . .	28
5.9	Fiber configuration influencing FA. . . . .	28
5.10	Diffusion spectrum imaging . . . . .	32
5.11	Funk Radon transform . . . . .	34
5.12	Principle of spherical deconvolution. . . . .	35
5.13	Glyph representation of spherical harmonic base functions. . . . .	40
5.14	Signal attenuation profile approximation with spherical harmonics of different order. . . . .	41
5.15	Principle of deterministic tractography. . . . .	42
5.16	Visitation map from probabilistic tractography. . . . .	43
5.17	Principle of global tractography with self-organizing particles. . . . .	44
5.18	Principle of tract-based spatial statistics (TBSS). . . . .	47
5.19	Effect of fODF modulation shown on a “ring” phantom. . . . .	48
6.1	Average intensities of axial slices from dMRI volumes. . . . .	52

6.2	Consecutive axial slices with signal dropout due to motion. . . . .	53
6.3	Outline of the white matter mask obtained from segmentation of FA map. . . . .	55
6.4	Comparing indices of different fiber configurations. . . . .	58
6.5	Modeling the connecting pathway using Catmull-Rom splines. . . . .	59
6.6	Initialization based on probabilistic tractography. . . . .	61
6.7	Schematic drawing of a glyph with two peaks. . . . .	63
6.8	Parameters for minimum number of probabilistic streamlines and search radius. . . . .	66
6.9	Anatomy of basal ganglia. . . . .	68
6.10	Atlas and tracks of the left inferior longitudinal fasciculus of a single subject. . . . .	70
7.1	Glyphs showing different fiber configurations. . . . .	74
7.2	Glyphs of voxels computed with different deconvolution kernels. . . . .	75
7.3	FD FF and FS in parallel, fanning and crossing fiber configurations computed from CSD with different response kernels. . . . .	76
7.4	Phantom of the FiberCup. . . . .	77
7.5	Plausibility Tracking applied to phantom data of the FiberCup. . . . .	78
7.6	Plausibility Tracking applied to phantom data of the FiberCup. . . . .	79
7.7	Close up on the fODF glyphs in the lower crossing region. . . . .	80
7.8	Most plausible pathway for each spatial location. . . . .	81
7.9	Results of the winning method of the FiberCup and probabilistic tractography on the phantom. . . . .	82
7.10	Comparison of deterministic and probabilistic tractography with Plausibility Tracking. . . . .	84
7.11	Distribution of the plausibility of connections with points in BA45, MC and PFC. . . . .	85
7.12	Reconstruction of four major fiber bundles. . . . .	86
7.13	Effect of waypoint masks on the connection between substantia nigra and putamen. . . . .	88
7.14	Connection between substantia nigra and putamen. . . . .	89
7.15	Parametrization of a fiber bundle with multiple planes. . . . .	90

---

7.16	Indices along the inter-hemispheric connection between left and right BA45, overlaid to a coronal slice of an FA map. . . . .	91
7.17	Pathway of the left ILF modeled by Plausibility Tracking in one subject, overlaid to a sagittal slice of a FA map through the left occipital cortex. . . . .	92
7.18	Distribution of plausibility values plotted for the ILF of all subjects. .	93
7.19	Indices mapped onto the ILF pathway of a representative subject. . . .	93
7.20	Different indices sampled along the ILF. . . . .	95
7.21	Fiber bundles interacting with the ILF within the temporal lobe. . . .	96



# List of Tables

7.1 Computational performance of Plausibility Tracking. . . . . 86



# Erklärung

Ich versichere, dass ich die vorliegende Arbeit ohne unzulässige Hilfe Dritter und ohne Benutzung anderer als der angegebenen Hilfsmittel angefertigt habe. Die aus anderen Quellen direkt oder indirekt übernommenen Daten und Konzepte sind unter Angabe der Quelle gekennzeichnet.

Bei der Auswahl und Auswertung folgenden Materials haben mir die nachstehend aufgeführten Personen in der jeweils beschriebenen Weise ~~entgeltlich~~/unentgeltlich<sup>1</sup> geholfen:

1. Andreas Hintzen und Marc Tittgemeyer vom Max-Planck-Institut für neurologische Forschung stellten die Daten und Masken für die Anwendung “Connections through minor pathways” zur Verfügung. Die Idee für dieses Projekt stammt von ihnen.

Weitere Personen waren an der inhaltlich-materiellen Erstellung der vorliegenden Arbeit nicht beteiligt. Insbesondere habe ich hierfür nicht die entgeltliche Hilfe von Vermittlungs- bzw. Beratungsdiensten (Promotionsberater oder andere Personen) in Anspruch genommen. Niemand hat von mir unmittelbar oder mittelbar geldwerte Leistungen für Arbeiten erhalten, die im Zusammenhang mit dem Inhalt der vorgelegten Dissertation stehen.

Die Arbeit wurde bisher weder im In- noch im Ausland in gleicher oder ähnlicher Form einer Prüfungsbehörde vorgelegt.

---

<sup>1</sup>Unzutreffendes bitte streichen



Ich bin darauf hingewiesen worden, dass die Unrichtigkeit der vorstehenden Erklärung als Täuschungsversuch bewertet wird und gemäß § 7 Abs. 8 der Promotionsordnung den Abbruch des Promotionsverfahrens zur Folge hat.

(Ort, Datum)

(Unterschrift)

## MPI Series in Human Cognitive and Brain Sciences:

- 1 Anja Hahne  
*Charakteristika syntaktischer und semantischer Prozesse bei der auditiven Sprachverarbeitung: Evidenz aus ereigniskorrelierten Potentialstudien*
- 2 Ricarda Schubotz  
*Erinnern kurzer Zeitdauern: Behaviorale und neurophysiologische Korrelate einer Arbeitsgedächtnisfunktion*
- 3 Volker Bosch  
*Das Halten von Information im Arbeitsgedächtnis: Dissoziationen langsamer corticaler Potentiale*
- 4 Jorge Jovicich  
*An investigation of the use of Gradient- and Spin-Echo (GRASE) imaging for functional MRI of the human brain*
- 5 Rosemary C. Dymond  
*Spatial Specificity and Temporal Accuracy in Functional Magnetic Resonance Investigations*
- 6 Stefan Zysset  
*Eine experimentalphysiologische Studie zu Gedächtnisabrufprozessen unter Verwendung der funktionellen Magnetresonanztomographie*
- 7 Ulrich Hartmann  
*Ein mechanisches Finite-Elemente-Modell des menschlichen Kopfes*
- 8 Bertram Opitz  
*Funktionelle Neuroanatomie der Verarbeitung einfacher und komplexer akustischer Reize: Integration haemodynamischer und elektrophysiologischer Maße*
- 9 Gisela Müller-Plath  
*Formale Modellierung visueller Suchstrategien mit Anwendungen bei der Lokalisation von Hirnfunktionen und in der Diagnostik von Aufmerksamkeitsstörungen*
- 10 Thomas Jacobsen  
*Characteristics of processing morphological structural and inherent case in language comprehension*
- 11 Stefan Kölsch  
*Brain and Music  
A contribution to the investigation of central auditory processing with a new electrophysiological approach*
- 12 Stefan Frisch  
*Verb-Argument-Struktur, Kasus und thematische Interpretation beim Sprachverstehen*
- 13 Markus Ullsperger  
*The role of retrieval inhibition in directed forgetting – an event-related brain potential analysis*
- 14 Martin Koch  
*Measurement of the Self-Diffusion Tensor of Water in the Human Brain*
- 15 Axel Hutt  
*Methoden zur Untersuchung der Dynamik raumzeitlicher Signale*
- 16 Frithjof Kruggel  
*Detektion und Quantifizierung von Hirnaktivität mit der funktionellen Magnetresonanztomographie*
- 17 Anja Dove  
*Lokalisierung an internen Kontrollprozessen beteiligter Hirngebiete mithilfe des Aufgabenwechselparadigmas und der ereigniskorrelierten funktionellen Magnetresonanztomographie*
- 18 Karsten Steinhauer  
*Hirnphysiologische Korrelate prosodischer Satzverarbeitung bei gesprochener und geschriebener Sprache*
- 19 Silke Urban  
*Verbinformationen im Satzverstehen*
- 20 Katja Werheid  
*Implizites Sequenzlernen bei Morbus Parkinson*
- 21 Doreen Nessler  
*Is it Memory or Illusion? Electrophysiological Characteristics of True and False Recognition*
- 22 Christoph Herrmann  
*Die Bedeutung von 40-Hz-Oszillationen für kognitive Prozesse*
- 23 Christian Fiebach  
*Working Memory and Syntax during Sentence Processing.  
A neurocognitive investigation with event-related brain potentials and functional magnetic resonance imaging*
- 24 Grit Hein  
*Lokalisation von Doppelaufgabendefiziten bei gesunden älteren Personen und neurologischen Patienten*
- 25 Monica de Filippis  
*Die visuelle Verarbeitung unbeachteter Wörter: Ein elektrophysiologischer Ansatz*
- 26 Ulrich Müller  
*Die catecholaminerge Modulation präfrontaler kognitiver Funktionen beim Menschen*
- 27 Kristina Uhl  
*Kontrollfunktion des Arbeitsgedächtnisses über interferierende Information*
- 28 Ina Bornkessel  
*The Argument Dependency Model: A Neurocognitive Approach to Incremental Interpretation*
- 29 Sonja Lattner  
*Neurophysiologische Untersuchungen zur auditorischen Verarbeitung von Stimminformationen*
- 30 Christin Grünewald  
*Die Rolle motorischer Schemata bei der Objektrepräsentation: Untersuchungen mit funktioneller Magnetresonanztomographie*
- 31 Annett Schirmer  
*Emotional Speech Perception: Electrophysiological Insights into the Processing of Emotional Prosody and Word Valence in Men and Women*
- 32 André J. Szameitat  
*Die Funktionalität des lateral-präfrontalen Cortex für die Verarbeitung von Doppelaufgaben*
- 33 Susanne Wagner  
*Verbales Arbeitsgedächtnis und die Verarbeitung ambiger Wörter in Wort- und Satzkontexten*
- 34 Sophie Manthey  
*Hirn und Handlung: Untersuchung der Handlungsrepräsentation im ventralen prämotorischen Cortex mit Hilfe der funktionellen Magnetresonanztomographie*
- 35 Stefan Heim  
*Towards a Common Neural Network Model of Language Production and Comprehension: fMRI Evidence for the Processing of Phonological and Syntactic Information in Single Words*
- 36 Claudia Friedrich  
*Prosody and spoken word recognition: Behavioral and ERP correlates*
- 37 Ulrike Lex  
*Sprachlateralisierung bei Rechts- und Linkshändern mit funktioneller Magnetresonanztomographie*

- 38 Thomas Arnold  
*Computergestützte Befundung klinischer Elektroenzephalogramme*
- 39 Carsten H. Wolters  
*Influence of Tissue Conductivity Inhomogeneity and Anisotropy on EEG/MEG based Source Localization in the Human Brain*
- 40 Ansgar Hantsch  
*Fisch oder Karpfen? Lexikale Aktivierung von Benennungsalternativen bei der Objektbenennung*
- 41 Peggy Bungert  
*Zentralnervöse Verarbeitung akustischer Informationen  
Signalidentifikation, Signallateralisation und zeitgebundene Informationsverarbeitung bei Patienten mit erworbenen Hirnschädigungen*
- 42 Daniel Senkowski  
*Neuronal correlates of selective attention: An investigation of electrophysiological brain responses in the EEG and MEG*
- 43 Gert Wollny  
*Analysis of Changes in Temporal Series of Medical Images*
- 44 Angelika Wolf  
*Sprachverstehen mit Cochlea-Implantat: EKP-Studien mit postlingual ertaubten erwachsenen CI-Trägern*
- 45 Kirsten G. Volz  
*Brain correlates of uncertain decisions: Types and degrees of uncertainty*
- 46 Hagen Huttner  
*Magnetresonanztomographische Untersuchungen über die anatomische Variabilität des Frontallappens des menschlichen Großhirns*
- 47 Dirk Köster  
*Morphology and Spoken Word Comprehension: Electrophysiological Investigations of Internal Compound Structure*
- 48 Claudia A. Hruska  
*Einflüsse kontextueller und prosodischer Informationen in der auditorischen Satzverarbeitung: Untersuchungen mit ereigniskorrelierten Hirmpotentialen*
- 49 Hannes Ruge  
*Eine Analyse des raum-zeitlichen Musters neuronaler Aktivierung im Aufgabenwechselparadigma zur Untersuchung handlungssteuernder Prozesse*
- 50 Ricarda I. Schubotz  
*Human premotor cortex: Beyond motor performance*
- 51 Clemens von Zerssen  
*Bewusstes Erinnern und falsches Wiedererkennen: Eine funktionelle MRT Studie neuroanatomischer Gedächtniskorrelate*
- 52 Christiane Weber  
*Rhythm is gonna get you.  
Electrophysiological markers of rhythmic processing in infants with and without risk for Specific Language Impairment (SLI)*
- 53 Marc Schönwiesner  
*Functional Mapping of Basic Acoustic Parameters in the Human Central Auditory System*
- 54 Katja Fiehler  
*Temporospatial characteristics of error correction*
- 55 Britta Stolterfoht  
*Processing Word Order Variations and Ellipses: The Interplay of Syntax and Information Structure during Sentence Comprehension*
- 56 Claudia Danielmeier  
*Neuronale Grundlagen der Interferenz zwischen Handlung und visueller Wahrnehmung*
- 57 Margret Hund-Georgiadis  
*Die Organisation von Sprache und ihre Reorganisation bei ausgewählten, neurologischen Erkrankungen gemessen mit funktioneller Magnetresonanztomographie – Einflüsse von Händigkeit, Läsion, Performanz und Perfusion*
- 58 Jutta L. Mueller  
*Mechanisms of auditory sentence comprehension in first and second language: An electrophysiological miniature grammar study*
- 59 Franziska Biedermann  
*Auditorische Diskriminationsleistungen nach unilateralen Läsionen im Di- und Telenzephalon*
- 60 Shirley-Ann Rüschmeyer  
*The Processing of Lexical Semantic and Syntactic Information in Spoken Sentences: Neuroimaging and Behavioral Studies of Native and Non-Native Speakers*
- 61 Kerstin Leuckefeld  
*The Development of Argument Processing Mechanisms in German. An Electrophysiological Investigation with School-Aged Children and Adults*
- 62 Axel Christian Kühn  
*Bestimmung der Lateralisierung von Sprachprozessen unter besondere Berücksichtigung des temporalen Cortex, gemessen mit fMRT*
- 63 Ann Pannekamp  
*Prosodische Informationsverarbeitung bei normalsprachlichem und deviantem Satzmaterial: Untersuchungen mit ereigniskorrelierten Hirmpotentialen*
- 64 Jan Derrfuß  
*Functional specialization in the lateral frontal cortex: The role of the inferior frontal junction in cognitive control*
- 65 Andrea Mona Philipp  
*The cognitive representation of tasks – Exploring the role of response modalities using the task-switching paradigm*
- 66 Ulrike Toepe  
*Contrastive Topic and Focus Information in Discourse – Prosodic Realisation and Electrophysiological Brain Correlates*
- 67 Karsten Müller  
*Die Anwendung von Spektral- und Waveletanalyse zur Untersuchung der Dynamik von BOLD-Zeitreihen verschiedener Hirnareale*
- 68 Sonja A. Kotz  
*The role of the basal ganglia in auditory language processing: Evidence from ERP lesion studies and functional neuroimaging*
- 69 Sonja Rossi  
*The role of proficiency in syntactic second language processing: Evidence from event-related brain potentials in German and Italian*
- 70 Birte U. Forstmann  
*Behavioral and neural correlates of endogenous control processes in task switching*
- 71 Silke Paulmann  
*Electrophysiological Evidence on the Processing of Emotional Prosody: Insights from Healthy and Patient Populations*
- 72 Matthias L. Schroeter  
*Enlightening the Brain – Optical Imaging in Cognitive Neuroscience*
- 73 Julia Reinholz  
*Interhemispheric interaction in object- and word-related visual areas*
- 74 Evelyn C. Ferstl  
*The Functional Neuroanatomy of Text Comprehension*
- 75 Miriam Gade  
*Aufgabeneinhibition als Mechanismus der Konfliktreduktion zwischen Aufgabenrepräsentationen*

- 76 Juliane Hofmann  
*Phonological, Morphological, and Semantic Aspects of Grammatical Gender Processing in German*
- 77 Petra Augurzky  
*Attaching Relative Clauses in German – The Role of Implicit and Explicit Prosody in Sentence Processing*
- 78 Uta Wolfensteller  
*Habituelle und arbiträre sensorimotorische Verknüpfungen im lateralen prämotorischen Kortex des Menschen*
- 79 Päivi Sivonen  
*Event-related brain activation in speech perception: From sensory to cognitive processes*
- 80 Yun Nan  
*Music phrase structure perception: the neural basis, the effects of acculturation and musical training*
- 81 Katrin Schulze  
*Neural Correlates of Working Memory for Verbal and Tonal Stimuli in Nonmusicians and Musicians With and Without Absolute Pitch*
- 82 Korinna Eckstein  
*Interaktion von Syntax und Prosodie beim Sprachverstehen: Untersuchungen anhand ereigniskorrelierter Hirmpotentiale*
- 83 Florian Th. Siebörger  
*Funktionelle Neuroanatomie des Textverstehens: Kohärenzbildung bei Witzen und anderen ungewöhnlichen Texten*
- 84 Diana Böttger  
*Aktivität im Gamma-Frequenzbereich des EEG: Einfluss demographischer Faktoren und kognitiver Korrelate*
- 85 Jörg Bahlmann  
*Neural correlates of the processing of linear and hierarchical artificial grammar rules: Electrophysiological and neuroimaging studies*
- 86 Jan Zwickel  
*Specific Interference Effects Between Temporally Overlapping Action and Perception*
- 87 Markus Ullsperger  
*Functional Neuroanatomy of Performance Monitoring: fMRI, ERP, and Patient Studies*
- 88 Susanne Dietrich  
*Vom Brüllen zum Wort – MRT-Studien zur kognitiven Verarbeitung emotionaler Vokalisationen*
- 89 Maren Schmidt-Kassow  
*What's Beat got to do with ist? The Influence of Meter on Syntactic Processing: ERP Evidence from Healthy and Patient populations*
- 90 Monika Lück  
*Die Verarbeitung morphologisch komplexer Wörter bei Kindern im Schulalter: Neuropsychologische Korrelate der Entwicklung*
- 91 Diana P. Szameitat  
*Perzeption und akustische Eigenschaften von Emotionen in menschlichem Lachen*
- 92 Beate Sabisch  
*Mechanisms of auditory sentence comprehension in children with specific language impairment and children with developmental dyslexia: A neurophysiological investigation*
- 93 Regine Oberecker  
*Grammatikverarbeitung im Kindesalter: EKP-Studien zum auditorischen Satzverstehen*
- 94 Şükrü Banş Demiral  
*Incremental Argument Interpretation in Turkish Sentence Comprehension*
- 95 Henning Holle  
*The Comprehension of Co-Speech Iconic Gestures: Behavioral, Electrophysiological and Neuroimaging Studies*
- 96 Marcel Braß  
*Das inferior frontale Kreuzungsareal und seine Rolle bei der kognitiven Kontrolle unseres Verhaltens*
- 97 Anna S. Hasting  
*Syntax in a blink: Early and automatic processing of syntactic rules as revealed by event-related brain potentials*
- 98 Sebastian Jentschke  
*Neural Correlates of Processing Syntax in Music and Language – Influences of Development, Musical Training and Language Impairment*
- 99 Amelie Mahlstedt  
*The Acquisition of Case marking Information as a Cue to Argument Interpretation in German  
An Electrophysiological Investigation with Pre-school Children*
- 100 Nikolaus Steinbeis  
*Investigating the meaning of music using EEG and fMRI*
- 101 Tilmann A. Klein  
*Learning from errors: Genetic evidence for a central role of dopamine in human performance monitoring*
- 102 Franziska Maria Korb  
*Die funktionelle Spezialisierung des lateralen präfrontalen Cortex: Untersuchungen mittels funktioneller Magnetresonanztomographie*
- 103 Sonja Fleischhauer  
*Neuronale Verarbeitung emotionaler Prosodie und Syntax: die Rolle des verbalen Arbeitsgedächtnisses*
- 104 Friederike Sophie Haupt  
*The component mapping problem: An investigation of grammatical function reanalysis in differing experimental contexts using eventrelated brain potentials*
- 105 Jens Brauer  
*Functional development and structural maturation in the brain's neural network underlying language comprehension*
- 106 Philipp Kanske  
*Exploring executive attention in emotion: ERP and fMRI evidence*
- 107 Julia Grieser Painter  
*Music, meaning, and a semantic space for musical sounds*
- 108 Daniela Sammler  
*The Neuroanatomical Overlap of Syntax Processing in Music and Language - Evidence from Lesion and Intracranial ERP Studies*
- 109 Norbert Zmyj  
*Selective Imitation in One-Year-Olds: How a Model's Characteristics Influence Imitation*
- 110 Thomas Fritz  
*Emotion investigated with music of variable valence – neurophysiology and cultural influence*
- 111 Stefanie Regel  
*The comprehension of figurative language: Electrophysiological evidence on the processing of irony*
- 112 Miriam Beisert  
*Transformation Rules in Tool Use*
- 113 Veronika Krieghoff  
*Neural correlates of Intentional Actions*
- 114 Andreja Bubić  
*Violation of expectations in sequence processing*

- 115 Claudia Männel  
*Prosodic processing during language acquisition: Electrophysiological studies on intonational phrase processing*
- 116 Konstanze Albrecht  
*Brain correlates of cognitive processes underlying intertemporal choice for self and other*
- 117 Katrin Sakreida  
*Nicht-motorische Funktionen des prämotorischen Kortex: Patientenstudien und funktionelle Bildgebung*
- 118 Susann Wolff  
*The interplay of free word order and pro-drop in incremental sentence processing: Neurophysiological evidence from Japanese*
- 119 Tim Raettig  
*The Cortical Infrastructure of Language Processing: Evidence from Functional and Anatomical Neuroimaging*
- 120 Maria Golde  
*Premotor cortex contributions to abstract and action-related relational processing*
- 121 Daniel S. Margulies  
*Resting-State Functional Connectivity fMRI: A new approach for assessing functional neuroanatomy in humans with applications to neuroanatomical, developmental and clinical questions*
- 122 Franziska Stüb  
*The interplay between attention and syntactic processes in the adult and developing brain: ERP evidences*
- 123 Stefan Bode  
*From stimuli to motor responses: Decoding rules and decision mechanisms in the human brain*
- 124 Christiane Diefenbach  
*Interactions between sentence comprehension and concurrent action: The role of movement effects and timing*
- 125 Moritz M. Daum  
*Mechanismen der frühkindlichen Entwicklung des Handlungsverständnisses*
- 126 Jürgen Dukart  
*Contribution of FDG-PET and MRI to improve Understanding, Detection and Differentiation of Dementia*
- 127 Kamal Kumar Choudhary  
*Incremental Argument Interpretation in a Split Ergative Language: Neurophysiological Evidence from Hindi*
- 128 Peggy Sparenberg  
*Filling the Gap: Temporal and Motor Aspects of the Mental Simulation of Occluded Actions*
- 129 Luming Wang  
*The Influence of Animacy and Context on Word Order Processing: Neurophysiological Evidence from Mandarin Chinese*
- 130 Barbara Ettrich  
*Beeinträchtigung frontomedianer Funktionen bei Schädel-Hirn-Trauma*
- 131 Sandra Dietrich  
*Coordination of Unimanual Continuous Movements with External Events*
- 132 R. Muralikrishnan  
*An Electrophysiological Investigation Of Tamil Dative-Subject Constructions*
- 133 Christian Obermeier  
*Exploring the significance of task, timing and background noise on gesture-speech integration*
- 134 Björn Herrmann  
*Grammar and perception: Dissociation of early auditory processes in the brain*
- 135 Eugenia Solano-Castiella  
*In vivo anatomical segmentation of the human amygdala and parcellation of emotional processing*
- 136 Marco Taubert  
*Plastizität im sensorimotorischen System – Lerninduzierte Veränderungen in der Struktur und Funktion des menschlichen Gehirns*
- 137 Patricia Garrido Vázquez  
*Emotion Processing in Parkinson's Disease: The Role of Motor Symptom Asymmetry*
- 138 Michael Schwartz  
*Adaptation to temporal structure*
- 139 Christine S. Schipke  
*Processing Mechanisms of Argument Structure and Case-marking in Child Development: Neural Correlates and Behavioral Evidence*
- 140 Sarah Jessen  
*Emotion Perception in the Multisensory Brain*
- 141 Jane Neumann  
*Beyond activation detection: Advancing computational techniques for the analysis of functional MRI data*
- 142 Franziska Knolle  
*Knowing what's next: The role of the cerebellum in generating predictions*
- 143 Michael Skeide  
*Syntax and semantics networks in the developing brain*
- 144 Sarah M. E. Gierhan  
*Brain networks for language: Anatomy and functional roles of neural pathways supporting language comprehension and repetition*
- 145 Lars Meyer  
*The Working Memory of Argument-Verb Dependencies: Spatiotemporal Brain Dynamics during Sentence Processing*
- 146 Benjamin Stahl  
*Treatment of Non-Fluent Aphasia through Melody, Rhythm and Formulaic Language*
- 147 Kathrin Rothermich  
*The rhythm's gonna get you: ERP and fMRI evidence on the interaction of metric and semantic processing*
- 148 Julia Merrill  
*Song and Speech Perception – Evidence from fMRI, Lesion Studies and Musical Disorder*
- 149 Klaus-Martin Krönke  
*Learning by Doing? Gesture-Based Word-Learning and its Neural Correlates in Healthy Volunteers and Patients with Residual Aphasia*
- 150 Lisa Joana Knoll  
*When the hedgehog kisses the frog: A functional and structural investigation of syntactic processing in the developing brain*
- 151 Nadine Diersch  
*Action prediction in the aging mind*
- 152 Thomas Dolk  
*A Referential Coding Account for the Social Simon Effect*
- 153 Mareike Bacha-Trams  
*Neurotransmitter receptor distribution in Broca's area and the posterior superior temporal gyrus*
- 154 Andrea Michaela Walter  
*The role of goal representations in action control*

- 155 Anne Keitel  
*Action perception in development: The role of experience*
- 156 Iris Nikola Knierim  
*Rules don't come easy: Investigating feedback-based learning of  
phonotactic rules in language.*